Commercializable Power Source Using Heterogeneous Hydrino Catalysts

R. L. Mills, K. Akhtar, G. Zhao, Z. Chang, J. He, X. Hu, G. Chu
BlackLight Power, Inc., 493 Old Trenton Road, Cranbury, NJ 08512

ABSTRACT

Using Maxwell's equations, the structure of the electron was derived by Mills as a boundary-value problem wherein the electron comprises the source current of time-varying electromagnetic fields during transitions with the constraint that the bound $n=1$ state electron cannot radiate energy. A reaction predicted by the solution involves a resonant, nonradiative energy transfer from otherwise stable atomic hydrogen to a catalyst capable of accepting the energy. Specifically, a catalyst comprises a chemical or physical process with an enthalpy change equal to an integer multiple m of the potential energy of atomic hydrogen, $27.2\ eV$. The product is $H(1/p)$, fractional Rydberg states of atomic hydrogen called "hydrino atoms" wherein $n = \dfrac{1}{2}, \dfrac{1}{3}, \dfrac{1}{4}, ..., \dfrac{1}{p}$ ($p \le 137$ is an integer) replaces the well-known parameter $n = \text{integer}$ in the Rydberg equation for hydrogen excited states. The reaction step of a nonradiative energy transfer of an integer multiple of $27.2\ eV$ from atomic hydrogen to the catalyst results in an ionized catalyst and free electrons that may cause the reaction to rapidly cease due to charge accumulation. Li, K, and NaH served as the catalysts to form hydrinos at a rapid rate when a high-surface-area conductive support doped with an oxidant was added to speed up the rate limiting step, the removal of electrons from the catalyst as it is ionized by accepting the nonradiative resonant energy transfer from atomic hydrogen to form hydrinos. The concerted electron-acceptor reaction from the catalyst to oxidant via the support was also exothermic to heat the reactants and enhance the rates. Using water-flow, batch calorimetry, the measured power and energy gain from these heterogeneous catalyst systems were up to over $10\ W/cm^3$ (reactant volume) and a factor of over six times the maximum theoretical, respectively. The reaction scaled linearly to 580 kJ that developed a power of about 30 kW. Solution ^1H NMR on samples extracted from the reaction products in DMF-d7 showed the predicted H_2 (1/4) and H^- (1/4) at 1.2 ppm and −3.8 ppm, respectively. ToF-SIMs showed sodium hydrino hydride peaks such as NaH_x, peaks with NaH catalyst, and the predicted 11 eV binding energy of H^- (1/4) was observed by XPS. In an advancement over prior $NaOH$-doped Raney Ni power systems, the reactants of each solid fuel or heterogeneous-catalyst system can be regenerated from the products using commercial chemical-plant systems. Based on the observed energy gain and successful thermal regeneration, green power plants can be operated continuously as power and eutectic-melt electrolysis or thermal regeneration reactions are maintained in synchrony. The system is closed except that only hydrogen consumed in forming hydrinos need be replaced.

Hydrogen can be obtained ultimately from the water with 200 times the energy release relative to combustion. These results indicate current commercial feasibility.

I. Introduction

A. Catalytic Lower-Energy Hydrogen Electronic Transitions

Classical physics (CP) gives closed-form solutions of the hydrogen atom, the hydride ion, the hydrogen molecular ion, and the hydrogen molecule and predicts corresponding species having fractional principal quantum numbers [1-12]. The nonradiative state of atomic hydrogen, which is historically called the "ground state," forms the basis of the boundary condition of CP to solve the bound electron. CP predicts a reaction involving a resonant, nonradiative energy transfer from otherwise stable atomic hydrogen to a catalyst capable of accepting the energy to form hydrogen in lower-energy states than previously thought possible. Specifically, CP predicts that atomic hydrogen may undergo a catalytic reaction with certain atoms, excimers, ions, and diatomic hydrides which provide a reaction with a net enthalpy of an integer multiple of the potential energy of atomic hydrogen, $E_h = 27.2 \ eV$ where E_h is one Hartree. Specific species (e.g. He^+, Ar^+, Sr^+, K, Li, HCl, and NaH) identifiable on the basis of their known electron energy levels are required to be present with atomic hydrogen to catalyze the process. The reaction involves a nonradiative energy transfer of an integer multiple of $27.2 \ eV$ from atomic hydrogen to the catalyst followed by $q \cdot 13.6 \ eV$ continuum emission or $q \cdot 13.6 \ eV$ transfer to another H to form extraordinarily hot, excited-state H and a hydrogen atom that is lower in energy than unreacted atomic hydrogen that corresponds to a fractional principal quantum number. That is, in the formula for the principal energy levels of the hydrogen atom:

$$E_n = -\frac{e^2}{n^2 8\pi\varepsilon_o a_H} = -\frac{13.598 \ eV}{n^2} \tag{1}$$

$$n = 1, 2, 3, ... \tag{2}$$

where a_H is the Bohr radius for the hydrogen atom (52.947 pm), e is the magnitude of the charge of the electron, and ε_o is the vacuum permittivity, fractional quantum numbers:

$$n = 1, \frac{1}{2}, \frac{1}{3}, \frac{1}{4}, ..., \frac{1}{p}; \quad p \leq 137 \text{ is an integer} \tag{3}$$

replace the well known parameter $n =$ integer in the Rydberg equation for hydrogen excited states. The $n = 1$ state of hydrogen and the $n = \frac{1}{\text{integer}}$ states of hydrogen are nonradiative, but a transition between two nonradiative states, say $n = 1$ to $n = 1/2$, is possible via a nonradiative energy transfer. Hydrogen is a special case of the stable states given by Eqs. (1) and (3) wherein the corresponding radius of the hydrogen or hydrino atom is given by

$$r = \frac{a_H}{p}, \tag{4}$$

where $p = 1, 2, 3, ...$. In order to conserve energy, energy must be transferred from the hydrogen atom to the catalyst in units of

$$m \cdot 27.2 \ eV, \ m = 1, 2, 3, 4, ... \tag{5}$$

and the radius transitions to $\frac{a_H}{m+p}$. The catalyst reactions involve two steps of energy release [1, 13]: a nonradiative energy transfer to the catalyst followed by additional energy release as the radius decreases to the corresponding stable final state. Thus, the general reaction is given by

$$m \cdot 27.2 \ eV + Cat^{q+} + H\left[\frac{a_H}{p}\right] \rightarrow Cat^{(q+r)+} + re^- + H*\left[\frac{a_H}{(m+p)}\right] + m \cdot 27.2 \ eV \quad (6)$$

$$H*\left[\frac{a_H}{(m+p)}\right] \rightarrow H\left[\frac{a_H}{(m+p)}\right] + [(p+m)^2 - p^2] \cdot 13.6 \ eV - m \cdot 27.2 \ eV \quad (7)$$

$$Cat^{(q+r)+} + re^- \rightarrow Cat^{q+} + m \cdot 27.2 \ eV \quad (8)$$

And, the overall reaction is

$$H\left[\frac{a_H}{p}\right] \rightarrow H\left[\frac{a_H}{(m+p)}\right] + [(p+m)^2 - p^2] \cdot 13.6 \ eV \quad (9)$$

q, r, m, and p are integers. $H*\left[\dfrac{a_H}{(m+p)}\right]$ has the radius of the hydrogen atom (corresponding to the 1 in the denominator) and a central field equivalent to $(m+p)$ times that of a proton, and $H\left[\dfrac{a_H}{(m+p)}\right]$ is the corresponding stable state with the radius of $\dfrac{1}{(m+p)}$ that of H. As the electron undergoes radial acceleration from the radius of the hydrogen atom to a radius of $\dfrac{1}{(m+p)}$ this distance, energy is released as characteristic light emission or as third-body kinetic energy. The emission may be in the form of an extreme-ultraviolet continuum radiation having an edge at $[(p+m)^2 - p^2 - 2m] \cdot 13.6 \ eV$ or $\dfrac{91.2}{[(p+m)^2 - p^2 - 2m]} \ nm$ and extending to longer wavelengths. In addition to radiation, a resonant kinetic energy transfer to form fast H may occur. Subsequent excitation of these fast $H(n=1)$ atoms by collisions with the background H_2 followed by emission of the corresponding $H(n=3)$ fast atoms gives rise to broadened Balmer α emission. Extraordinary (>100 eV) Balmer α line broadening is observed consistent with predictions [14-26].

Thus, a catalyst provides a net positive enthalpy of reaction of $m \cdot 27.2 \ eV$ (i.e. it resonantly accepts the nonradiative energy transfer from hydrogen atoms and releases the energy to the surroundings to affect electronic transitions to fractional quantum energy levels). As a consequence of the nonradiative energy transfer, the hydrogen atom becomes unstable and emits further energy until it achieves a lower-energy nonradiative state having a principal energy level given by Eqs. (1) and (3). Thus, the catalysis releases energy from the hydrogen atom with a commensurate decrease in size of the hydrogen atom, $r_n = na_H$ where n is given by Eq. (3). For example, the catalysis of $H(n=1)$ to $H(n=1/4)$ releases $204 \ eV$, and the hydrogen radius decreases from a_H to $\dfrac{1}{4}a_H$. The catalyst product, $H(1/p)$, may also react with an electron to form a hydrino hydride ion $H^-(1/p)$, or two $H(1/p)$ may react to form the corresponding molecular hydrino $H_2(1/p)$.

Specifically, the catalyst product, $H(1/p)$, may also react with an electron to form a novel hydride ion $H^-(1/p)$ with a binding energy E_B [1, 14-17, 27-31]:

$$E_B = \frac{\hbar^2 \sqrt{s(s+1)}}{8\mu_e a_0^2 \left[\frac{1+\sqrt{s(s+1)}}{p}\right]^2} - \frac{\pi\mu_0 e^2 \hbar^2}{m_e^2}\left(\frac{1}{a_H^3} + \frac{2^2}{a_0^3 \left[\frac{1+\sqrt{s(s+1)}}{p}\right]^3}\right) \tag{10}$$

where $p = \text{integer} > 1$, $s = 1/2$, $\hbar$ is Planck's constant bar, μ_o is the permeability of vacuum, m_e is the mass of the electron, μ_e is the reduced electron mass given by $\mu_e = \dfrac{m_e m_p}{\dfrac{m_e}{\sqrt{\dfrac{3}{4}}} + m_p}$ where m_p is the mass of the proton, a_o is the Bohr radius, and the ionic radius is $r_1 = \dfrac{a_0}{p}\left(1+\sqrt{s(s+1)}\right)$.

From Eq. (10), the calculated ionization energy of the hydride ion is $0.75418\ eV$, and the experimental value given by Lykke [32] is $6082.99 \pm 0.15\ cm^{-1}$ (0.75418 eV).

Upfield-shifted NMR peaks are direct evidence of the existence of lower-energy state hydrogen with a reduced radius relative to ordinary hydride ion and having an increase in diamagnetic shielding of the proton. The shift is given by the sum of that of an ordinary hydride ion H^- and a component due to the lower-energy state [1, 17]:

$$\frac{\Delta B_T}{B} = -\mu_0 \frac{e^2}{12 m_e a_0 \left(1+\sqrt{s(s+1)}\right)}\left(1+\alpha 2\pi p\right) = -\left(29.9 + 1.37 p\right) ppm \tag{11}$$

where for H^- $p = 0$ and $p = \text{integer} > 1$ for $H^-(1/p)$ and α is the fine structure constant.

$H(1/p)$ may react with a proton and two $H(1/p)$ may react to form $H_2(1/p)^+$ and $H_2(1/p)$, respectively. The hydrogen molecular ion and molecular charge and current density functions, bond distances, and energies were solved previously [1, 6] from the Laplacian in ellipsoidal coordinates with the constraint of nonradiation.

$$(\eta - \zeta)R_\xi \frac{\partial}{\partial \xi}\left(R_\xi \frac{\partial \phi}{\partial \xi}\right) + (\zeta - \xi)R_\eta \frac{\partial}{\partial \eta}\left(R_\eta \frac{\partial \phi}{\partial \eta}\right) + (\xi - \eta)R_\zeta \frac{\partial}{\partial \zeta}\left(R_\zeta \frac{\partial \phi}{\partial \zeta}\right) = 0 \tag{12}$$

The total energy E_T of the hydrogen molecular ion having a central field of $+pe$ at each focus of the prolate spheroid molecular orbital is

5

$$E_T = -p^2 \left\{ \frac{\dfrac{e^2}{8\pi\varepsilon_o a_H}(4\ln 3 - 1 - 2\ln 3)\left[1 + p\sqrt{\dfrac{2\hbar\sqrt{\dfrac{2e^2}{4\pi\varepsilon_o(2a_H)^3}}}{m_e c^2}} \right]}{-\dfrac{1}{2}\hbar\sqrt{\dfrac{\dfrac{pe^2}{4\pi\varepsilon_o\left(\dfrac{2a_H}{p}\right)^3} - \dfrac{pe^2}{8\pi\varepsilon_o\left(\dfrac{3a_H}{p}\right)^3}}{\mu}}} \right\} \tag{13}$$

$$= -p^2 16.13392\ eV - p^3 0.118755\ eV$$

where p is an integer, c is the speed of light in vacuum, and μ is the reduced nuclear mass [1, 6]. The total energy of the hydrogen molecule having a central field of $+pe$ at each focus of the prolate spheroid molecular orbital is

$$E_T = -p^2 \left\{ \frac{\dfrac{e^2}{8\pi\varepsilon_o a_0}\left[\left(2\sqrt{2} - \sqrt{2} + \dfrac{\sqrt{2}}{2}\right)\ln\dfrac{\sqrt{2}+1}{\sqrt{2}-1} - \sqrt{2} \right]\left[1 + p\sqrt{\dfrac{2\hbar\sqrt{\dfrac{e^2}{4\pi\varepsilon_o a_0^3}}}{m_e c^2}} \right]}{-\dfrac{1}{2}\hbar\sqrt{\dfrac{\dfrac{pe^2}{8\pi\varepsilon_o\left(\dfrac{a_0}{p}\right)^3} - \dfrac{pe^2}{8\pi\varepsilon_o\left(\dfrac{\left(1+\dfrac{1}{\sqrt{2}}\right)a_0}{p}\right)^3}}{\mu}}} \right\}$$

$$= -p^2 31.351\ eV - p^3 0.326469\ eV$$

(14)

The bond dissociation energy, E_D, of the hydrogen molecule $H_2(1/p)$ is the difference between the total energy of the corresponding hydrogen atoms and E_T

$$E_D = E(2H(1/p)) - E_T \tag{15}$$

where [33]

$$E(2H(1/p)) = -p^2 27.20\ eV \tag{16}$$

E_D is given by Eqs. (15-16) and (14):

$$E_D = -p^2 27.20\ eV - E_T$$

$$= -p^2 27.20\ eV - (-p^2 31.351\ eV - p^3 0.326469\ eV) \tag{17}$$

$$= p^2 4.151\ eV + p^3 0.326469\ eV$$

The calculated and experimental parameters of H_2, D_2, H_2^+, and D_2^+ from Ref. [1, 6] are given in Table 1.

The NMR of catalysis-product gas provides a definitive test of the theoretically predicted

chemical shift of H_2 (1/4). In general, the ^1H NMR resonance of H_2 (1/p) is predicted to be upfield from that of H_2 due to the fractional radius in elliptic coordinates [1, 6] wherein the electrons are significantly closer to the nuclei. The predicted shift, $\dfrac{\Delta B_T}{B}$, for H_2 (1/p) derived previously [1, 6] is given by the sum of that of H_2 and a term that depends on $p = $ integer > 1 for H_2 (1/p):

$$\frac{\Delta B_T}{B} = -\mu_0 \left(4 - \sqrt{2}\ln\frac{\sqrt{2}+1}{\sqrt{2}-1}\right)\frac{e^2}{36 a_0 m_e}(1 + \pi\alpha p) \tag{18}$$

$$\frac{\Delta B_T}{B} = -(28.01 + 0.64 p)\,ppm \tag{19}$$

where for H_2 $p = 0$. The experimental absolute H_2 gas-phase resonance shift of -28.0 ppm [34-37] is in excellent agreement with the predicted absolute gas-phase shift of -28.01 ppm (Eq. (19)).

The vibrational energies, E_{vib}, for the $\upsilon = 0$ to $\upsilon = 1$ transition of hydrogen-type molecules H_2 (1/p) are [1, 6]

$$E_{vib} = p^2 0.515902\ eV \tag{20}$$

where p is an integer and the experimental vibrational energy for the $\upsilon = 0$ to $\upsilon = 1$ transition of H_2, $E_{H_2(\upsilon=0\rightarrow\upsilon=1)}$, is given by Beutler [38] and Herzberg [39].

The rotational energies, E_{rot}, for the J to $J+1$ transition of hydrogen-type molecules H_2 (1/p) are [1, 6]

$$E_{rot} = E_{J+1} - E_J = \frac{\hbar^2}{I}(J+1) = p^2(J+1)0.01509\ eV \tag{21}$$

where p is an integer, I is the moment of inertia, and the experimental rotational energy for the $J = 0$ to $J = 1$ transition of H_2 is given by Atkins [40].

The p^2 dependence of the rotational energies results from an inverse p dependence of the internuclear distance and the corresponding impact on the moment of inertia I. The predicted internuclear distance $2c'$ for H_2 (1/p) is

$$2c' = \frac{a_0\sqrt{2}}{p} \tag{22}$$

B. Prior Results

The data from a broad spectrum of investigational techniques strongly and consistently indicates that hydrogen can exist in lower-energy states than previously thought possible and support the existence of these states called hydrino, for "small hydrogen," and the corresponding hydride ions and molecular hydrino. Some of these prior related studies supporting the possibility of a novel reaction of atomic hydrogen, which produces hydrogen in fractional quantum states that are at lower energies than the traditional "ground" ($n = 1$) state, include extreme ultraviolet (EUV) spectroscopy, characteristic emission from catalysts and the hydride ion products, lower-energy hydrogen emission, chemically-formed plasmas, Balmer α line

broadening, population inversion of H lines, elevated electron temperature, anomalous plasma afterglow duration, power generation, and analysis of novel chemical compounds [13-31, 41-54].

He^+ fulfills the catalyst criterion—a chemical or physical process with an enthalpy change equal to an integer multiple of $27.2\ eV$ since it ionizes at $54.417\ eV$, which is $2 \cdot 27.2\ eV$. Two hydrogen atoms may also serve as the catalyst of the same enthalpy. As given in Chp. 5 of Ref [1], and Refs. [13-14], hydrogen atoms $H(1/p)$ $p = 1, 2, 3, ... 137$ can undergo further transitions to lower-energy states given by Eqs. (1) and (3) wherein the transition of one atom is catalyzed by a second that resonantly and nonradiatively accepts $m \cdot 27.2\ eV$ with a concomitant opposite change in its potential energy. The overall general equation for the transition of $H(1/p)$ to $H(1/(p+m))$ induced by a resonance transfer of $m \cdot 27.2\ eV$ to $H(1/p')$ is represented by

$$H(1/p') + H(1/p) \rightarrow H + H(1/(p+m)) + \left[2pm + m^2 - p'^2 + 1 \right] \cdot 13.6\ eV \tag{23}$$

Hydrogen atoms may serve as a catalyst wherein $m = 1$ and $m = 2$ for one and two atoms, respectively, acting as a catalyst for another. The rate for the two-atom-catalyst, $2H$, may be high when extraordinarily fast H as reported previously [13-26] collides with a molecule to form the $2H$ wherein two atoms resonantly and nonradiatively accept $54.4\ eV$ from a third hydrogen atom of the collision partners.

With $m = 2$, the product of catalysts He^+ and $2H$ is $H(1/3)$ that reacts rapidly to form $H(1/4)$, then molecular hydrino, $H_2(1/4)$, as a preferred state. Specifically, in the case of a high hydrogen atom concentration, the further transition given by Eq. (23) of $H(1/3)$ ($p = 3$) to $H(1/3)$ ($p + m = 4$) with H as the catalyst ($p' = 1$; $m = 1$) can be fast:

$$H(1/3) \xrightarrow{\ H\ } H(1/4) + 95.2\ eV \tag{24}$$

The corresponding molecular hydrino $H_2(1/4)$ and hydrino hydride ion $H^-(1/4)$ are preferred final products consistent with observation since the $p = 4$ quantum state has a multipolarity greater than that of a quadrupole giving it, $H(1/4)$, a long theoretical lifetime [14] for further catalysis.

The nonradiative energy transfer to the catalysts, He^+ and $2H$, is predicted to pump the He^+ ion energy levels and increase the electron excitation temperature of H in helium-hydrogen and hydrogen plasmas, respectively. For both catalysts, the intermediate $H*\left[\dfrac{a_H}{2+1} \right]$ (Eq. (6) with $m = 2$) has the radius of the hydrogen atom (corresponding to the 1 in the denominator) and a central field equivalent to 3 times that of a proton, and $H\left[\dfrac{a_H}{3} \right]$ is the corresponding stable state with the radius of 1/3 that of H. As the electron undergoes radial acceleration from the radius of the hydrogen atom to a radius of 1/3 this distance, energy is released as characteristic light emission or as third-body kinetic energy. The emission may be in the form of extreme-ultraviolet continuum radiation having an edge at $54.4\ eV$ (22.8 nm) and extending to longer wavelengths. Alternatively, fast H is predicted due to a resonant kinetic-energy transfer. A secondary continuum band is predicted arising from the subsequently rapid transition of the catalysis product $\left[\dfrac{a_H}{3} \right]$ (Eqs. (6-9) and (24)) to the $\left[\dfrac{a_H}{4} \right]$ state wherein atomic

hydrogen accepts $27.2 \; eV$ from $\left[\dfrac{a_H}{3} \right]$ [1, 13]. Extreme ultraviolet (EUV) spectroscopy and high-resolution visible spectroscopy were recorded on microwave and glow and pulsed discharges of helium with hydrogen and hydrogen alone providing catalysts He^+ and $2H$, respectively [13]. Pumping of the He^+ ion lines occurred with the addition of hydrogen, and the excitation temperature of hydrogen plasmas under certain conditions was very high. The EUV continua at both 22.8 nm and 40.8 nm were observed and extraordinary (>50 eV) Balmer α line broadening was observed. $H_2 \, (1/4)$ was observed by solution NMR at 1.25 ppm on gases collected from helium-hydrogen, hydrogen, and water-vapor-assisted hydrogen plasmas and dissolved in $CDCl_3$.

Similarly, the reaction Ar^+ to Ar^{2+} has a net enthalpy of reaction of $27.63 \; eV$, which is equivalent to $m = 1$ in Eqs. (6-9). When Ar^+ served as the catalyst its predicted 91.2 nm and 45.6 nm continua were observed as well as the other characteristic signatures of hydrino transitions, pumping of the catalyst excited states, fast H, and the predicted gaseous hydrino product $H_2 \, (1/4)$ that was observed by solution NMR at 1.25 ppm. Considering these results and those of hydrogen and helium-hydrogen plasmas, the $q \cdot 13.6 \; eV$ continua have been observed with thresholds at $54.4 \; eV$ ($q = 4$) for $2H$ catalyst, $54.4 \; eV$ ($q = 4$) and $40.8 \; eV$ ($q = 3$) for He^+ catalyst, and $27.2 \; eV$ ($q = 2$) and $13.6 \; eV$ ($q = 1$) for Ar^+ catalyst. Much higher values of q are possible with transitions of hydrinos to lower states giving rise to high-energy continuum radiation over a broad spectral region as reported previously [13]. These results have further implications for the resolution of many celestial mysteries such as the paradox of the identity of dark matter and the identity of the radiation source behind the observation that diffuse $H\alpha$ emission is ubiquitous throughout the Galaxy and widespread sources of flux shortward of $912 \; \mathring{A}$ are required [13].

In recent power generation and product characterization studies [14], atomic lithium and molecular NaH served as catalysts since they meet the catalyst criterion—a chemical or physical process with an enthalpy change equal to an integer multiple m of the potential energy of atomic hydrogen, $27.2 \; eV$ (e.g. $m = 3$ for Li and $m = 2$ for NaH). Specific predictions based on closed-form equations for energy levels of the corresponding hydrino hydride ion H^- (1/4) of novel alkali halido hydrino hydride compounds ($MH * X$; $M = Li \; or \; Na$, $X = halide$) and molecular hydrino $H_2 \, (1/4)$ were tested using chemically generated catalysis reactants.

First, Li catalyst was tested. Li and $LiNH_2$ were used as a source of atomic lithium and hydrogen atoms. Using water-flow, batch calorimetry, the measured power from 1g Li, 0.5g $LiNH_2$, 10g $LiBr$, and 15g Pd / Al_2O_3 was about 160W with an energy balance of $\Delta H = -19.1 \; kJ$. The observed energy balance was 4.4 times the maximum theoretical based on known chemistry. Next, Raney nickel (R-Ni) served as a dissociator when the power reaction mixture was used in chemical synthesis wherein $LiBr$ acted as a getter of the catalysis product $H \, (1/4)$ to form $LiH * X$ as well as to trap $H_2 \, (1/4)$ in the crystal. The ToF-SIMs showed $LiH * X$ peaks. The ^1H MAS NMR $LiH * Br$ and $LiH * I$ showed a large distinct upfield resonance at about –2.5 ppm that matched $H^- \, (1/4)$ in a LiX matrix. An NMR peak at 1.13 ppm matched interstitial $H_2 \, (1/4)$, and the rotation frequency of $H_2 \, (1/4)$ of 4^2 times that of ordinary H_2 was observed at $1989 \; cm^{-1}$ in the FTIR spectrum. The XPS spectrum recorded on the

*LiH * Br* crystals showed peaks at about 9.5 eV and 12.3 eV that could not be assigned to any known elements based on the absence of any other primary element peaks, but matched the binding energy of H^- (1/4) in two chemical environments. A further signature of the energetic process was the observation of the formation of a plasma called a resonant transfer- or rt-plasma at low temperatures (e.g. $\approx 10^3 \, K$) and very low field strengths of about 1-2 V/cm when atomic *Li* was present with atomic hydrogen. Time-dependent line broadening of the *H* Balmer α line was observed corresponding to extraordinarily fast *H* (>40 eV).

A compound comprising hydrogen such as *MH*, where M is an element other than hydrogen, serves as a source of hydrogen and a source of catalyst. A catalytic reaction is provided by the breakage of the $M - H$ bond plus the ionization of t electrons from the atom *M* each to a continuum energy level such that the sum of the bond energy and ionization energies of the t electrons is approximately $m \cdot 27.2 \, eV$, where m is an integer. One such catalytic system involves sodium. The bond energy of *NaH* is 1.9245 eV [55], and the first and second ionization energies of *Na* are 5.13908 eV and 47.2864 eV, respectively [33]. Based on these energies the *NaH* molecule can serve as a catalyst and *H* source, since the bond energy of *NaH* plus the double ionization ($t = 2$) of *Na* to Na^{2+} is 54.35 eV ($2 \cdot 27.2 \, eV$). The concerted catalyst reactions are given by

$$54.35 \ eV + NaH \rightarrow Na^{2+} + 2e^- + H\left[\frac{a_H}{3}\right] + [3^2 - 1^2] \cdot 13.6 \ eV \tag{25}$$

$$Na^{2+} + 2e^- + H \rightarrow NaH + 54.35 \ eV \tag{26}$$

And, the overall reaction is

$$H \rightarrow H\left[\frac{a_H}{3}\right] + [3^2 - 1^2] \cdot 13.6 \ eV \tag{27}$$

The product $H(1/3)$ reacts rapidly to form $H(1/4)$, then molecular hydrino, $H_2(1/4)$, as a preferred state (Eq. (24)). The *NaH* catalyst reactions may be concerted since the sum of the bond energy of *NaH*, the double ionization ($t = 2$) of *Na* to Na^{2+}, and the potential energy of *H* is 81.56 eV ($3 \cdot 27.2 \, eV$). The catalyst reactions are given by

$$81.56 \ eV + NaH + H \rightarrow Na^{2+} + 2e^- + H_{fast}^+ + e^- + H\left[\frac{a_H}{4}\right] + [4^2 - 1^2] \cdot 13.6 \ eV \tag{28}$$

$$Na^{2+} + 2e^- + H + H_{fast}^+ + e^- \rightarrow NaH + H + 81.56 \ eV \tag{29}$$

And, the overall reaction is

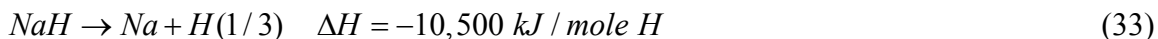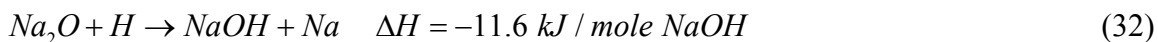$$H \rightarrow H\left[\frac{a_H}{4}\right] + [4^2 - 1^2] \cdot 13.6 \ eV \tag{30}$$

where H_{fast}^+ is a fast hydrogen atom having at least 13.6 eV of kinetic energy. H^- (1/4) forms stable halido hydrides and is a favored product together with the corresponding molecule formed by the reactions $2H(1/4) \rightarrow H_2(1/4)$ and $H^-(1/4) + H^+ \rightarrow H_2(1/4)$ [13-17, 27-31, 45].

Sodium hydride is typically in the form of an ionic crystalline compound formed by the reaction of gaseous hydrogen with metallic sodium. And, in the gaseous state, sodium comprises covalent Na_2 molecules [56] with bond energy of 74.8048 kJ/mole [57]. It was found that when $NaH(s)$ was heated at a very slow temperature ramp rate (0.1 °C/min) under a helium atmosphere to form $NaH(g)$, the predicted exothermic reaction given by Eqs. (25-27) was
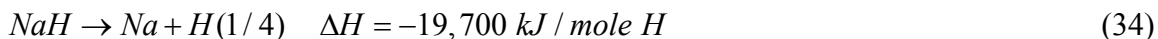
observed at high temperature by differential scanning calorimetry (DSC) [14]. To achieve high power, a chemical system was designed to greatly increase the amount and rate of formation of $NaH(g)$. The reaction of $NaOH$ and Na to Na_2O and $NaH(s)$ calculated from the heats of formation [55, 57] releases $\Delta H = -44.7 \ kJ \ / \ mole \ NaOH$:

$$NaOH + 2Na \rightarrow Na_2O + NaH(s) \quad \Delta H = -44.7 \ kJ \ / \ mole \ NaOH \qquad (31)$$
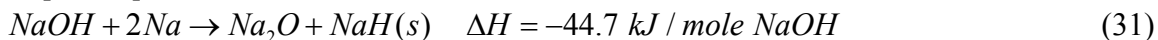
This exothermic reaction can drive the formation of $NaH(g)$ and was exploited to drive the very exothermic reaction given by Eqs. (25-27). The regenerative reaction in the presence of atomic hydrogen is

$$Na_2O + H \rightarrow NaOH + Na \quad \Delta H = -11.6 \ kJ \ / \ mole \ NaOH \qquad (32)$$

$$NaH \rightarrow Na + H(1/3) \quad \Delta H = -10,500 \ kJ \ / \ mole \ H \qquad (33)$$

and

$$NaH \rightarrow Na + H(1/4) \quad \Delta H = -19,700 \ kJ \ / \ mole \ H \qquad (34)$$

NaH uniquely achieves high kinetics since the catalyst reaction relies on the release of the intrinsic H, which concomitantly undergoes the transition to form $H(1/3)$ that further reacts to form $H(1/4)$. High-temperature differential scanning calorimetry (DSC) was performed on ionic NaH under a helium atmosphere at an extremely slow temperature ramp rate (0.1 °C/min) to increase the amount of molecular NaH formation. A novel exothermic effect of $-177 \ kJ \ / \ moleNaH$ was observed in the temperature range of 640 °C to 825 °C. To achieve high power, R-Ni having a surface area of about 100 $m^2 \ / \ g$ was surface-coated with $NaOH$ and reacted with Na metal to form NaH. Using water-flow, batch calorimetry, the measured power from 15g of R-Ni was about 0.5 kW with an energy balance of $\Delta H = -36 \ kJ$ compared to $\Delta H \approx 0 \ kJ$ from the R-Ni starting material, R-NiAl alloy, when reacted with Na metal. The observed energy balance of the NaH reaction was $-1.6X10^4 \ kJ \ / \ mole \ H_2$, over 66 times the $-241.8 \ kJ \ / \ mole \ H_2$ enthalpy of combustion. With an increase in $NaOH$ doping to 0.5 wt%, the Al of the R-Ni intermetallic served to replace Na metal as a reductant to generate NaH catalyst. When heated to 60 °C, 15g of the composite catalyst material required no additive to release 11.7 kJ of excess energy and develop a power of 0.25 kW. Solution NMR on product gases dissolved in DMF-d7 showed H_2 (1/4) at 1.2 ppm.

The ToF-SIMs showed sodium hydrino hydride, NaH_x, peaks. The ^1H MAS NMR spectra of $NaH*Br$ and $NaH*Cl$ showed large distinct upfield resonances at –3.6 ppm and –4 ppm, respectively, that matched H^- (1/4), and an NMR peak at 1.1 ppm matched H_2 (1/4). $NaH*Cl$ from reaction of $NaCl$ and the solid acid $KHSO_4$ as the only source of hydrogen comprised two fractional hydrogen states. The H^- (1/4) NMR peak was observed at –3.97 ppm, and the H^- (1/3) peak was also present at –3.15 ppm. The corresponding H_2 (1/4) and H_2 (1/3) peaks were observed at 1.15 ppm and 1.7 ppm, respectively. ^1H NMR of $NaH*F$ dissolved in DMF-d7 showed isolated H_2 (1/4) and H^- (1/4) at 1.2 ppm and –3.86 ppm, respectively, wherein the absence of any solid matrix effect or the possibility of alternative assignments confirmed the solid NMR assignments. The XPS spectrum recorded on $NaH*Br$ showed the H^- (1/4) peaks at about 9.5 eV and 12.3 eV that matched the results from $LiH*Br$ and $KH*I$; whereas, sodium hydrino hydride showed two fractional hydrogen states additionally having the H^- (1/3) XPS peak at 6 eV in the absence of a halide peak. The predicted rotational transitions having

energies of 4^2 times those of ordinary H_2 were also observed from H_2 (1/4) which was excited using a 12.5 keV electron beam.

Using the NaH solid fuel, the energy scaled linearly and the power increased nonlinearly wherein the reaction of 1 kg 0.5 wt% $NaOH$-doped R-Ni liberated 753.1 kJ of energy to develop a power in excess of 50 kW. Albeit conventional reactions contribute negligibly to the energy balance, the excess energy of the batch run was far less than the theoretical maximum energy release due to hydrino formation. This indicates that reactions such as the formation of a sodium aluminate or alumina surface layer terminate the catalytic cycle given by Eqs. (31-34). In principle, the solid fuel can be regenerated and the hydrino reaction can be repeated in a perpetual cycle with hydrogen added back to replace that converted to hydrinos. Another option is to apply a chemical process that can easily regenerate the solid fuel from readily separable components.

In this paper, we report hydrino reactions based on heterogeneous catalysts that developed high power, energy output and energy gain. In addition, both hydrino-species, molecular hydrino and hydrino hydride ions, were readily isolated from the reaction products. The reaction to cause a transition of atomic hydrogen to form hydrinos requires a catalyst such as Li, K, or NaH and atomic hydrogen wherein NaH serves as a catalyst and source of atomic hydrogen in a concerted reaction. The typical metallic form of Li and K were converted to the atomic form and the ionic form of NaH was converted to the molecular form by using a support such as an activated carbon (AC) having a surface area of 900 m^2/g to disperse Li and K atoms and NaH molecules, respectively. The reaction step (Eq. (6)) of a nonradiative energy transfer of an integer multiple of 27.2 eV from atomic hydrogen to the catalyst results in an ionized catalyst and free electrons that causes the reaction to rapidly cease due to charge accumulation. The support also acted as a conductive electron acceptor of electrons released from the catalyst reaction that formed the hydrinos. Each reaction mixture further comprised an oxidant to serve as a scavenger of electrons from the conductive support and a final electron-acceptor reactant as well as a weak reductant to assist the oxidant's function. In some cases, the concerted electron-acceptor (oxidation) reaction was also very exothermic to heat the reactants and enhance the rates to produce power or hydrino compounds. The energy balances of the heterogeneous catalyst systems were measured by water-flow calorimetry, and the hydrino products were characterized by ^1H NMR, ToF-SIMs, and XPS. The heat was also recorded on a 10-fold scale-up reaction.

II. Experimental
A. Heterogeneous Catalyst Mixtures

Each reaction mixture comprised (i) a catalyst from the group of LiH, KH, and NaH, (ii) an oxidant from the group of $NiBr_2$, MnI_2, $AgCl$, $EuBr_2$, SF_6, S, CF_4, NF_3, $LiNO_3$, $M_2S_2O_8$ with Ag, and P_2O_5, (iii) a reductant from the group of Mg powder, or MgH_2, Al powder, or aluminum nano-powder (Al NP), Sr, and Ca, and (iv) a support from the group of AC, YC$_2$ and TiC. Compounds were from Sigma Aldrich, Alfa Aesar, or Strem Chemicals. Inc. Gases were from Spectra Gases Inc. or GTS-Welco. The reactants were loaded in a glove box under an argon atmosphere and mixed by ball milling in hermetically sealed vessels or by using a blender in the glove box. The mixture was loaded in the cell in the glove box and the cell was sealed with a high temperature valve that was used to evacuate the cell once removed from the glove box and then pressurize it with gas (in the case of heterogeneous reaction mixtures with a

gas oxidant). The moles ($\pm 0.1\%$) of gas added to the cell were determined using the ideal gas law with the measured pressure difference upon filling from a reservoir of an accurately known volume. The corresponding controls comprised permutations having one essential reactive catalysis component missing from the reaction mixture. In addition, control calorimetric chemical reactions were run comprising the decomposition of NH_4NO_3 and the reaction of Mg with Fe_2O_3.

Before use, the activated carbon was dried under vacuum at 300 °C for 48 hours. Quantitative XRD showed 99.8% carbon and 0.2% SiO_2. TiC or YC_2 was also dried under vacuum at 300 °C for 48 hours. For all reactants that could form a hydrate, the anhydrous compound was used when commercially available. Otherwise, they were dried under vacuum. The water content of any reactant was determined to be less than 10^{-5} moles/g except EuBr$_2$ that was 10^{-4} moles/g as received. The measurement was by desorption studies using physical gas parameter determination (P, V, T), mass spectroscopy, and quantitative gas chromatography as described previously [14].

Quantitative X-ray diffraction (XRD) was performed on the reaction products using hermetically sealed sample holders (Bruker Model #A100B37) loaded in a glove box under argon, wax sealed, and analyzed with a Siemens D5000 diffractometer using Cu radiation at 40kV/30mA over the range 10°–70° with a step size of 0.02° and a counting time of eight hours. Mass spectroscopy and quantitative GC on the product gases showed some methane that had a negligible impact on the heat balance.

B. Water-Flow, Batch Calorimetry. A schematic of the cylindrical stainless steel reactors of approximately 130.3 cm^3 volume (1.5" inside diameter (ID), 4.5" length, and 0.2" wall thickness) and 1988 cm^3 volume (3.75" inside diameter (ID), 11" length, and 0.375" wall thickness) are shown in Figure 1. The water flow calorimeter comprising a vacuum chamber containing each cell and an external water coolant coil that collected 99+% of the energy released in the cell to achieve an error $< \pm 1\%$ is shown in Figure 2. Both the cells and water-flow calorimeter were described previously [14]. The energy recovery was determined by integrating the total output power P_T over time. The power was given by

$$P_T = \dot{m} C_p \Delta T \tag{35}$$

where $\dot{m}$ was the mass flow rate, C_p was the specific heat of water, and ΔT was the absolute change in temperature between the inlet and outlet. The reaction was initiated by applying precision power to external resistive heaters. Specifically, 100-200 W of power (130.3 cm^3 cell) or 800-1000 W (1988 cm^3 cell) was supplied to the heater. During this heating period, the reagents reached a temperature threshold wherein the onset of the hydrino reaction was typically confirmed by a rapid rise in cell temperature. Once the cell temperature reached about 400-500 °C the input power was set to zero. After 50 minutes, the program directed the power to zero. To increase the rate of heat transfer to the coolant, the chamber was re-pressurized with 1000 Torr of helium as described previously [14], and the maximum change in water temperature (outlet minus inlet) was approximately 1.2 °C. The assembly was allowed to fully reach equilibrium over a 24-hour period as confirmed by the observation of full equilibrium in the flow thermistors.

C. Solution NMR. 50 mg of reaction product or samples of *NaHS* or *NaOH* were added to 1.5 ml of deuterated N,N-dimethylformamide-d7 ($DCONCD_3)_2$, DMF-d7, D_2O or deuterated DMSO-d6 (99.5% Cambridge Isotope Laboratories, Inc.) in a vial that was sealed with a glass Teflon valve, agitated, and allowed to dissolve over a 12 hour-period in a glove box under an argon atmosphere. In addition, H_2S was bubbled into *NaOH* solutions to a desired pH. The solution in the absence of any solid was transferred to an NMR tube (5 mm OD, 23 cm length, Wilmad) by a gas-tight connection, followed by flame-sealing of the tube. Additional control NMR samples comprised the starting materials added to the NMR solvent with the dissolved portion analyzed. The NMR spectra were recorded with a 500 MHz Bruker NMR spectrometer that was deuterium locked. The chemical shifts were referenced to the solvent frequency such as DMF-d7 at 8.03 ppm relative to TMS.

D. ToF-SIMS Spectra. The crystalline samples were sprinkled onto the surface of a double-sided adhesive tape and characterized using a Physical Electronics TFS-2000 ToF-SIMS instrument. The primary ion gun utilized a $^{69}Ga^+$ liquid metal source. A region on each sample of $(60 \mu m)^2$ was analyzed. In order to remove surface contaminants and expose a fresh surface, the samples were sputter-cleaned for 60 seconds using a $180 \mu m$ X $100 \mu m$ raster. The aperture setting was 3, and the ion current was 600 pA resulting in a total ion dose of 10^{15} $ions/cm^2$.

During acquisition, the ion gun was operated using a bunched (pulse width 4 ns bunched to 1 ns) 15 kV beam [58-59]. The total ion dose was 10^{12} $ions/cm^2$. Charge neutralization was active, and the post accelerating voltage was 8000 V. The positive and negative SIMS spectra were acquired. Representative post sputtering data is reported.

E. XPS Spectra. A series of XPS analyses were made on the crystalline samples using a Scienta 300 XPS Spectrometer. The fixed analyzer transmission mode and the sweep acquisition mode were used. The step energy in the survey scan was $0.5 \, eV$, and the step energy in the high-resolution scan was $0.15 \, eV$. In the survey scan, the time per step was 0.4 seconds, and the number of sweeps was 4. In the high-resolution scan, the time per step was 0.3 seconds, and the number of sweeps was 30. $C \, 1s$ at $284.5 \, eV$ was used as the internal standard.

F. Synthesis and Solid ^1H MAS NMR of $LiH*$. Lithium hydrinohydrides in a sulfur matrix were synthesized by reaction of hydrogen with 1.32g $LiH(s)$ + 3g Al powder + 12g AC + 3.9g S (Alfa Aesar). The compounds were prepared in a stainless steel gas cell (Figure 3) according to the methods described previously [14]. The reactor was run at 360 °C in a kiln for 4 hours. Then, the reactor was cooled under helium atmosphere. The sealed reactor was then opened in a glove box under an argon atmosphere. NMR samples were extracted with DMF-d7 and placed in glass ampules, sealed with rubber septa, and transferred out of the glove box to be flame sealed.

III. Results and Discussion
A. Water-Flow Calorimetry Power Measurements. The experimental net energy, calculated theoretical maximum energy for conventional chemistry [60-62], excess energy due to the hydrino reaction, the peak power, and energy gain of heterogeneous hydrino catalyst systems comprising reactants of (i) *NaH* or *KH*, (ii) *Mg* and (iii) $NiBr_2$, MnI_2, *AgCl* or $EuBr_2$ mixed

with AC, YC_2 or TiC are given in Table 2. In each test, the energy input and energy output were calculated by integration of the corresponding power as described previously [14]. The thermal energy in the coolant flow in each time increment was calculated using Eq. (35) by multiplying volume flow rate of water by the water density at 19 °C (0.998 kg/liter), the specific heat of water (4.181 kJ/kg °C), the corrected temperature difference, and the time interval. Values were summed over the entire experiment to obtain the total energy output. The total energy from the cell E_T must equal the energy input E_{in} and any net energy E_{net}. Thus, the net energy was given by

$$E_{net} = E_T - E_{in} \tag{36}$$

From the energy balance, any excess heat E_{ex} was determined relative to the maximum theoretical E_{mt} by

$$E_{ex} = E_{net} - E_{mt} \tag{37}$$

The calibration test results demonstrated a heat coupling of better than 98% of the resistive input to the output coolant, and zero excess heat controls demonstrated that with the calibration correction applied, the calorimeter was accurate to within less than 1% error [14].

The control decomposition reaction of NH_4NO_3 to N_2O and H_2O calculated from the heats of formation [60-62] is exothermic by $\Delta H = -124.4 \ kJ \ / \ mole \ NH_4NO_3$:

$$NH_4NO_3 \rightarrow N_2O + 2H_2O \tag{38}$$
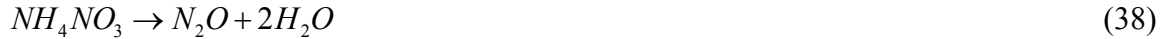
At elevated temperature, further decomposition occurs. The decomposition reaction energy of NH_4NO_3 to N_2, O_2, and H_2O calculated from the heats of formation [60-62] is exothermic by $\Delta H = -206 \ kJ \ / \ mole \ NH_4NO_3$:

$$NH_4NO_3 \rightarrow N_2 + 1/2O_2 + 2H_2O \tag{39}$$

For 10 g NH_4NO_3, the theoretical energy is 25.736 kJ. The gaseous products from the decomposition reaction run to 380 °C were determined by quantitative gas chromatography. The experimental energy balance was 23 kJ which compared well with the theoretical of 24.99 kJ corresponding to a 0.927 mole-fraction contribution of the reaction of Eq. (39) and a 0.073 mole-fraction contribution of the reaction given by Eq. (38).

The control reaction of $Mg + Fe_2O_3$ to MgO calculated from the heats of formation [60-62] is exothermic by $\Delta H = -326.87 \ kJ \ / \ mole \ Mg$ or $\Delta H = -980.6 \ kJ \ / \ mole \ Fe_2O_3$:

$$3Mg + Fe_2O_3 \rightarrow 3MgO + 2Fe \tag{40}$$

For 2.43g Mg and 5.34g Fe_2O_3, the theoretical energy is 32.75 kJ. The experimental energy balance was 30 kJ.

Control reactions of heterogeneous catalysts were performed with the support absent and with the catalyst absent. The energy balances matched or were below the maximum theoretical. Other permutations involving the absence of one or more components of a given system were tested, and it was found that the optimum energy gain was achieved when all of the components of the heterogeneous reaction systems given in Table 2 were present.
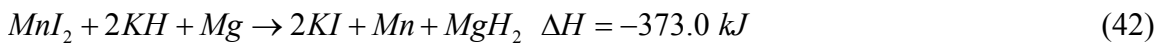
The cell temperature with time due to the indicated constant power and the coolant power with time for the heterogeneous catalyst mixture, 5.0g $NaH(s)$ + 5.0g Mg + 20.0g AC + 11.0g $NiBr_2$, are shown in Figures 4 and 5, respectively. The numerical integration of the input and output power curves with the calibration correction applied yielded the output energy of 277 kJ

and an input energy of 224 kJ. Thus, from Eq. (36), the net energy was 53 kJ. In the plot of Figure 4, there is a point at which the slope of the temperature changes almost discontinuously at 160 °C due to the cell temperature rising rapidly with the onset of reaction. Based on the system response to a power pulse, the net energy of 53 kJ occurred in about 30 s that places the power for the reaction at over 1.75 kW. The calculated theoretical maximum energy for conventional chemistry based on the limiting reagent of 0.05 moles of $NiBr_2$ is 26.25 kJ for the reaction:

$$NiBr_2 + 2NaH + 3Mg \rightarrow 2NaBr + Mg_2Ni + MgH_2 \quad \Delta H = -524.70 \; kJ \tag{41}$$

The XRD results showed products predicted by Eq. (41) at ratios short of the reactants going to completion. Thus, the excess energy and gain (Eq. (37)) were at least 26.75 kJ and 2 times the maximum by conventional chemistry.

The cell temperature with time due to the indicated constant power and the coolant power with time for the heterogeneous catalyst mixture, 8.3g $KH(s)$ + 5.0g Mg + 20.0g TiC + 15.45g MnI_2, are shown in Figures 6 and 7, respectively. The numerical integration of the input and output power curves with the calibration correction applied yielded the output energy of 318 kJ and an input energy of 269 kJ. Thus, from Eq. (36), the net energy was 49 kJ. In the plot of Figure 6, there is a point at which the slope of the temperature changes almost discontinuously at 50 °C due to the cell temperature rising more rapidly with the onset of reaction. Based on the system response to a power pulse, the net energy of 49 kJ occurred in about 60 s that places the power for the reaction at about 0.8 kW. The calculated theoretical maximum energy for conventional chemistry based on the limiting reagent of 0.05 moles of MnI_2 is 18.65 kJ for the reaction:

$$MnI_2 + 2KH + Mg \rightarrow 2KI + Mn + MgH_2 \quad \Delta H = -373.0 \; kJ \tag{42}$$

The XRD results showed products predicted by Eq. (42) at ratios short of the reactants going to completion. Thus, the excess energy and gain (Eq. (37)) were at least 30.35 kJ and 2.6 times the maximum by conventional chemistry.

The cell temperature with time due to the indicated constant power and the coolant power with time for the heterogeneous catalyst mixture, 8.3g $KH(s)$ + 5.0g Mg + 20.0g AC + 7.2g $AgCl$, are shown in Figures 8 and 9, respectively. The numerical integration of the input and output power curves with the calibration correction applied yielded the output energy of 367.52 kJ and an input energy of 327.1 kJ. Thus, from Eq. (36), the net energy was 40.42 kJ. In the plot of Figure 8, there is a point at which the slope of the temperature changes almost discontinuously at 288 °C due to the cell temperature rising more rapidly with the onset of reaction. Based on the system response to a power pulse, the net energy of 40.42 kJ occurred in about 60 s that places the power for the reaction at about 0.67 kW. The calculated theoretical maximum energy for conventional chemistry based on the limiting reagent of 0.05 moles of $AgCl$ is 14.52 kJ for the reaction:

$$AgCl + KH + 0.5Mg \rightarrow KCl + Ag + 0.5MgH_2 \quad \Delta H = -289.44 \; kJ \tag{43}$$
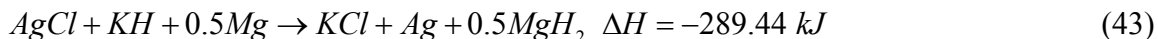
The XRD results showed products predicted by Eq. (43) at ratios short of the reactants going to completion. Thus, the excess energy and gain (Eq. (37)) were at least 25.9 kJ and 2.78 times the maximum by conventional chemistry.

The cell temperature with time due to the indicated constant power and the coolant power with time for the heterogeneous catalyst mixture, 8.3g $KH(s)$ + 5.0g Mg + 20.0g TiC + 15.6g $EuBr_2$, are shown in Figures 10 and 11, respectively. The numerical integration of the input and

output power curves with the calibration correction applied yielded the output energy of 336 kJ and an input energy of 291 kJ. Thus, from Eq. (36), the net energy was 45 kJ. In the plot of Figure 10, there is a point at which the slope of the temperature changes almost discontinuously at 50 °C due to the cell temperature rising more rapidly with the onset of reaction. Based on the system response to a power pulse, the net energy of 45 kJ occurred in about 60 s that places the power for the reaction at about 0.75 kW. The calculated theoretical maximum energy for conventional chemistry based on the limiting reagent of 0.05 moles of $EuBr_2$ is 6.85 kJ for the reaction:

$$EuBr_2 + 2KH \rightarrow 2KBr + EuH_2 \quad \Delta H = -136.55 \; kJ \tag{44}$$
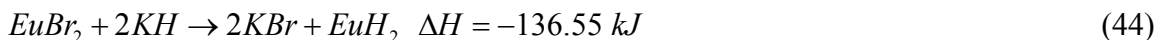
The XRD results showed products predicted by Eq. (44) at ratios short of the reactants going to completion. Assuming completion, the excess energy and gain (Eq. (37)) were 38.2 kJ and 6.6 times the maximum by conventional chemistry, respectively. However, using the heats of reaction, the theoretical energy balance from known chemistry based on the XRD-observed products and molar percentages was $\Delta H = +1.92 \; kJ / mole \; EuBr_2$. The actual excess energy and gain relative to conventional chemistry were 45 kJ and infinite, respectively. Therefore, the energy gain was limited by the $50 \; MJ / mole \; H_2$ for the formation of H_2 (1/4), an ideal for these heterogeneous catalyst systems.

The only exothermic reaction possible to account for the large excess energy balances summarized in Table 2 is that given by Eqs. (6-9). The reaction was then scaled-up 10 fold to determine the scaling behavior. The cell temperature with time due to the indicated constant power and the coolant power with time for the hydrino reaction mixture of 50.0g $NaH(s)$ + 50.0g Mg + 200.0g AC + 109.5g $NiBr_2$, are shown in Figures 12 and 13, respectively. The numerical integration of the input and output power curves yielded the output energy of 2567 kJ and an input energy of 1990 kJ corresponding to a net energy of 577 kJ. The cell developed a system-response-corrected peak power in excess of 30 kW initiated at 140 °C. From Eq. (41), the calculated theoretical maximum energy for conventional chemistry based on the limiting reagent of 0.5 moles of $NiBr_2$ is 262.5 kJ such that the excess energy and gain (Eq. (37)) were at least 314.5 kJ and 2.19 times the maximum by conventional chemistry. Thus, the energy and power scaled linearly.

B. NMR Identification of H_2 (1/4) and H^- (1/4). The ^1H solution NMR following DMF-d7 solvent extraction of the product of the reaction mixture comprising 1g $NaH(s)$ + 1g MgH_2 mixed with 4g activated carbon and pressurized with 0.0094 moles of SF_6 (Figure 14) showed a sharp singlet at –3.84 ppm that matched H^- (1/4). This assignment was supported by the calorimetric measurement on this reaction. The numerical integration of the input and output power curves with the calibration correction applied yielded the output energy of 129.8 kJ and an input energy of 96.7 kJ. Thus, from Eq. (36), the net energy was 33.1 kJ. The cell temperature changed discontinuously at 110 °C and rose to 455 °C in about 30s with the onset of reaction corresponding to a power for the reaction of over 1.1 kW. The calculated theoretical maximum energy for conventional chemistry based on the limiting reagent of 0.0094 moles of SF_6 is 20.87 kJ for the reaction:

$$2NaH + 3MgH_2 + SF_6 \rightarrow 2NaMgF_3 + 4H_2 + MgS \quad \Delta H = -2220.02 \; kJ \tag{45}$$

The XRD results showed products predicted by Eq. (45) at ratios short of the reactants going to completion with the formation of 3.7wt% $NaHS$ and 7.4wt% MgF_2. Thus, the excess energy and gain (Eq. (37)) were at least 12.2 kJ and 1.6 times the maximum by conventional chemistry.

The other peaks in the spectrum shown in Figure 14 are due to DMF-d7 except for the background trace water peak at 3.62 ppm and background hydrocarbon peaks from AC. To eliminate a species formed by reaction of the solvent with the reaction product of 1g $NaH(s)$ + 1g MgH_2 + 4g AC + 0.01 moles of SF_6, the extraction was also performed with DMSO-d6 and the results (Figure 15) were very similar showing a sharp singlet at –4.07 ppm. The slight difference was attributed to a minor solvent effect. Using Eq. (11) with $p = 4$ and the experimental absolute resonance shift of TMS, –31.5 ppm, the predicted gas-phase shift of H^- (1/4) is

$$\frac{\Delta B_T}{B} = -(29.9 + 1.37(4))\,ppm - (-31.5\,ppm)$$
$$= -35.38\,ppm - (-31.5\,ppm) \tag{46}$$
$$= -3.88\,ppm$$

which is extraordinarily close to the observed shift of –3.84 ppm (Figure 14) and –4.07 ppm (Figure 15). ToF-SIMs having a detection limit below parts per million (ppm) level showed no metals in the reaction product other than alkali metals (predominantly sodium), magnesium, fluoride, hydride, and sulfur. Thus, there is no other possible assignment of the upfield-shifted peak based on the elements present other than H bound to S. To eliminate this assignment the water reactivity of the –3.84 ppm peak was determined and controls for H bound to S were recorded.

The extracted reaction product of 1g $NaH(s)$ + 1g MgH_2 + 4g AC + 0.0094 moles of SF_6, having the NMR shown in Figure 14 was heated in an inert atmosphere to 50 °C with trace water. As shown in Figure 16, the peak shifted slightly to –3.74 ppm and decreased and broadened significantly. Concomitantly, the water peak became broader indicating a water interaction. When this reaction was repeated with increasing amount of water, the effect on the –3.84 ppm and water peaks increased. In all cases, the –3.84 ppm peak was eliminated with further heating or with larger amounts of water and nominal heating. These results indicate that the hydrino hydride ion is more stable than ordinary hydride, but reacts at sufficiently high concentration and with heating. Thus, it was anticipated that hydrino hydride dissolved in water would react completely and there would be no –3.84 ppm peak in D_2O; whereas, species such as HS^- do not react with water [63]. The former was confirmed experimentally.

Next, H bound to S was investigated. One of the minor reaction products of 1g $NaH(s)$ + 1g MgH_2 + 4g AC + 0.0094 moles of SF_6, was $NaHS$. Since $NaHS$ comprises a source of the catalyst NaH and the hydrino hydride getter S, hydrino hydride H^- (1/4) was anticipated to be extractable in DMF-d7 from $NaHS$ powder. This was confirmed experimentally by the observation of a sharp singlet peak at –3.80 ppm NMR peak as shown in Figure 17. H_2S bubbled into D_2O showed a singlet peak at 1.96 ppm. This was confirmed by adding increasing amounts of HCl to 0.1 M $NaHS$ in D_2O that resulted in the 1.96 ppm peak (Figure 18) increasing with decreasing pH. Concomitantly, the –2.17 ppm peak decreased confirming its

identity as HS^-. DMF and D_2O are miscible in all portions. H_2S in DMF-d7 and H_2S in D_2O added to DMF-d7 showed singlet peaks only slightly shifted relative to D_2O, being at 1.77 ppm (Figure 19) and 1.76 ppm (Figure 20), respectively. Thus, H_2S was not the source of the -3.80 ppm peak.

The effect of increasing pH and concentration of $NaHS$ on the HS^- peak at –2.2 ppm was determined. A 0.1 M solution of $NaHS$ dissolved in D_2O had a pH of 9.0 and showed the H_2S peak at 1.95 ppm and the HS^- peak at –2.22 ppm. The latter peak was confirmed by increasing the concentration and pH of a mixture of $NaOH$ and H_2S to form HS^- that resulted in an increasing intensity of the –2.22 ppm peak. For example, an intense HS^- peak was observed at –2.08 ppm in the NMR spectrum of H_2S bubbled into a 0.25 M solution of $NaOH$ dissolved in D_2O until the pH was 9.0 (Figure 21).

As discussed *supra*, the hydrino hydride H^- (1/4) peak at –3.84 ppm in DMF-d7 (Figure 14) was previously found to react with water (Figure 16) and was absent from the spectrum of $NaHS$ dissolved in D_2O (Figure 18). To provide a control for HS^- in DMF-d7 as the NMR solvent, $NaHS$ was synthesized under conditions that were unfavorable to the NaH catalysis reaction with S as a getter. Specifically, H_2S was bubbled into a concentrated D_2O solution of $NaOH$ until the pH matched that of 0.1 M $NaHS$, pH = 9. As discussed *supra*, the NMR of this D_2O-solvent solution showed a peak at –2.08 ppm (Figure 21) confirming the presence of HS^- and the successful synthesis of $NaHS$. When the prepared hydrino-free $NaHS$ was added to DMF-d7 a broad HS^- peak was observed at –2.73 ppm (Figure 22), that was similar to the HS^- peak in D_2O. Increasing the pH to greater than 11 resulted in a broad peak in the region –1.5 ppm to –3 ppm.

Then, a saturated solution of $NaHS$ in D_2O was added to DMF-d7 with the result that a very broad peak at –3 ppm was formed (Figure 23). Since hydrino hydride reacts with water, this peak and the other very broad peaks in the region between about –2 and –3 ppm from H_2S + $NaOH$ that became more upfield shifted and broadened with increasing concentration or pH were assigned to HS_n^-. Sulfur also forms stable sulfanes in aqueous solution and other solvents having the structure H_2S_n, typically n=1 through 8 [63]. The corresponding ionized species HS_n^- are expected to have an increasing upfield shifted and broadened NMR peak as the chain-length increases with pH and concentration.

With the addition of water beyond trace, the hydrino hydride ion reacted with water as discussed *supra*. The predicted product is the corresponding molecular hydrino H_2 (1/4). Confirmation of the –3.8 ppm (Figures 14 and 17) peak as H^- (1/4) and its water reactivity was the observation that the H_2 (1/4) peak at 1.27 ppm formed with the disappearance of the –3.8 ppm peak upon the addition of substantial water to a high concentration of $NaHS$ (Figure 23). Using Eq. (19) and the experimental absolute resonance shift of TMS, –31.5 ppm, the predicted gas-phase shift of H_2 (1/4) is

$$\frac{\Delta B_T}{B} = -30.6\, ppm - (-31.5\, ppm) = 0.9\, ppm \tag{47}$$

which is very close to the observed shift of 1.27 ppm (Figure 23). Furthermore, the experimental absolute H_2 gas-phase resonance shift of –28.0 ppm is in excellent agreement with the predicted absolute gas-phase shift of -28.01 ppm (Eq. (19)) as given in Sec. IA.

These solution-phase results not only provide possibility of an unequivocal identification of H^- (1/4) and H_2 (1/4), but their characteristics of having the absence of any solid matrix effect or the possibility of alternative assignments such as U-centered H or F centers in solid matrix confirm the prior solid NMR assignments as well [14]. The upfield-shifted peaks assigned to hydrino hydride ions were also previously identified in solid samples of alkali halido hydrides $MH*X$ wherein M is an alkali metal, $H*$ is hydrino hydride ion, and X is halide. Typically these compounds comprised the favored state of hydrino H^- (1/4) with the molecular hydrino peak H_2 (1/4), but one product of a reaction using NaH as the catalyst with a solid source of hydrogen comprised both the direct catalysis product H^- (1/3) as well as H^- (1/4) observed by the MAS ^1H NMR at –3.15 ppm and –3.97 ppm, respectively [14]. The corresponding H_2 (1/3) and H_2 (1/4) were observed at 1.15 ppm and 1.7 ppm, respectively. This result sustained the assignment of at least one of the hydrino hydride peaks since HS^- could not be both peaks. Since the ^1H NMR of $KH*I$ and $KH*Cl$ dissolved in DMF-d7 showed isolated H_2 (1/4) and H^- (1/4) at 1.2 ppm and –3.86 ppm, respectively, that matched the results from solid fuel reactants, sulfur element analysis was performed on these compounds in addition to metals determination performed previously [14]. The results were in the few parts per million range, far too low to account for the intensity of the NMR peaks. The S-H stretching band is at about 2540 cm^{-1} as confirmed by FTIR of $NaSH$, and its absence in $KH*I$ and $KH*Cl$ confirmed the absence of HS^- or HS_n^-.

The solid and solution NMR identification of H^- (1/4) over HS^- was made unequivocally by the observation of both the H^- (1/4) peak at –3.81 ppm and the HS^- peak at -2.21 ppm (Figure 24) from the DMF-d7 extracted reaction product of 1.32g $LiH(s)$ + 3g Al powder + 12g AC + 3.9g S formed in the chemical cell (Figure 3). Here, the possibility of the product $LiAlH_4$ as source of either of the peaks was eliminated by the observation that $LiAlH_4$ has no upfield peaks consistent with prior observations that alkali hydrides have down-field shifted peaks [29-31].

It was observed previously that $KH*I$ had a substantial matrix shift relative to $KH*Cl$. Both comprised H^- (1/4) as demonstrated by the equivalent solution NMR results of about –3.8 ppm. However, the solid NMR results were quite different in that the H^- (1/4) peak in $KH*I$ was a broad peak at –2.31 ppm; whereas, that of $KH*Cl$ was a very sharp peak at –4.46 ppm [14]. It was also observed previously that the H^- (1/4) peak from $KH*I$ dissolved in DMF-d7 at high concentration was shifted down-field by about 0.2 ppm due to the high ionic strength [14]. This slight solvent-environment effect on the H^- (1/4) peak was also observed when KI was dissolved into the solution of $NaHS$ in DMF-d7.

A significant solvent effect was observed only with some of the extracted-product samples having sulfur as the oxidant. Similar to the –3.81 ppm peak shown in Figure 24 involving S as the oxidant, the DMF-d7 extracted reaction products of 0.33g $LiH(s)$ + 1g Al powder + 4g AC + 1.3g S and 1.66g $KH(s)$ + 1g Al powder + 4g AC + 1.3g S both showed the typical sharp singlet peak at –3.81 ppm (Figure 25) and –3.86 ppm (Figure 26), respectively.

However, the DMF-d7 extracted reaction products of 1g $NaH(s)$ + 1g MgH_2 powder + 4g AC + 3.2g S showed slightly broadened singlet peaks at –3.34 ppm (Figure 27). Sulfur dissolves in nonpolar solvents as eight member rings S_8. When aqueous sulfide solutions are heated with sulfur, solutions containing S_3^{2-} and S_4^{2-} are obtained. When these polysulfide ions are dissolved in polar solvents such as DMF, deep blue solutions are formed. This solution that gave the –3.34 ppm peak was blue indicating the presence of dissolved sulfur species. To test the effect of a solvent shift due to dissolved sulfur, 5 mg of sulfur was added to DMF-d7 extracted $NaHS$, and the H^- (1/4) peak shifted from –3.80 ppm (Figure 17) to –3.37 ppm (Figure 28). This effect was repeatable and reproduced the results of prior results on peaks down-field of –3.8 ppm when sulfur was present in the reaction product.

The ^1H solution NMR was recorded following DMF-d7 solvent extraction of the products of the heterogeneous catalyst systems given in Sec. IIA. and are shown in Figures 29-36 with the H_2 (1/4) peak identified at about 1.21 ppm and H^- (1/4) peak at about –3.85 ppm. Many of these systems are absent a source of sulfur and comprise gaseous oxidants. Thus, they provide further confirmation of the H_2 (1/4) and H^- (1/4) assignments.

C. ToF-SIMS Spectra. The negative $NaHS$ ToF-SIMS spectrum ($m/e = 20 - 30$ and $m/e = 50 - 100$) is shown in Figures 37 and 38, respectively. The hydrino-hydride-compound series NaH_x^- was observed as shown previously [14] wherein the mass deficit from the high resolution (10,000) mass determination and lack of ^{13}C and ^{15}N peaks definitively distinguished this assignment over the $C_2H_x^-$ series observed in controls having hydrocarbons as well as CN^-. The mass differential and absence of magnesium isotope peaks also eliminated MgH_x^-. The series was absent in the further controls, NaH and MgH_2.

In the higher mass region, other series of hydrino hydride ion clusters such as NaH_xS^-, $H_xS_2^-$, and $Na_2H_2S^-$ were observed. The spectrum also showed a very large H^- peak. The corresponding dominant ions in the positive spectrum were Na^+ and S^+.

These peaks were not present in $NaHS$ prepared by combination of NaH and S when S was at a low concentration that avoided an insitu reaction with ion-beam heating. The negative ToF-SIMS spectrum ($m/e = 0 - 20$) of NaH + 5wt% S is shown in Figure 39. Sodium hydrino hydride ions NaH_x^- $x = 1, 2, 3$ were not observed; albeit, S^- was a dominant negative ion (Figure 40) and Na^+ was the dominant positive ion in the positive spectrum. Only background hydrocarbon fragments were observed in this region. The higher-mass clusters having S were not observed as well.

D. XPS Identification of H^- (1/4). A survey spectrum was obtained on $NaHS$ over the region $E_b = 0 \, eV$ to 1200 eV (Figure 41). The primary element peaks allowed for the determination of all of the elements present in the $NaHS$ crystals. No elements were present in the survey scan which could be assigned to peaks in the low binding energy region (Figure 42) with the exception of the Na $2p$ peak at 29.9 eV, F $2S$ 27.7 eV due to background fluorocarbon, the O $2s$ at 23 eV, the negligible S $3s$ at 18 eV, and the S $3p$ at 7.5 eV. The peaks assigned to H^-

(1/4) were not due to sulfur since noncatalyst controls such as CuS showed no peaks in the corresponding region. Accordingly, any other peaks in this region must be due to novel species. As shown in Figure 42, the XPS spectrum of $NaHS$ differs from the known peaks due to the identified primary elements having additional peaks at 9.5 eV and 12.7 eV but do match the $H^-(1/4)$ $E_b = 11.2$ eV hydride ion (Eq. (10)). The literature was searched for elements having a peak in the valence-band region that could be assigned to these peaks. Given the primary element peaks present, there was no known alternative assignment. Thus, the 9.5 eV and 12.7 eV peaks that could not be assigned to known elements and do not correspond to any other primary element peak were assigned to the $H^-(1/4)$ in two different chemical environments. These features closely matched those for $H^-(1/4)$ of $KH*I$ reported previously [14-17, 27, 31]. The presence of $H^-(1/4)$ in two different chemical environments is further evidenced by the ^1H MAS NMR spectrum such as that of $KH*Cl$ shown in Figure 49 compared to Figure 35A of Ref. [14].

E. Applications

Hydride ions with increased binding energies form novel compounds with the potential for future applications in many industries including chemical, electronics, computer, military, energy, and aerospace in the form of products such as battery materials, propellants, solid fuels, surface coatings, structural materials, and chemical processes. The binding energies given by Eq. (10) go through a maximum stability at $p = 16$ and decrease in stability such that $p = 24$ corresponds to the last stable ion of the series. Applications are anticipated based on this range of stability. Significant applications also exist for the corresponding molecular species H_2 (1/p).

i. High Voltage Battery. Hydride ions having extraordinary binding energies may stabilize a cation M^{x+} in an extraordinarily high oxidation state such as +2 in the case of lithium. Thus, these hydride ions may be used as the basis of a high voltage battery of a rocking-chair design wherein the hydride ion moves back and forth between the cathode and anode half cells during discharge and charge cycles. Exemplary reactions for a cation M^{x+} are:

Cathode reaction:
$$MH_x + e^- \rightarrow MH_{x-1} + H^- \tag{48}$$

Anode reaction:
$$MH_{x-2} + H^- \rightarrow MH_{x-1} + e^- \tag{49}$$
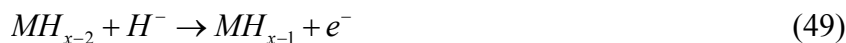
Overall reaction:
$$MH_x + MH_{x-2} \rightarrow 2MH_{x-1} \tag{50}$$

ii. Energetic Propellant. The reaction to form H_2 (1/p) from a hydride compound $M^+H^-(1/p)$ containing $H^-(1/p)$, where M^+ is a metal ion such as Li^+ and $p \approx 24$, represents a potentially very energetic reaction. In the application of $M^+H^-(1/p)$ as a solid, liquid, or gaseous rocket fuel, rocket propellant power may be provided by reaction of $M^+H^-(1/p)$ with a proton to form

H_2 (1/4) or by the thermal decomposition of $M^+H^-(1/p)$ to form H_2 (1/p). The total energy of H_2 (1/p) and H^- (1/p) are given by Eqs. (14) and the sum of Eqs. (10) and (1) with (3), respectively. Using $32p^2\ eV$ as an estimate of the total energy of H_2 (1/p) and the total energy of H (1/p) given by Eqs. (1) and (3) as an estimate of total energy of H^- (1/p), the energy balance of the proton reaction is

$$M^+H^-(1/p) + H^+X^- \rightarrow H_2(1/p) + MX + p^2(32 - 13.6)\ eV \qquad (51)$$

The energy of the decomposition reaction is

$$2M^+H^-(1/p) \xrightarrow{\Delta} H_2(1/p) + 2M + p^2(32 - 2\cdot 13.6)\ eV \qquad (52)$$

Very high energy balances are possible as p approaches the limit for a stable hydride ion at 24.

In the case of H^- (1/24), the energy balances for Eqs. (51) and (52) are truly unconventional, 10 keV and 2.7 keV, respectively, compared to combustion that releases 1.48 eV per hydrogen atom. Thus, energies of about 7000 and 2000 times that of the conventional hydrogen-oxygen reaction, respectively, are expected and the mass of reactants may be compared to these of hydrogen. Thus, a H^- (1/24)-based propellant may be transformational especially given the logarithmic dependence on fuel-weight to lift in the rocketry equation [64].

iii. UV Laser. The existence of excited vibration-rotational levels of H_2 (1/p) in the gas phase and emission of these molecules trapped in a crystalline lattice [14] presents the possibility of a laser using a transition from a vibration-rotational level to another lower-energy-level other than one with a significant Boltzmann population at the cell neutral-gas temperature (e.g. one with both υ and $J = 0$). A laser may be realized using cavities and mirrors that are appropriate for the desired wavelength similar to those of current lasers based on molecular vibration-rotational levels such as the CO_2 laser. However, an advantage exists to produce laser light at much shorter wavelengths. The current results anticipate a laser based on vibration-rotational levels of H_2 (1/4) that lases in the UV. Such lasers have significant application in photolithography.

Lithography, the technique for manufacturing microelectronics semiconductor devices such as processors and memory chips, presently uses deep UV radiation at 193 nm from the ArF excimer laser. Future sources are F_2 lasers at 157 nm and perhaps H_2 lasers at 127 nm. Advancements in light sources are required in order to achieve the steady reduction in the size of integrated circuits. Only a free electron laser (FEL) with a minimum beam energy of 500 MeV appears suitable as a light source for the Next Generation Lithography (NGL) based on EUV lithography (13.5 nm) [65-66]. With the discovery of H_2 (1/p), the opportunity may exist to replace a FEL that occupies the size of a large building with a table-top laser for the desired 10 to 14 nm range based on vibration-rotational-state inversion of H_2 (1/13).

III. Conclusion

The predictions for transitions of atomic hydrogen to form hydrinos such as power production, characteristic signatures of hydrino compound reaction products, pumped catalyst states, fast H, characteristic continuum radiation directly showing hydrino-state transitions below the misnamed "ground state" with the production of liquid-helium-condensable molecular hydrino gas have been confirmed experimentally [13-14]. The first attempt to produce a commercial power process from this reaction was successful in exceeding the criterion for energy balance, power density, and operating temperature, but the $NaOH$-doped R-Ni fuel reprocessing may be more technically challenging. In this study, we advanced the potential of

23

the hydrino power source to replace conventional sources based on superior cost, supply, and environmental considerations. Specifically, we developed a heterogeneous catalyst system as a means to circumvent the difficult fuel regeneration problem following cessation of the NaH catalysis reaction in the $NaOH$-doped R-Ni solid fuel due to undesirable side reactions of forming a sodium aluminate or alumina surface layer. Considering the reactive components requiring regeneration, the excess power and energy balances measured by water-flow calorimetry were about five to 25 times more energetic per mole than that of the $NaOH$-doped R-Ni fuel.

The energy and power scaled linearly, to easily achieve over 30 kW. Based on the volume of the catalyst and hydrogen fuel consumed to form H_2 (1/4) with an energy release of >50 MJ/mole H_2 compared to $\Delta H_f (H_2O \text{ liquid}) = -285.8 \ kJ/mole$, the power density is comparable to that of gas-fired power plants, the energy balance is greater than that of any known material on a weight or molar basis, and the temperature can be run to the limit set by the material tolerances of the reaction vessel. The scaled-up power results directly demonstrate a new field of hydrogen chemistry and a powerful new energy source that has the capability of being scaled to any level based on the quantity of reactants used with performance levels projecting superiority over other energy sources such as fossil-fuel and nuclear energy sources [14]. Furthermore, the process is nonpolluting. Since the identified H_2 (1/p) byproduct is stable and lighter-than-air, it cannot accumulate in the Earth's atmosphere. And, it is present in the environment such as in common ingested salts as reported previously [14]. Thus, the typical $500,000,000/plant-yr fossil fuel cost and the environmental impact to the air, water, and ground of producing, handling, and using fossil fuels may be eliminated. Similarly, the radioactive waste from nuclear plants, their tremendous infrastructure costs, and security and accident risks may also be avoided.

Having met or exceeded existing performance characteristics, the final criterion for commercial competitiveness is the existence of cost effective regeneration chemistry. The hydrino reaction requires (i) a catalyst and a source of hydrogen that were both provided by LiH, KH, or NaH, (ii) a dispersive and electron accepting and conducting support material that was provided by activated carbon, TiC or YC$_2$, and (iii) oxidation-reduction reactants. The reactant catalyst, oxidant and reductant can readily be regenerated from the product halides such as NaCl by electrolysis of a eutectic melt with the oxidant metal as the anode to directly form the corresponding halide and lower the regenerative energy gap. Based on a 45% thermal-electric conversion efficiency and a 85% electrolysis efficiency for the conversion of the catalyst metal halide to oxidant metal halide at the anode, the energy gain required for regeneration is a factor of about 2.6 times the standard enthalpies from these reactions. The energy gains of the hydrino reactions were comparable to this nominal milestone for regeneration.

In the case that the reactant-product energy gap is small, the reactants may be regenerated thermally. For example, it is thermodynamically favorable to thermally reverse the reaction given by Eq. (44) by several pathways to achieve the following:

$$2KBr + Eu \rightarrow EuBr_2 + 2K \tag{53}$$

The reaction can be driven to completion by dynamically removing potassium. The reaction given by Eq. (53) was confirmed by reacting about a two-to-one molar mixture of KBr and Eu (4.1g (34.5 mmoles) of KBr and 2.1g (13.8 mmoles) of Eu) wrapped in a stainless steel foil crucible in a 0.75 inch OD stainless steel tube open at one end in a 1 inch OD vacuum-tight quartz tube. The reaction was run at 850 °C for one hour under vacuum. Potassium metal was

evaporated from the hot zone, and the majority product identified by XRD was $EuBr_2$. The energy balance from non-hydrino chemistry of this hydrino catalyst system is essentially energy neutral such that with each power and regeneration cycle maintained concurrently to constitute a continuous power source, 900 $kJ/mole$ $EuBr_2$ are released per cycle.

Thus, the reactants can be regenerated from the products by either eutectic-melt electrolysis or thermally using components of commercial chemical-plant systems. With standard systems, commercial levels of power can be generated at typical power-plant operating temperatures and at higher power densities. We envision green power plants operated continuously as power and regeneration reactions of the fuel mixture are maintained in synchrony using known industrial processes involving electrolysis or thermally-driven metal exchange of the halide-salt products. Only the hydrogen fuel obtained ultimately from the water is consumed with an enormous 200-fold energy release relative to combustion.

Rather than pollutants the byproducts have significant advanced technology applications based on their stability characteristics. In prior studies [14], novel alkali halido hydrino hydride compounds ($MH * X$; $M = K, Li, or Na$, $X = halide$) were synthesized in kiln cells operated over 72 hours at elevated temperature >500 °C. The ^1H MAS NMR showed a distinct peak at ~ 1 ppm and upfield shift peaks corresponding to H_2 (1/4) and H^- (1/3) and H^- (1/4) in the corresponding solid matrix, respectively. ^1H NMR of $MH * X$ dissolved in DMF-d7 showed isolated H_2 (1/4) and H^- (1/4) at 1.2 ppm and −3.86 ppm, respectively, wherein the absence of any solid matrix effect or the possibility of alternative assignments confirmed the solid NMR assignments. The metal-halide-oxidant system as well as additional regeneration-capable heterogeneous catalyst systems were applied to the production of compounds comprising hydrino species as well as heat. A typical energy gain due to hydrino formation of 1.5 times the theoretical conventional-chemistry maximum was achieved corresponding to a 1000 kJ/mole oxidant at a power density of 10 W/cm^3. The H_2 (1/4) and H^- (1/4) hydrino products of these reactions were observed at 1.2 ppm and at −3.86 ppm, respectively, by ^1H solution NMR on DMF-d7 extracted reaction products (Sec. IIIB). ToF-SIMs showed hydrino hydride peaks (Sec. IIIC). XPS showed H^- (1/4) hydrino hydride ion peaks (Sec. IIID). Thus, similar results of hydrino-species production in the form of solid compounds and their isolation as free species in solution have been achieved with reactions having a duration of under 30 seconds at reaction rates of about a factor 500,000 times faster than the rates of prior systems [14, 29-31].

Regarding a combined power and chemical plant, rather than pollutants the byproducts have significant advanced technology applications based on their stability characteristics. Advanced hydride technologies are indicated. Hydride ions H^- (1/p) having extraordinary binding energies may stabilize a cation M^{x+} in an extraordinarily high oxidation state as the basis of a high voltage battery. And, a rocketry propellant based on H^- (1/24) to H_2 (1/24) may be possible with an energy release so large that it may be transformational. Significant applications also exist for the corresponding molecular species H_2 (1/p) wherein the excited vibration-rotational levels could be the basis of a UV laser that could significantly advance photolithography and line-of-sight telecommunications.

References

1. R. Mills, *The Grand Unified Theory of Classical Physics*; June 2008 Edition, posted at http://www.blacklightpower.com/theory/bookdownload.shtml.

2. R. L. Mills, B. Holverstott, B. Good, N. Hogle, A. Makwana, "Total Bond Energies of Exact Classical Solutions of Molecules Generated by Millsian 1.0 Compared to Those Computed Using Modern 3-21G and 6-31G* Basis Sets," Physics Essays, 23, (2010), 153.

3. R. L. Mills, "Classical Quantum Mechanics," Physics Essays, Vol. 16, No. 4, December, (2003), pp. 433-498.

4. R. Mills, "Physical Solutions of the Nature of the Atom, Photon, and Their Interactions to Form Excited and Predicted Hydrino States," Physics Essays, Vol. 20, No. 3, (2007), pp. 403-460.

5. R. L. Mills, "Exact Classical Quantum Mechanical Solutions for One- Through Twenty-Electron Atoms," Physics Essays, Vol. 18, (2005), pp. 321-361.

6. R. L. Mills, "The Nature of the Chemical Bond Revisited and an Alternative Maxwellian Approach," Physics Essays, Vol. 17, (2004), pp. 342-389.

7. R. L. Mills, "Maxwell's Equations and QED: Which is Fact and Which is Fiction," Physics Essays, Vol. 19, (2006), pp. 225-262.

8. R. L. Mills, "Exact Classical Quantum Mechanical Solution for Atomic Helium Which Predicts Conjugate Parameters from a Unique Solution for the First Time," Physics Essays, Vol. 21(20), (2008), pp. 103-141.

9. R. L. Mills, "The Fallacy of Feynman's Argument on the Stability of the Hydrogen Atom According to Quantum Mechanics," Annales de la Fondation Louis de Broglie, Vol. 30, No. 2, (2005), pp. 129-151.

10. R. Mills, "The Grand Unified Theory of Classical Quantum Mechanics," Int. J. Hydrogen Energy, Vol. 27, No. 5, (2002), pp. 565-590.

11. R. Mills, The Nature of Free Electrons in Superfluid Helium—a Test of Quantum Mechanics and a Basis to Review its Foundations and Make a Comparison to Classical Theory, Int. J. Hydrogen Energy, Vol. 26, No. 10, (2001), pp. 1059-1096.

12. R. Mills, "The Hydrogen Atom Revisited," Int. J. of Hydrogen Energy, Vol. 25, Issue 12, December, (2000), pp. 1171-1183.

13. R. L. Mills, Y. Lu, K. Akhar, "Spectroscopic Observation of Helium-Ion- and Hydrogen-Catalyzed Hydrino Transitions," Cent. Eur. J. Phys., (2009), doi: 10.2478/s11534-009-0106-9

14. R. L. Mills, G. Zhao, K. Akhtar, Z. Chang, J. He, Y. Lu, W. Good, G. Chu, B. Dhandapani, "Commercializable Power Source from Forming New States of Hydrogen," Int. J. Hydrogen Energy, Vol. 34, (2009), 573-614.

15. R. L. Mills, J. He, Y. Lu, M. Nansteel, Z. Chang, B. Dhandapani, "Comprehensive Identification and Potential Applications of New States of Hydrogen," Int. J. Hydrogen Energy, Vol. 32(14), (2007), pp. 2988-3009.

16. R. Mills, J. He, Z. Chang, W. Good, Y. Lu, B. Dhandapani, "Catalysis of Atomic Hydrogen to Novel Hydrogen Species H^- (1/4) and H_2 (1/4) as a New Power Source," Int. J. Hydrogen Energy, Vol. 32, No. 12, (2007), pp. 2573-2584.

17. R. Mills, P. Ray, B. Dhandapani, W. Good, P. Jansson, M. Nansteel, J. He, A. Voigt, "Spectroscopic and NMR Identification of Novel Hydride Ions in Fractional Quantum Energy States Formed by an Exothermic Reaction of Atomic Hydrogen with Certain Catalysts," European Physical Journal-Applied Physics, Vol. 28, (2004), pp. 83-104.

18. K. Akhtar, J. Scharer, R. L. Mills, "Substantial Doppler broadening of atomic-hydrogen lines in DC and capacitively coupled RF plasmas," J. Phys. D, Applied Physics, Vol. 42, (2009), 135207(.

19. R. Mills, K. Akhtar, "Tests of Features of Field-Acceleration Models for the Extraordinary Selective H Balmer α Broadening in Certain Hydrogen Mixed Plasmas," Int. J. Hydrogen Energy, Vol. 34, (2009), pp. 6465-6477.

20. R. L. Mills, P. Ray, B. Dhandapani, R. M. Mayo, J. He, "Comparison of Excessive Balmer α Line Broadening of Glow Discharge and Microwave Hydrogen Plasmas with Certain Catalysts," J. of Applied Physics, Vol. 92, No. 12, (2002), pp. 7008-7022.

21. R. L. Mills, P. Ray, B. Dhandapani, J. He, "Comparison of Excessive Balmer α Line Broadening of Inductively and Capacitively Coupled RF, Microwave, and Glow Discharge Hydrogen Plasmas with Certain Catalysts," IEEE Transactions on Plasma Science, Vol. 31, No. (2003), pp. 338-355.

22. R. L. Mills, P. Ray, "Substantial Changes in the Characteristics of a Microwave Plasma Due to Combining Argon and Hydrogen," New Journal of Physics, www.njp.org, Vol. 4, (2002), pp. 22.1-22.17.

23. R. L. Mills, B. Dhandapani, K. Akhtar, "Excessive Balmer α Line Broadening of Water-Vapor Capacitively-Coupled RF Discharge Plasmas," Int. J. Hydrogen Energy, Vol. 33, (2008), pp. 802-815.

24. R. Mills, P. Ray, B. Dhandapani, "Evidence of an Energy Transfer Reaction Between Atomic Hydrogen and Argon II or Helium II as the Source of Excessively Hot H Atoms in RF Plasmas," Journal of Plasma Physics, (2006), Vol. 72, Issue 4, pp. 469-484.24.

25. J. Phillips, C-K Chen, K. Akhtar, B. Dhandapani, R. Mills, "Evidence of Catalytic Production of Hot Hydrogen in RF Generated Hydrogen/Argon Plasmas," International Journal of Hydrogen Energy, Vol. 32(14), (2007), pp. 3010-3025.

26. R. L. Mills, P. C. Ray, R. M. Mayo, M. Nansteel, B. Dhandapani, J. Phillips, "Spectroscopic Study of Unique Line Broadening and Inversion in Low Pressure Microwave Generated Water Plasmas," J. Plasma Physics, Vol. 71, Part 6, (2005), pp. 877-888.

27. R. L. Mills, P. Ray, "A Comprehensive Study of Spectra of the Bound-Free Hyperfine Levels of Novel Hydride Ion H^- (1/2), Hydrogen, Nitrogen, and Air," Int. J. Hydrogen Energy, Vol. 28, No. 8, (2003), pp. 825-871.

28. R. Mills, "Spectroscopic Identification of a Novel Catalytic Reaction of Atomic Hydrogen and the Hydride Ion Product," Int. J. Hydrogen Energy, Vol. 26, No. 10, (2001), pp. 1041-1058.

29. R. Mills, B. Dhandapani, M. Nansteel, J. He, T. Shannon, A. Echezuria, "Synthesis and Characterization of Novel Hydride Compounds," Int. J. of Hydrogen Energy, Vol. 26, No. 4, (2001), pp. 339-367.

30. R. Mills, B. Dhandapani, M. Nansteel, J. He, A. Voigt, "Identification of Compounds Containing Novel Hydride Ions by Nuclear Magnetic Resonance Spectroscopy," Int. J. Hydrogen Energy, Vol. 26, No. 9, (2001), pp. 965-979.

31. R. Mills, B. Dhandapani, N. Greenig, J. He, "Synthesis and Characterization of Potassium Iodo Hydride," Int. J. of Hydrogen Energy, Vol. 25, Issue 12, December, (2000), pp. 1185-1203.

32. K. R. Lykke, K. K. Murray, W. C. Lineberger, "Threshold photodetachment of H^-," Phys. Rev. A, Vol. 43, No. 11, (1991), pp. 6104-6107.

33. D. R. Lide, *CRC Handbook of Chemistry and Physics*, 86th Edition, CRC Press, Taylor & Francis, Boca Raton, (2005-6), pp. 10-202 to 10-204.

34. K. K. Baldridge, J. S. Siegel, "Correlation of empirical δ (TMS) and absolute NMR chemical shifts predicted by ab initio computations," J. Phys. Chem. A, Vol. 103, (1999), pp. 4038-4042.

35. J. Mason, Editor, *Multinuclear NMR*, Plenum Press, New York, (1987), Chp. 3.

36. C. Suarez, E. J. Nicholas, M. R. Bowman, "Gas-phase dynamic NMR study of the internal rotation in N-trifluoroacetlypyrrolidine," J. Phys. Chem. A, Vol. 107, (2003), pp. 3024-3029.

37. C. Suarez, "Gas-phase NMR spectroscopy," The Chemical Educator, Vol. 3, No. 2, (1998).

38. H. Beutler, Z. Physical Chem., "Die dissoziationswarme des wasserstoffmolekuls H_2, aus einem neuen ultravioletten resonanzbandenzug bestimmt," Vol. 27B, (1934), pp. 287-302.

39. G. Herzberg, L. L. Howe, "The Lyman bands of molecular hydrogen," Can. J. Phys., Vol. 37, (1959), pp. 636-659.

40. P. W. Atkins, *Physical Chemistry*, Second Edition, W. H. Freeman, San Francisco, (1982), p. 589.

41. R. Mills and M. Nansteel, P. Ray, "Argon-Hydrogen-Strontium Discharge Light Source," IEEE Transactions on Plasma Science, Vol. 30, No. 2, (2002), pp. 639-653.

42. R. Mills and M. Nansteel, P. Ray, "Bright Hydrogen-Light Source due to a Resonant Energy Transfer with Strontium and Argon Ions," New Journal of Physics, Vol. 4, (2002), pp. 70.1-70.28.

43. R. Mills, J. Dong, Y. Lu, "Observation of Extreme Ultraviolet Hydrogen Emission from Incandescently Heated Hydrogen Gas with Certain Catalysts," Int. J. Hydrogen Energy, Vol. 25, (2000), pp. 919-943.

44. R. Mills, M. Nansteel, and P. Ray, "Excessively Bright Hydrogen-Strontium Plasma Light Source Due to Energy Resonance of Strontium with Hydrogen," J. of Plasma Physics, Vol. 69, (2003), pp. 131-158.

45. R. L. Mills, J. He, M. Nansteel, B. Dhandapani, "Catalysis of Atomic Hydrogen to New Hydrides as a New Power Source," International Journal of Global Energy Issues (IJGEI), Special Edition in Energy Systems, Vol. 28, Nos. 2/3 (2007), pp. 304-324.

46. H. Conrads, R. Mills, Th. Wrubel, "Emission in the Deep Vacuum Ultraviolet from a Plasma Formed by Incandescently Heating Hydrogen Gas with Trace Amounts of Potassium Carbonate," Plasma Sources Science and Technology, Vol. 12, (3003), pp. 389-395.

47. J. Phillips, R. L. Mills, X. Chen, "Water Bath Calorimetric Study of Excess Heat in 'Resonance Transfer' Plasmas," Journal of Applied Physics, Vol. 96, No. 6, pp. 3095-3102.

48. R. L. Mills, X. Chen, P. Ray, J. He, B. Dhandapani, "Plasma Power Source Based on a Catalytic Reaction of Atomic Hydrogen Measured by Water Bath Calorimetry," Thermochimica Acta, Vol. 406/1-2, (2003), pp. 35-53.

49. R. L. Mills, P. Ray, "Extreme Ultraviolet Spectroscopy of Helium-Hydrogen Plasma," J. Phys. D, Applied Physics, Vol. 36, (2003), pp. 1535-1542.

50. R. L. Mills, P. Ray, B. Dhandapani, M. Nansteel, X. Chen, J. He, "New Power Source from Fractional Quantum Energy Levels of Atomic Hydrogen that Surpasses Internal Combustion," J Mol. Struct., Vol. 643, No. 1-3, (2002), pp. 43-54.

51. R. Mills, P. Ray, "Spectral Emission of Fractional Quantum Energy Levels of Atomic Hydrogen from a Helium-Hydrogen Plasma and the Implications for Dark Matter," Int. J. Hydrogen Energy, Vol. 27, No. 3, (2002), pp. 301-322.

52. R. Mills, P. Ray, R. M. Mayo, "CW HI Laser Based on a Stationary Inverted Lyman Population Formed from Incandescently Heated Hydrogen Gas with Certain Group I Catalysts," IEEE Transactions on Plasma Science, Vol. 31, No. 2, (2003), pp. 236-247.

53. R. L. Mills, P. Ray, "Stationary Inverted Lyman Population Formed from Incandescently Heated Hydrogen Gas with Certain Catalysts," J. Phys. D, Applied Physics, Vol. 36, (2003), pp. 1504-1509.

54. R. Mills, P. Ray, R. M. Mayo, "The Potential for a Hydrogen Water-Plasma Laser," Applied Physics Letters, Vol. 82, No. 11, (2003), pp. 1679-1681.

55. D. R. Lide, *CRC Handbook of Chemistry and Physics*, 86th Edition, CRC Press, Taylor & Francis, Boca Raton, (2005-6), pp. 9-54 to 9-59.

56. F. A. Cotton, G. Wilkinson, C. A. Murillo, M. Bochmann, *Advanced Inorganic Chemistry*, Sixth Edition, John Wiley & Sons, Inc., New York, (1999), pp. 92-93.

57. D. R. Lide, *CRC Handbook of Chemistry and Physics*, 86th Edition, CRC Press, Taylor & Francis, Boca Raton, (2005-6), pp. 5-4 to 5-18; 9-63.

58. Microsc. Microanal. Microstruct., Vol. 3, 1, (1992).

59. For specifications see PHI Trift II, ToF-SIMS Technical Brochure, (1999), Eden Prairie, MN 55344.

60. D. R. Lide, *CRC Handbook of Chemistry and Physics*, 88th Edition, CRC Press, Taylor & Francis, Boca Raton, (2007-8).

61. J. A. Dean, *Lange's Handbook of Chemistry*, Fifteenth Edition, McGraw-Hill Professional, New York, (1999).

62. O. Knacke, O. Kubascheeski, K. Hesselmann, *Thermochemical Properties of Inorganic Substances*, 2nd Ed., Springer-Verlag Berlin, Heidelberg (1991).

63. F. A. Cotton, G. Wilkinson, C. A. Murillo, M. Bochmann, *Advanced Inorganic Chemistry*, Sixth Edition, John Wiley & Sons, Inc., New York, (1999), pp. 499-506.

64. G. R. Fowles, *Analytical Mechanics*, Third Edition, Holt, Rinehart, and Winston, New York, (1977), pp. 182-184.

65. J. E. Bjorkholm, "EUV lithography—the successor to optical lithography?," Intel Technology Journal, Q3, (1998), pp. 1-8.

66. K. Hesch, E. Pellegrin, R. Rossmanith, R. Steininger, V. Saile, J. Wust, G. Dattoli, A. Doria, G. Gallerano, L. Giannessi, P. Ottaviani, H. Moser, "Extreme ultraviolet (EUV) sources based on synchrotron radiation," Proceedings of the 2001 Particle Accelerator Conference, Chicago, pp. 654-656.

Table 1. The Maxwellian closed-form calculated and experimental parameters of H_2, D_2, H_2^+ and D_2^+.

Parameter	Calculated	Experimental
H_2 Bond Energy	4.478 eV	4.478 eV
D_2 Bond Energy	4.556 eV	4.556 eV
H_2^+ Bond Energy	2.654 eV	2.651 eV
D_2^+ Bond Energy	2.696 eV	2.691 eV
H_2 Total Energy	31.677 eV	31.675 eV
D_2 Total Energy	31.760 eV	31.760 eV
H_2 Ionization Energy	15.425 eV	15.426 eV
D_2 Ionization Energy	15.463 eV	15.466 eV
H_2^+ Ionization Energy	16.253 eV	16.250 eV
D_2^+ Ionization Energy	16.299 eV	16.294 eV
H_2^+ Magnetic Moment	$9.274 \, X \, 10^{-24} \, JT^{-1} \left(\mu_B \right)$	$9.274 \, X \, 10^{-24} \, JT^{-1} \left(\mu_B \right)$
Absolute H_2 Gas-Phase NMR Shift	-28.0 ppm	-28.0 ppm
H_2 Internuclear Distance[a]	0.748 Å $\sqrt{2}a_o$	0.741 Å
D_2 Internuclear Distance[a]	0.748 Å $\sqrt{2}a_o$	0.741 Å
H_2^+ Internuclear Distance	1.058 Å $2a_o$	1.06 Å
D_2^+ Internuclear Distance[a]	1.058 Å $2a_o$	1.0559 Å
H_2 Vibrational Energy	0.517 eV	0.516 eV
D_2 Vibrational Energy	0.371 eV	0.371 eV
H_2 $\omega_e x_e$	120.4 cm^{-1}	121.33 cm^{-1}
D_2 $\omega_e x_e$	60.93 cm^{-1}	61.82 cm^{-1}
H_2^+ Vibrational Energy	0.270 eV	0.271 eV
D_2^+ Vibrational Energy	0.193 eV	0.196 eV
H_2 J=1 to J=0 Rotational Energy[a]	0.0148 eV	0.01509 eV
D_2 J=1 to J=0 Rotational Energy[a]	0.00741 eV	0.00755 eV
H_2^+ J=1 to J=0 Rotational Energy	0.00740 eV	0.00739 eV
D_2^+ J=1 to J=0 Rotational Energy[a]	0.00370 eV	0.003723 eV

[a] Not corrected for the slight reduction in internuclear distance due to $\overline{E}_{osc}$.

Table 2. The experimental net energy, calculated theoretical maximum energy for conventional chemistry [60-62], excess heat from the hydrino reaction, the peak power, and energy gain of heterogeneous hydrino catalyst systems.

Reactants	Experimental Net Energy (kJ)	Calculated Theoretical Maximum[a] (kJ)	Excess Heat[b] (kJ)	Peak Power (kW)	Energy Gain[c]
5.0g $NaH(s)$ + 5.0g Mg + 20.0g AC + 11.0g $NiBr_2$	53	26.25	26.75	1.75	2
8.3g $KH(s)$ + 5.0g Mg + 20.0g TiC + 15.45g MnI_2	49	18.65	30.35	0.8	2.6
8.3g $KH(s)$ + 5.0g Mg + 20.0g AC + 7.2g $AgCl$	40.42	14.52	25.9	0.67	2.78
8.3g $KH(s)$ + 5.0g Mg + 20.0g TiC + 15.6g $EuBr_2$[d]	45	6.85	38.15	0.75	6.6
50.0g $NaH(s)$ + 50.0g Mg + 200.0g AC + 109.5g $NiBr_2$	577	262.5	314.5	30	2.19

[a] Confirmed by XRD.
[b] Difference of experimental net energy and calculated theoretical maximum.
[c] Ratio of the experimental net energy and calculated theoretical maximum.
[d] Similar results were obtained with YC_2 replacing TiC. No oxides were detectable by XRD.

Figure 1. Schematic of the reaction cell and the cross sectional view of the water flow calorimeter used to measure the energy balances of heterogeneous catalyst reactions to form hydrinos. The components were: 1—inlet and outlet thermistors; 2—high-temperature valve; 3—ceramic fiber heater; 4—copper water-coolant coil; 5—reactor; 6—insulation; 7—cell thermocouple, and 8—water flow chamber.
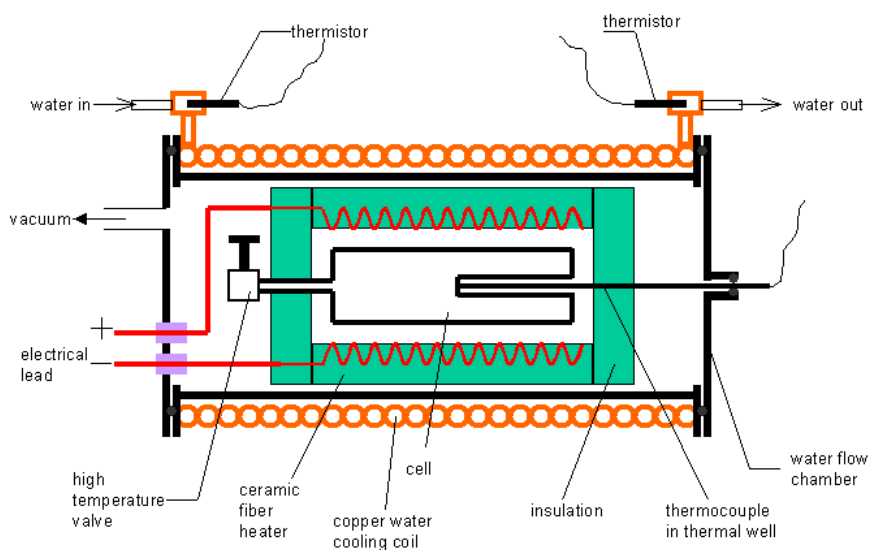
Figure 2. Schematic of the water flow calorimeter used to measure the energy balances of the heterogeneous catalyst reactions to form hydrinos.

Flow Calorimeter System
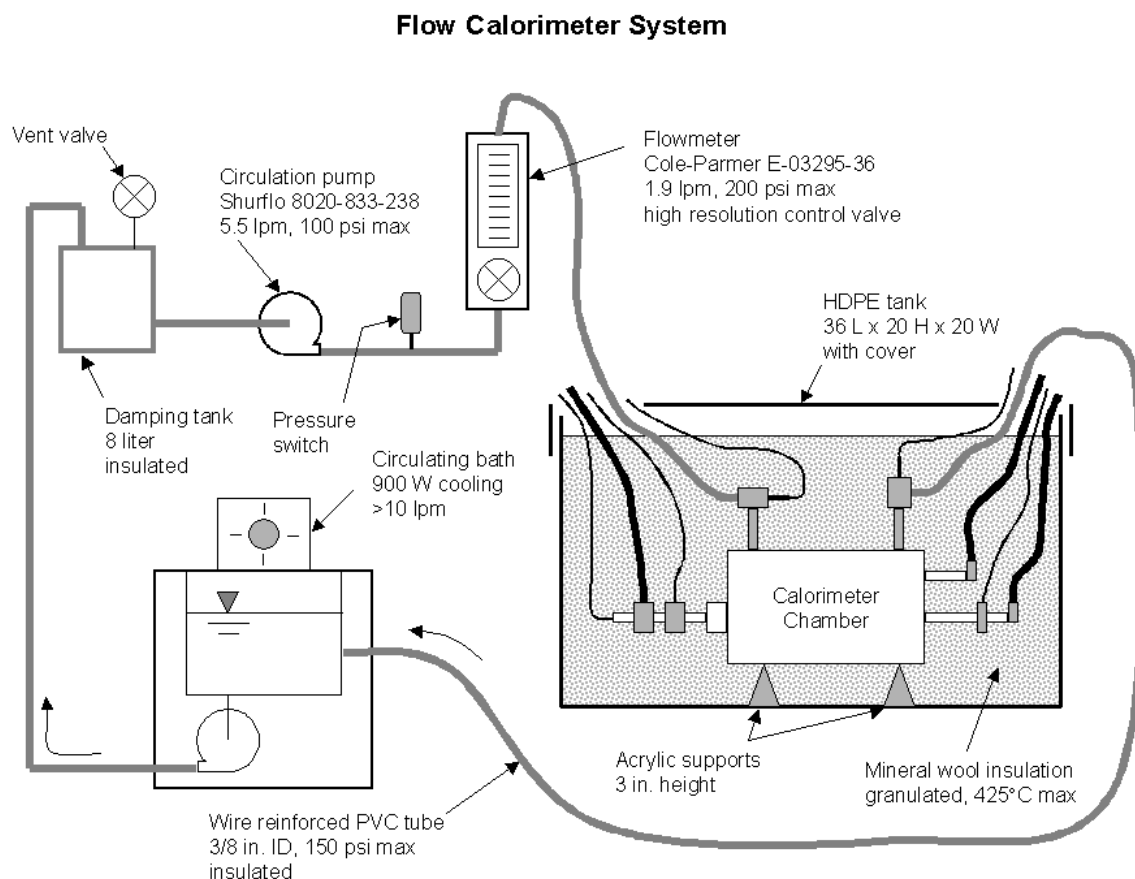
Figure 3. Stainless steel gas cell to synthesize *MH*X* (*M* is the catalyst metal and *X* is a halide). The components were: 101—stainless steel cell; 117—internal cavity of cell; 118—high vacuum conflat flange; 119—mating blank conflat flange; 102—stainless steel tube vacuum line and gas supply line; 103—lid to the kiln or top insulation, 104—surrounding heaters covered by high temperature insulation; 108—R-Ni dissociator when used; 109—reactants; 110—high vacuum turbo pump; 112—pressure gauge; 111—vacuum pump valve; 113—valve; 114—valve; 115—regulator, and 116—hydrogen tank.
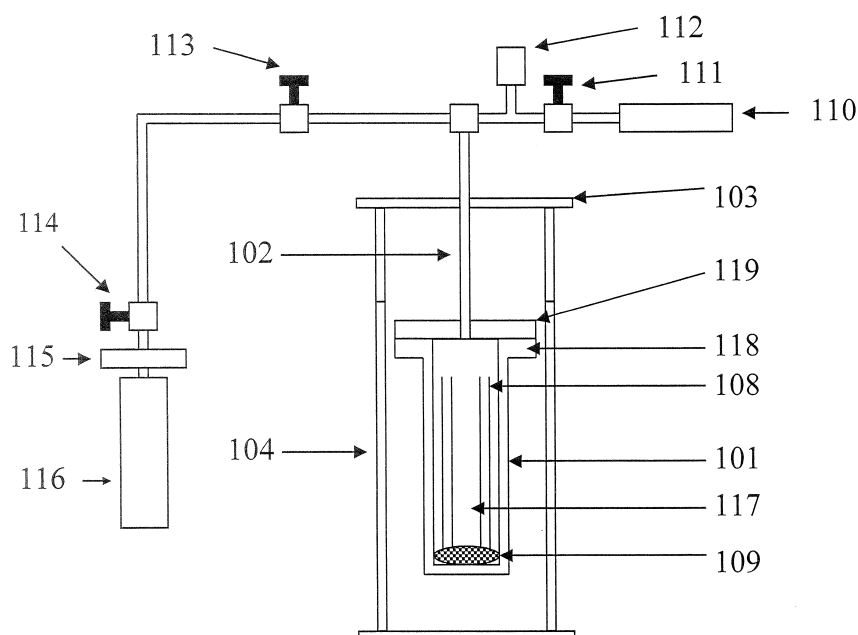
Figure 4. The cell temperature with time due to the indicated constant power for the heterogeneous catalyst mixture, 5.0g $NaH(s)$ + 5.0g Mg + 20.0g AC + 11.0g $NiBr_2$. The reaction liberated 53 kJ of energy in about 30 s to develop a system-response-corrected peak power in excess of 1.75 kW.
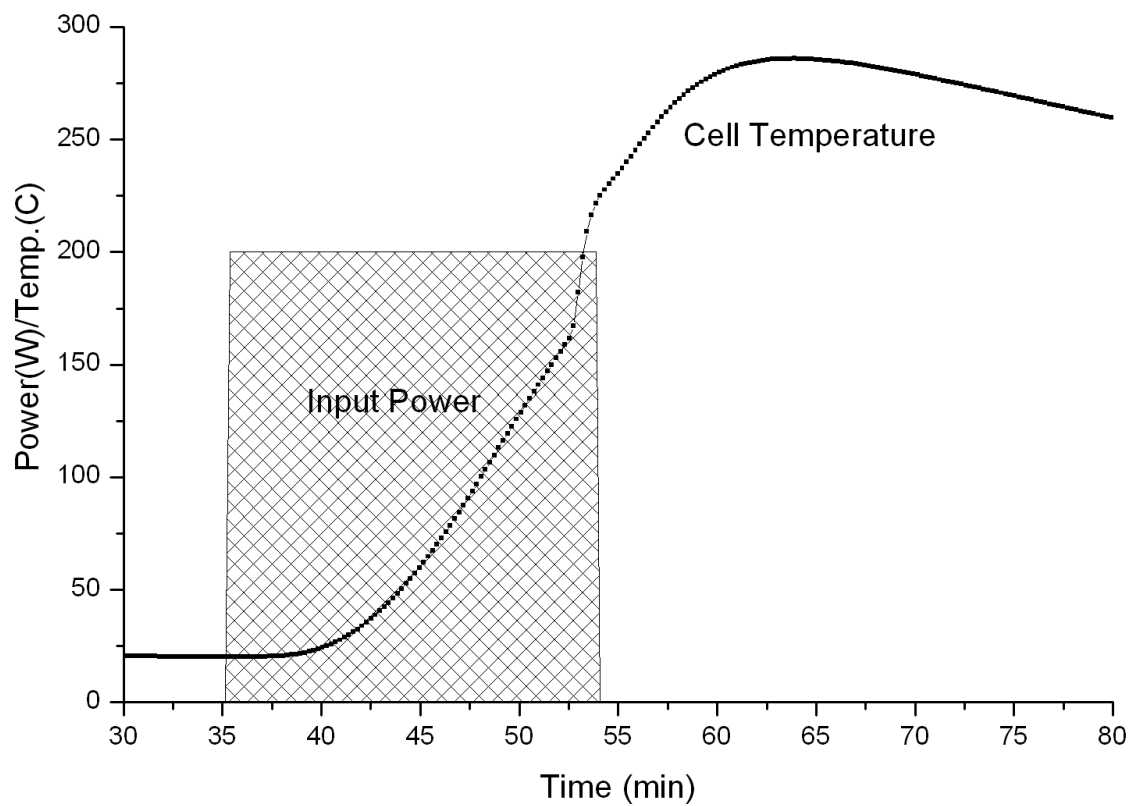
Figure 5. The coolant power with time for the heterogeneous catalyst mixture, 5.0g $NaH(s)$ + 5.0g Mg + 20.0g AC + 11.0g $NiBr_2$. The numerical integration of the input and output power curves with the calibration correction applied yielded the output energy of 277 kJ and an input energy of 224 kJ corresponding to a net energy of 53 kJ.
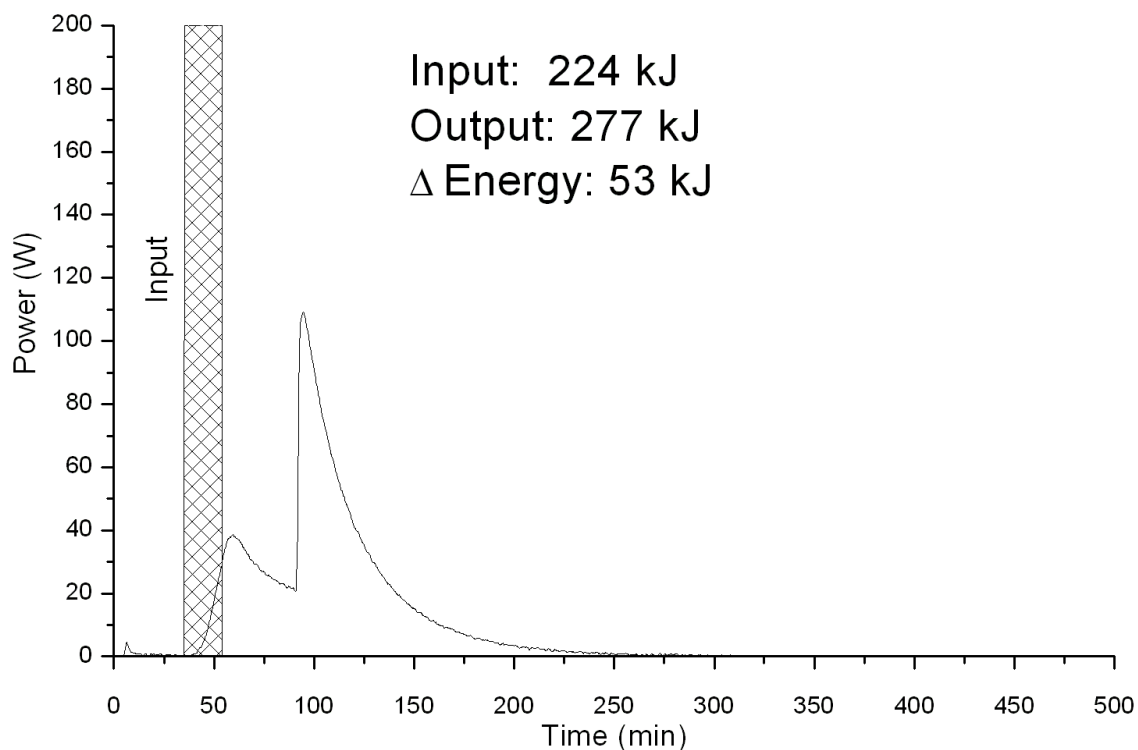
Figure 6. The cell temperature with time due to the indicated constant power for the heterogeneous catalyst mixture, 8.3g $KH(s)$ + 5.0g Mg + 20.0g TiC + 15.45g MnI_2. The reaction liberated 49 kJ of energy in about 60 s to develop a system-response-corrected peak power in excess of 0.8 kW.
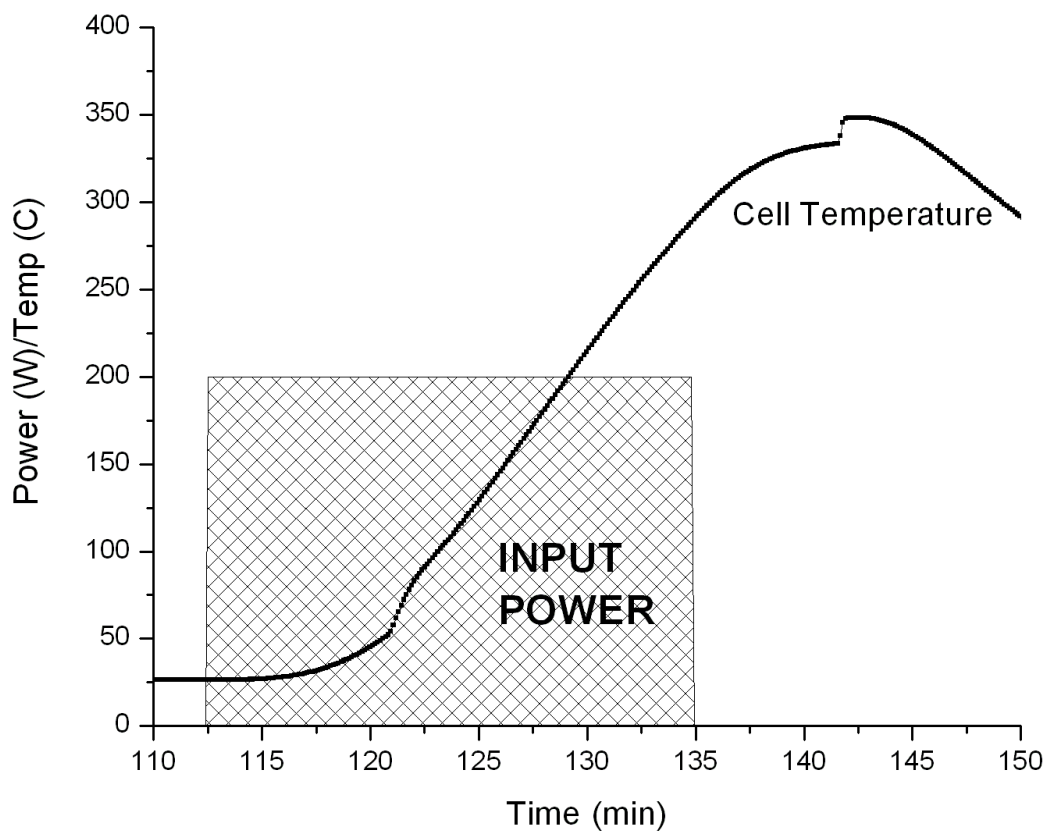
Figure 7. The coolant power with time for the heterogeneous catalyst mixture, 8.3g $KH(s)$ + 5.0g Mg + 20.0g TiC + 15.45g MnI_2. The numerical integration of the input and output power curves with the calibration correction applied yielded the output energy of 318 kJ and an input energy of 269 kJ corresponding to a net energy of 49 kJ.
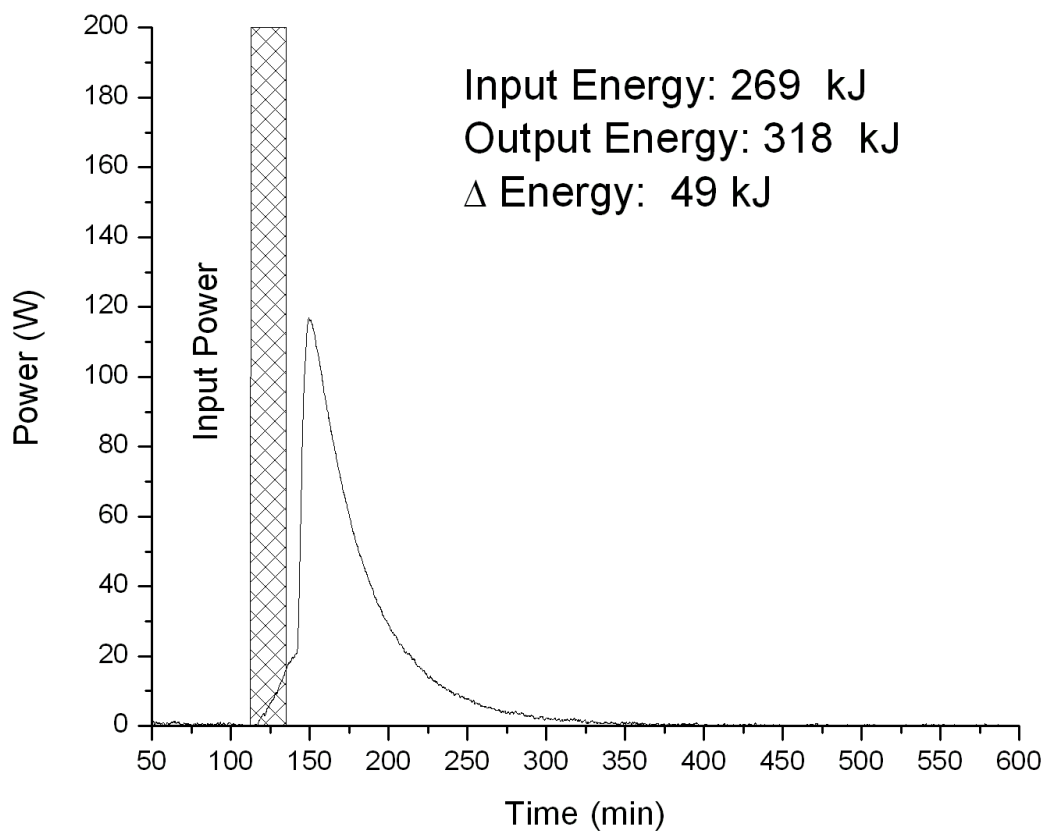
Figure 8. The cell temperature with time due to the indicated constant power for the heterogeneous catalyst mixture, 8.3g $KH(s)$ + 5.0g Mg + 20.0g AC + 7.2g $AgCl$. The reaction liberated 40.42 kJ of energy in about 60 s to develop a system-response-corrected peak power in excess of 0.67 kW.
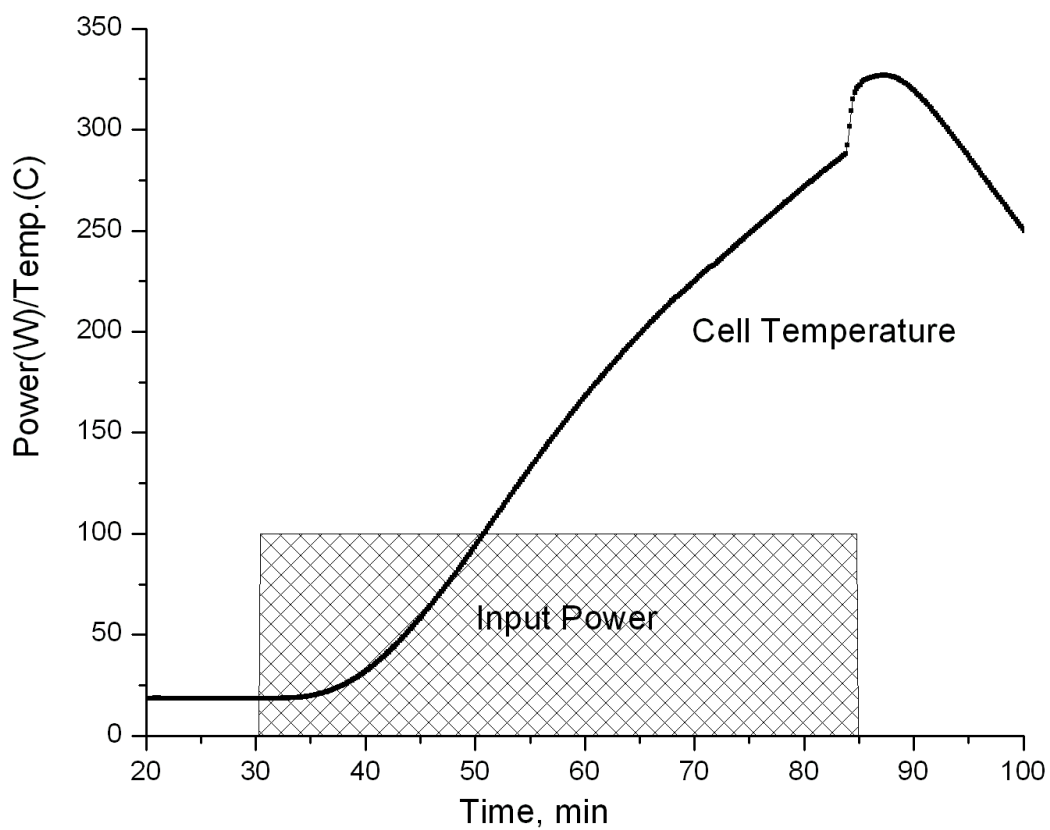
Figure 9. The coolant power with time for the heterogeneous catalyst mixture, 8.3g $KH(s)$ + 5.0g Mg + 20.0g AC + 7.2g $AgCl$. The numerical integration of the input and output power curves with the calibration correction applied yielded the output energy of 367.52 kJ and an input energy of 327.1 kJ corresponding to a net energy of 40.42 kJ.
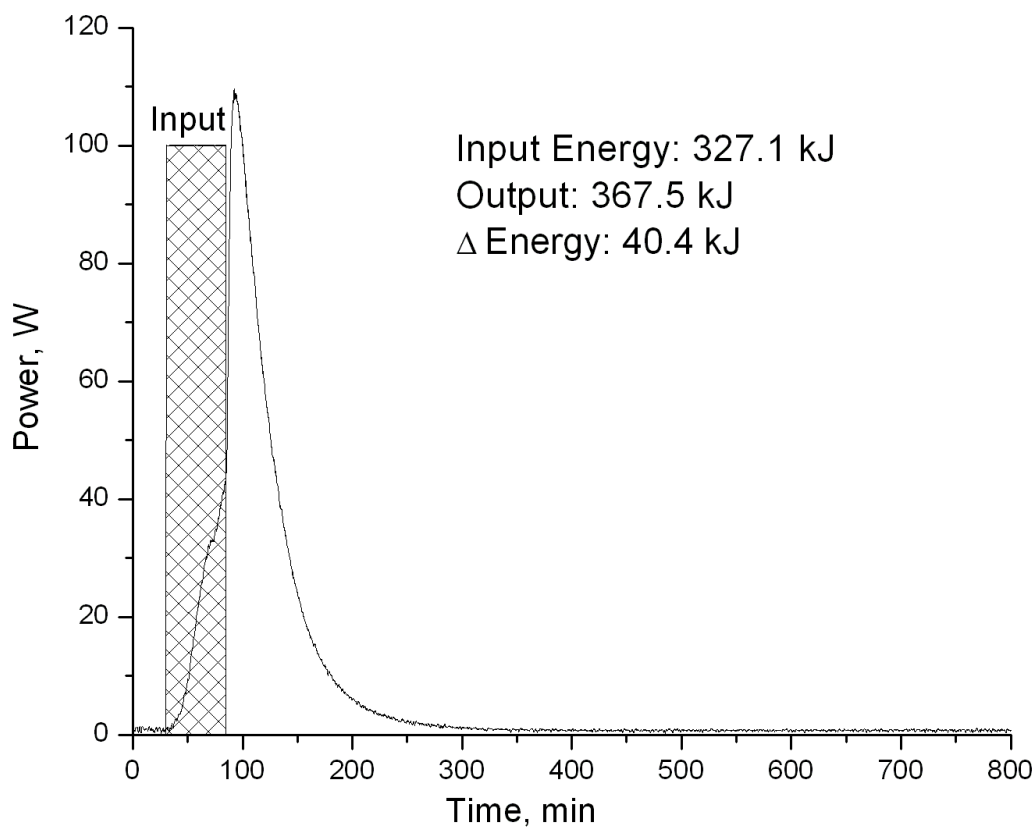
Figure 10. The cell temperature with time due to the indicated constant power for the heterogeneous catalyst mixture, 8.3g $KH(s)$ + 5.0g Mg + 20.0g TiC + 15.6g $EuBr_2$. The reaction liberated 45 kJ of energy in about 60 s to develop a system-response-corrected peak power in excess of 0.75 kW.
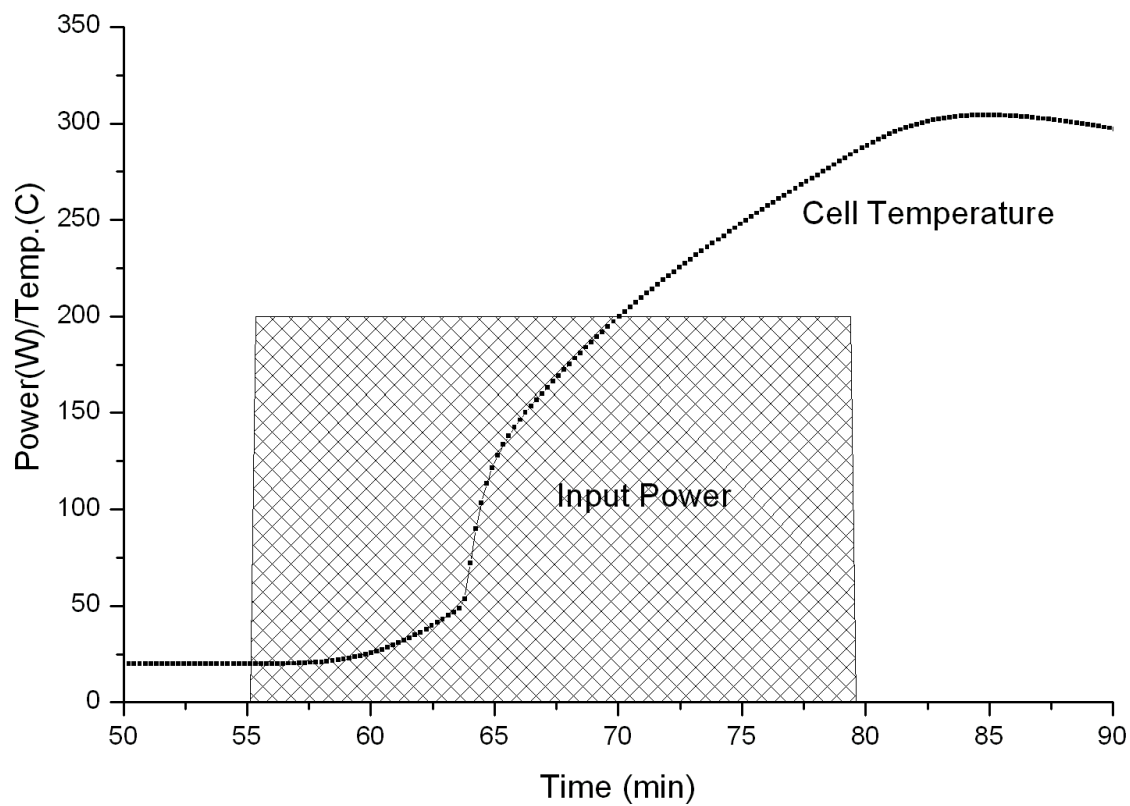
Figure 11. The coolant power with time for the heterogeneous catalyst mixture, 8.3g $KH(s)$ + 5.0g Mg + 20.0g TiC + 15.6g $EuBr_2$. The numerical integration of the input and output power curves with the calibration correction applied yielded the output energy of 336 kJ and an input energy of 291 kJ corresponding to a net energy of 45 kJ.
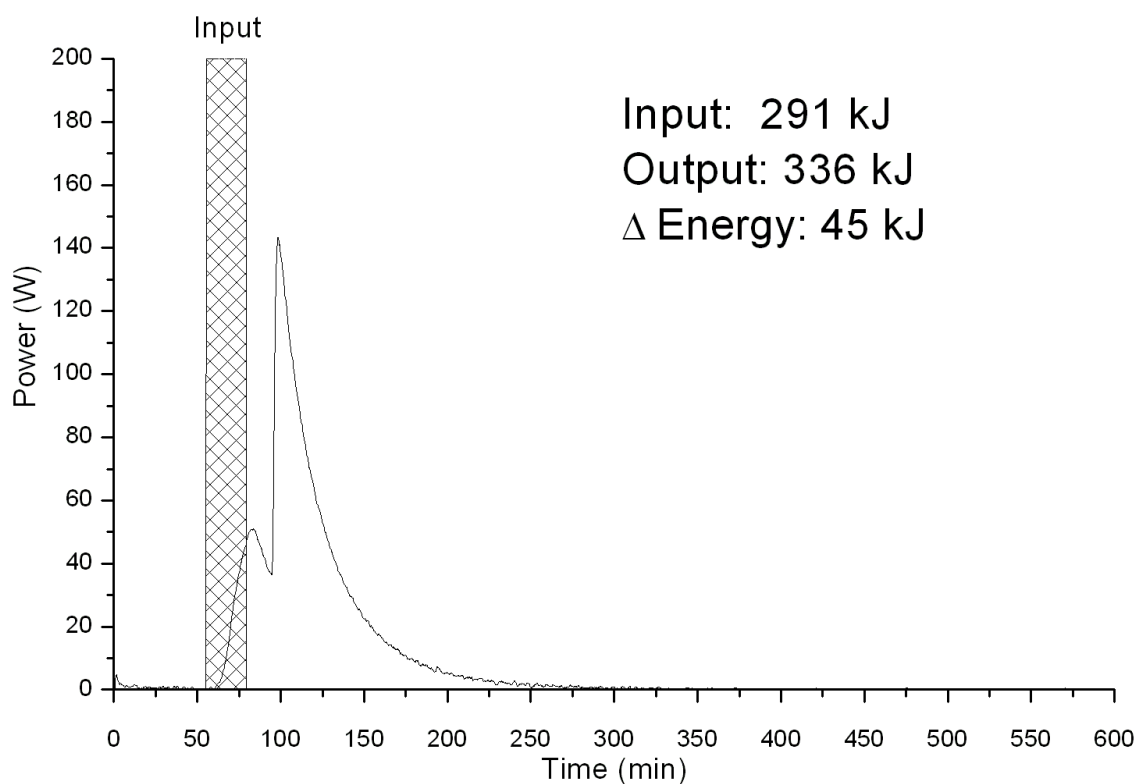
Figure 12. The cell temperature with time due to the indicated constant power for the 10-fold scale-up of the heterogeneous catalyst mixture comprising 50.0g $NaH(s)$ + 50.0g Mg + 200.0g AC + 109.5g $NiBr_2$. The reaction liberated 577 kJ of energy in less than 20 s to develop a system-response-corrected peak power in excess of 30 kW.
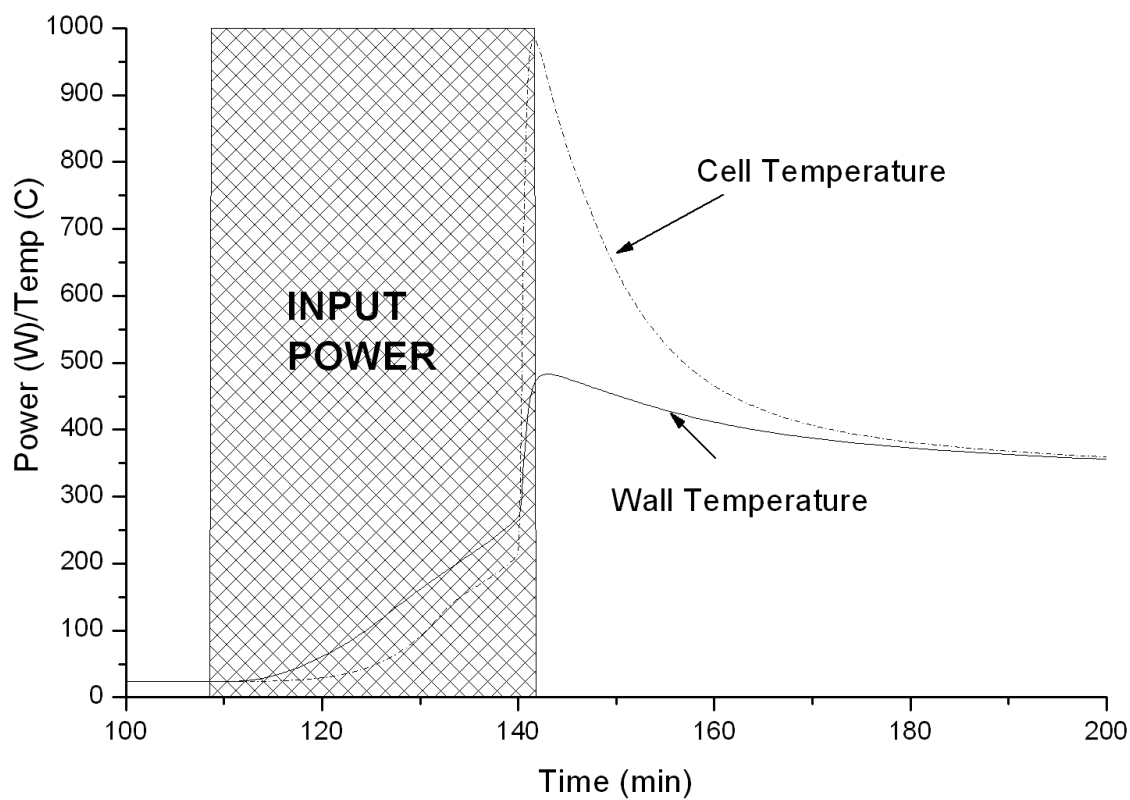
Figure 13. The coolant power with time for the 10-fold scale up of the heterogeneous catalyst mixture comprising 50.0g $NaH(s)$ + 50.0g Mg + 200.0g AC + 109.5g $NiBr_2$. The numerical integration of the input and output power curves with the calibration correction applied yielded the output energy of 2567 kJ and an input energy of 1990 kJ corresponding to a net energy of 577 kJ.
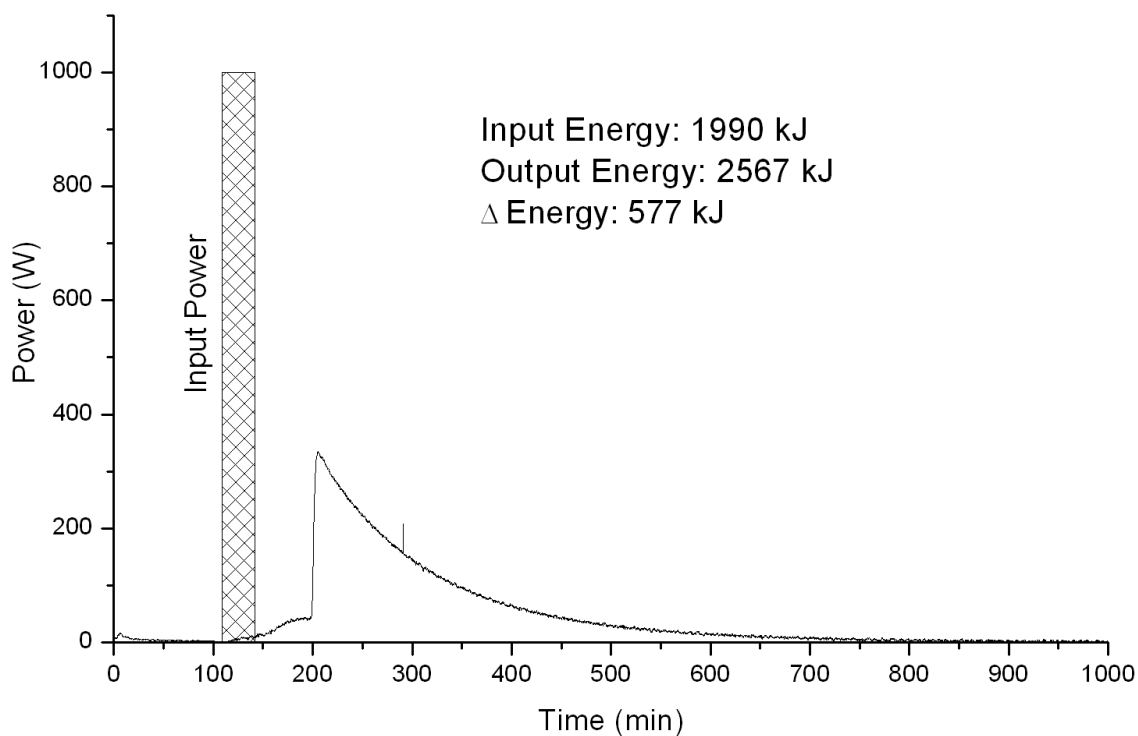
Figure 14. ^1H solution NMR following DMF-d7 solvent extraction of the product of the reaction mixture comprising 1g $NaH(s)$ + 1g MgH_2 mixed with 4g activated carbon and pressurized with 0.0094 moles of SF_6 showed the H^- (1/4) peak at –3.84 ppm. The other peaks in the spectrum are due to DMF (labeled), trace H_2O at 3.62 ppm, and background hydrocarbon peaks from the AC.
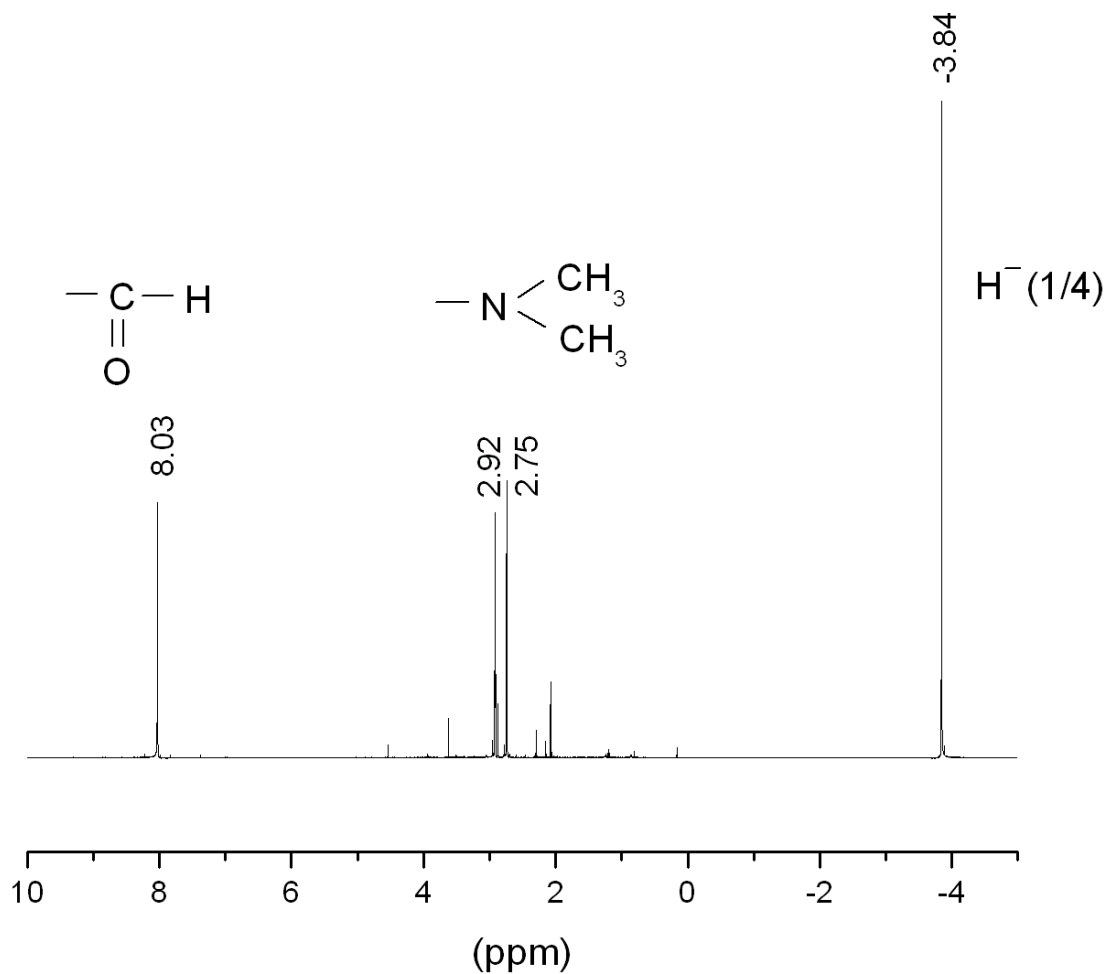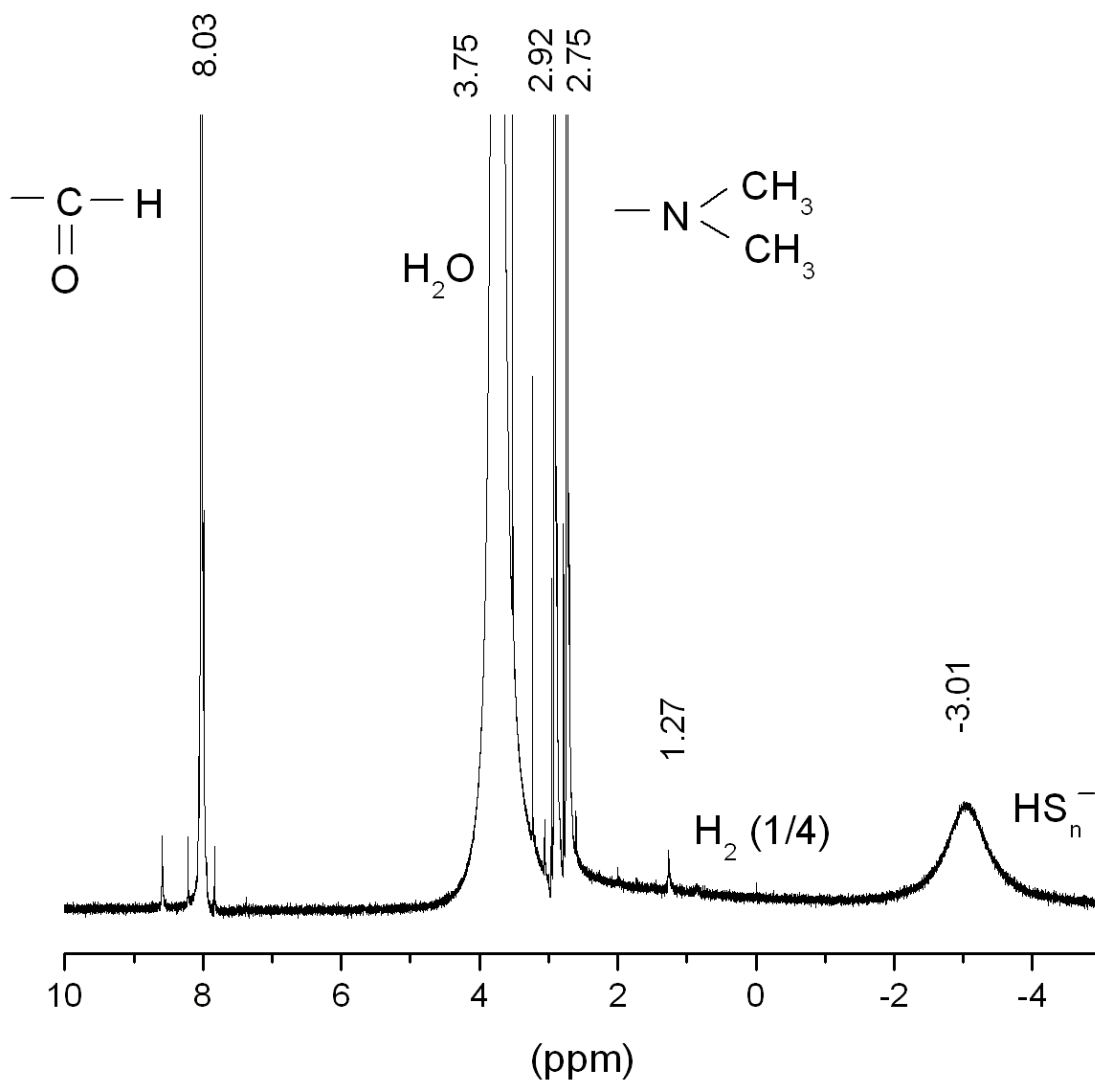
Figure 15. ^1H solution NMR following DMSO-d6 solvent extraction of the product of the reaction mixture comprising 1g $NaH(s)$ + 1g MgH_2 mixed with 4g activated carbon and pressurized with 0.01 moles of SF_6 showed the H^- (1/4) peak at –4.07 ppm and the solvent peak at 2.50 ppm. The presence of the H^- (1/4) peak in two different solvents confirmed that it is not solvent-reaction-product related.
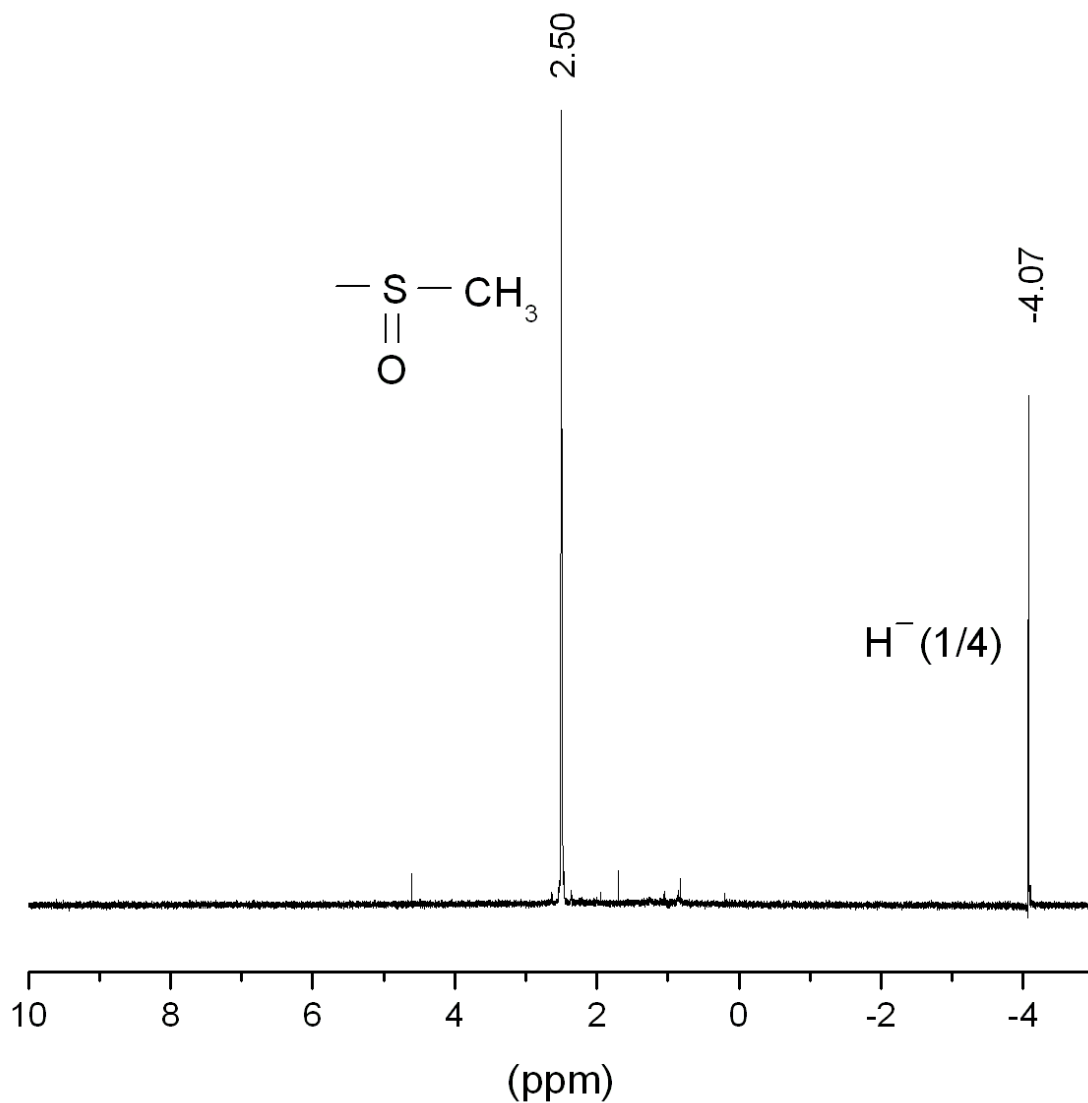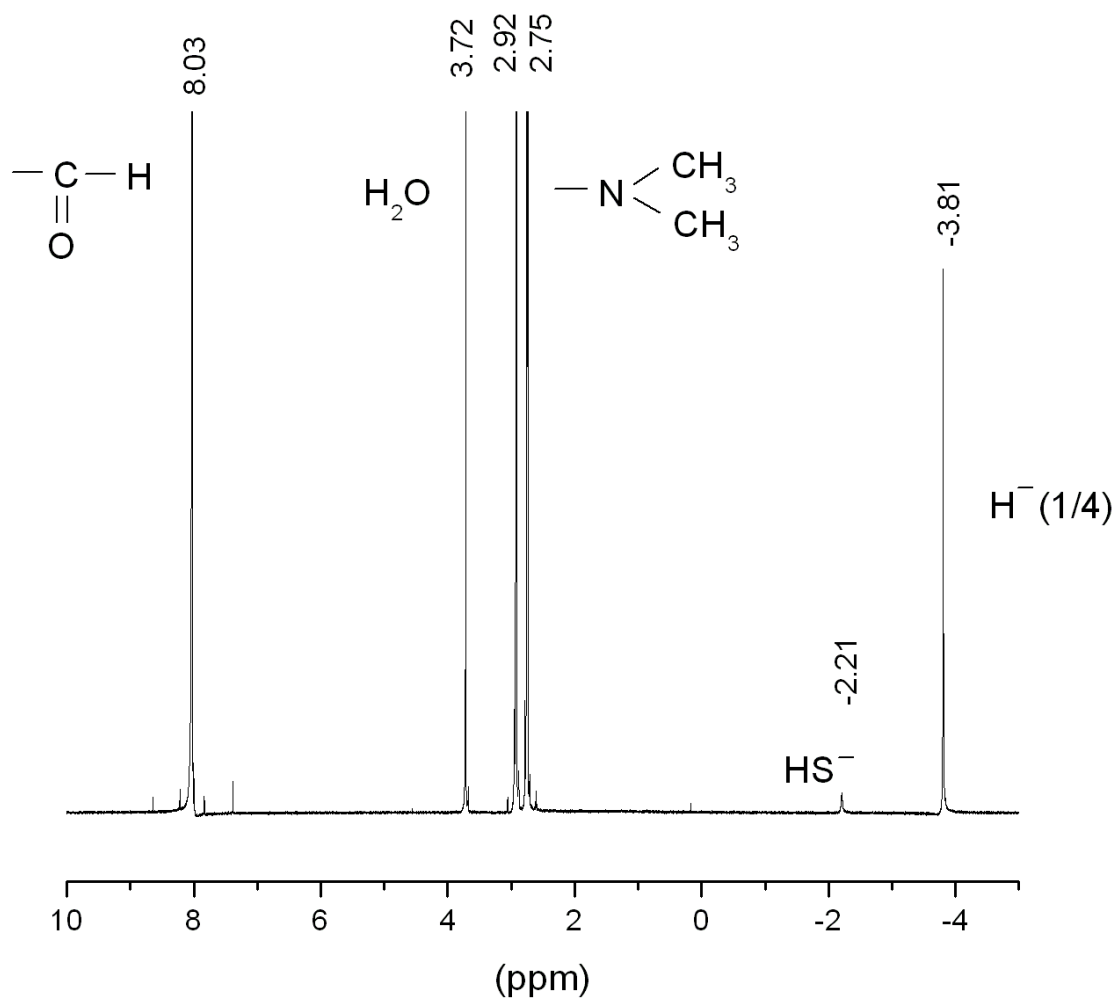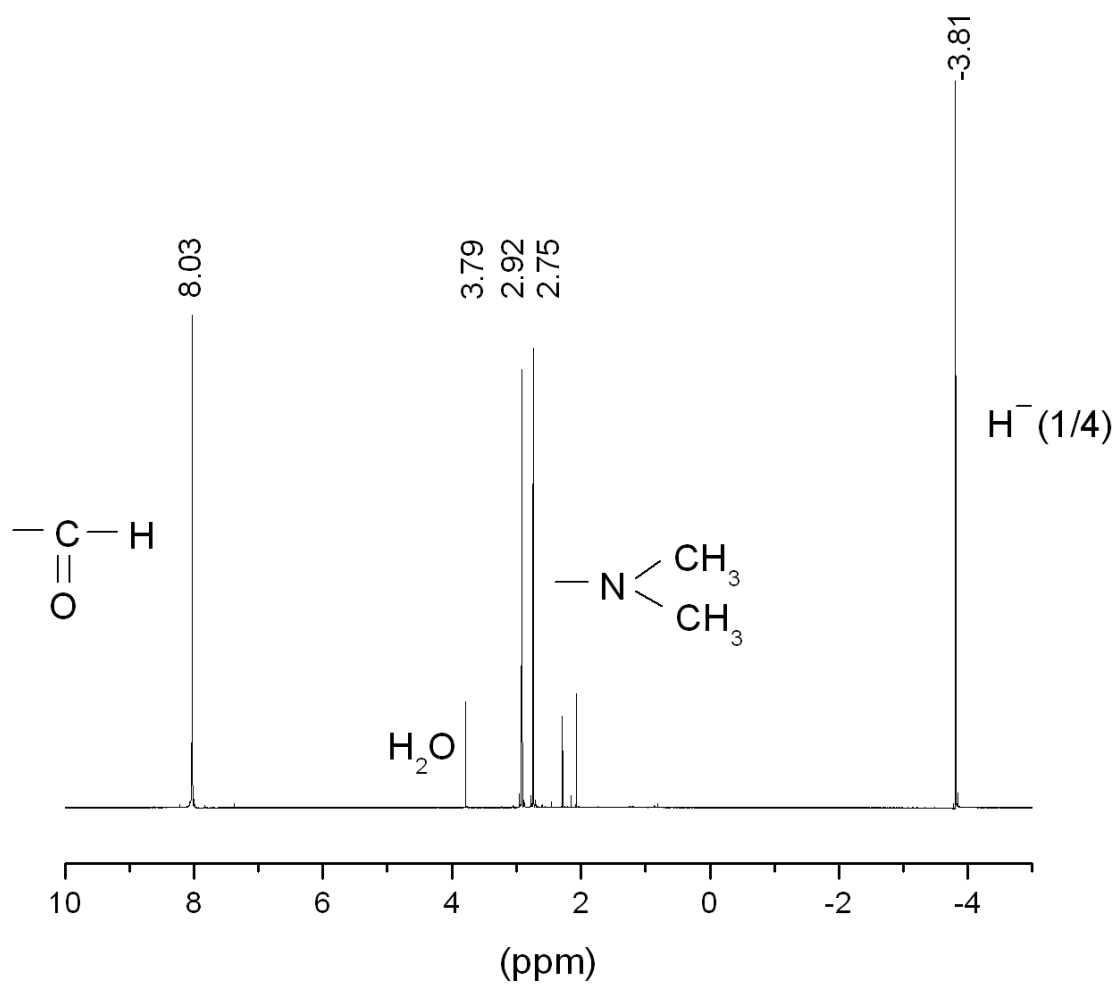
Figure 16. ^1H solution NMR following DMF-d7 extraction of the product of the reaction mixture comprising 1g $NaH(s)$ + 1g MgH_2 mixed with 4g activated carbon and pressurized with 0.0094 moles of SF_6 and its reaction with trace water at 50 °C. The −3.84 ppm peak shifted slightly to −3.74 ppm and decreased and broadened significantly. Concomitantly, the water peak at 3.61 ppm became broader indicating a water interaction.
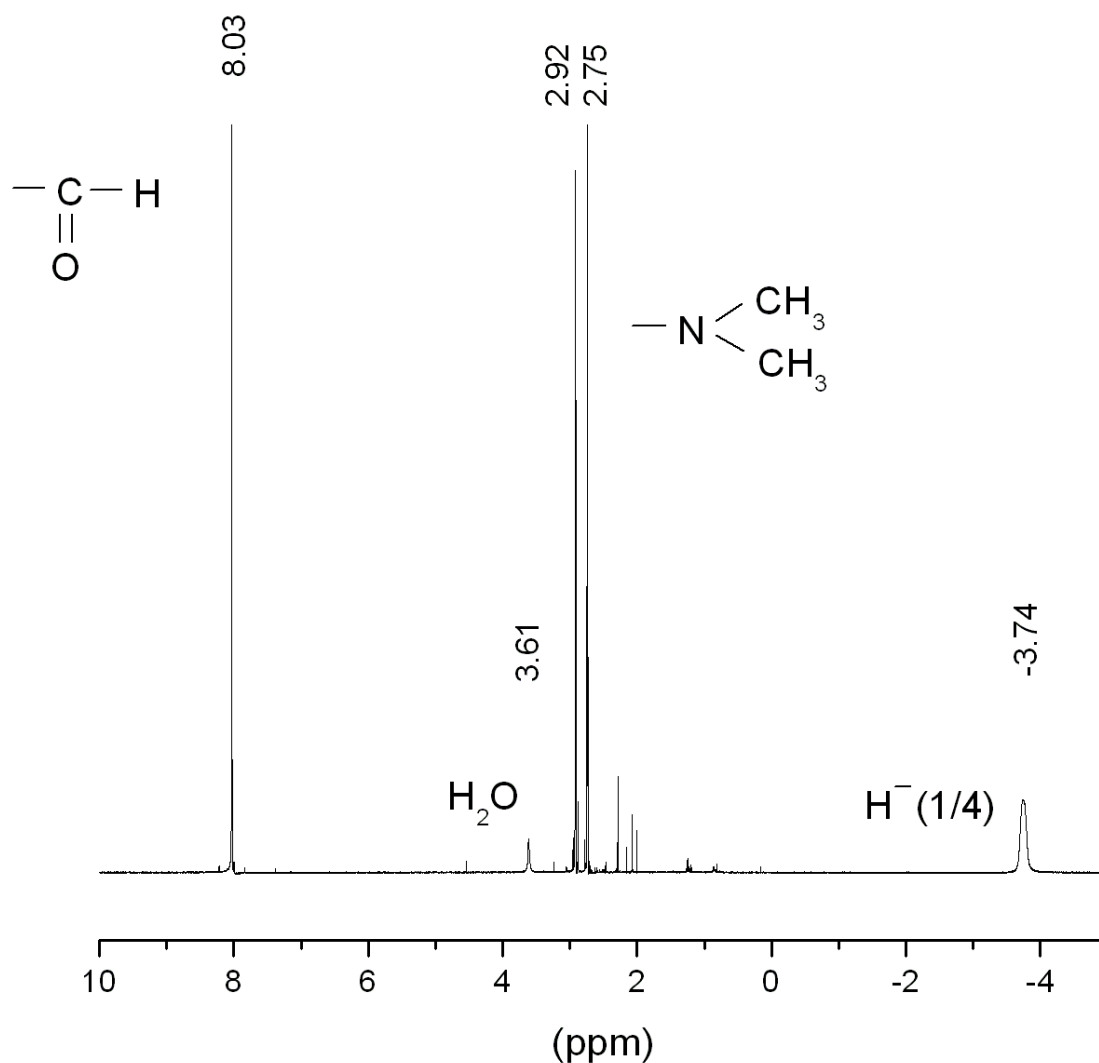
Figure 17. ^1H solution NMR following DMF-d7 solvent extraction of *NaHS* showing the predicted H^- (1/4) peak at −3.80 ppm. The other peaks in the spectrum are due to DMF (labeled).
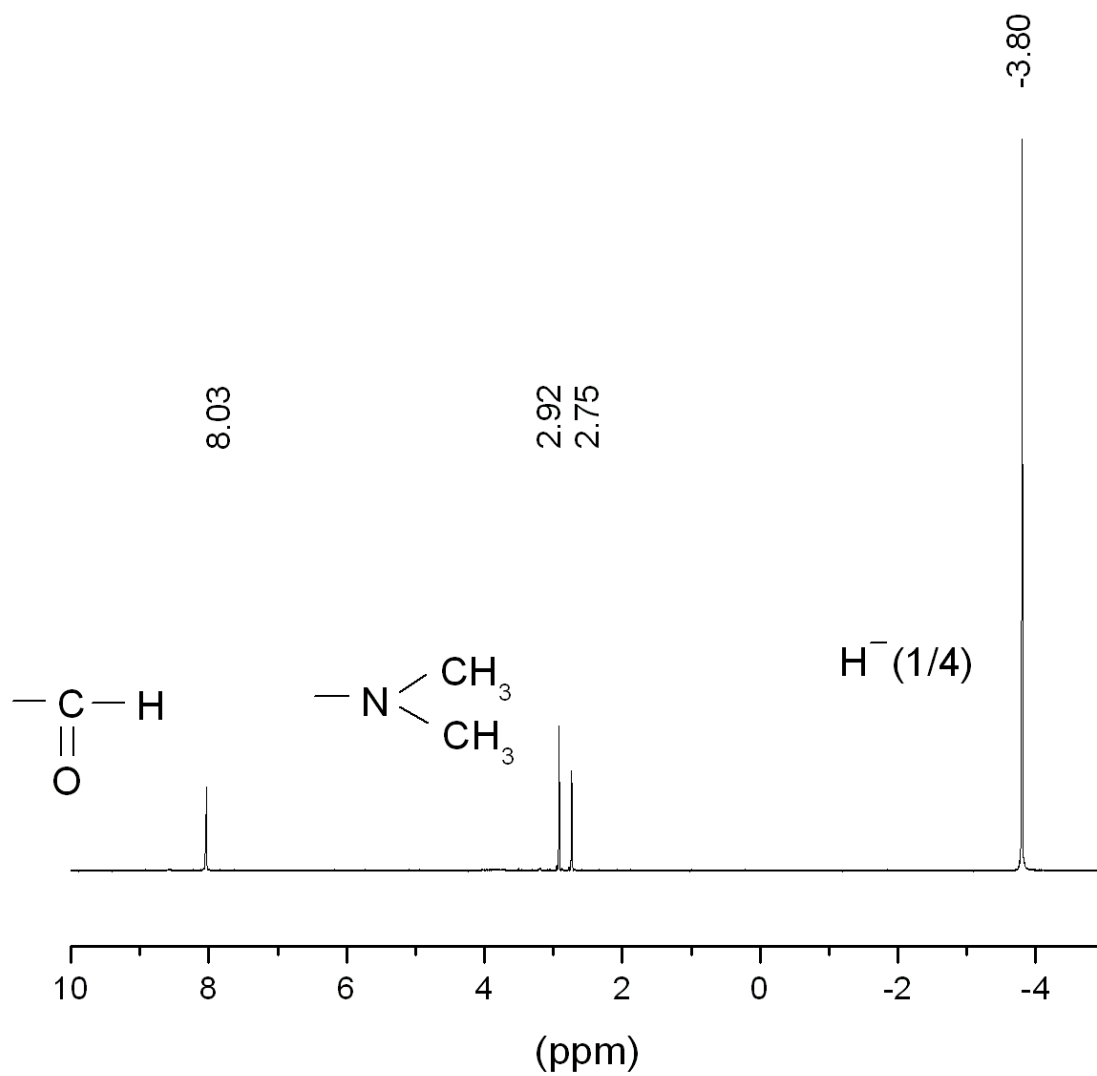
Figure 18. ^1H solution NMR of *HCl* added to 0.1 M *NaHS* in D_2O. The H_2S peak at 1.96 ppm increased with decreasing pH; whereas, the opposite relationship was observed for the HS^- peak at –2.17 ppm. The D_2O solvent peak was observed at 4.80 ppm and some DMF peaks, possibly residual solvent peaks from the synthesis of *NaHS*, were present.
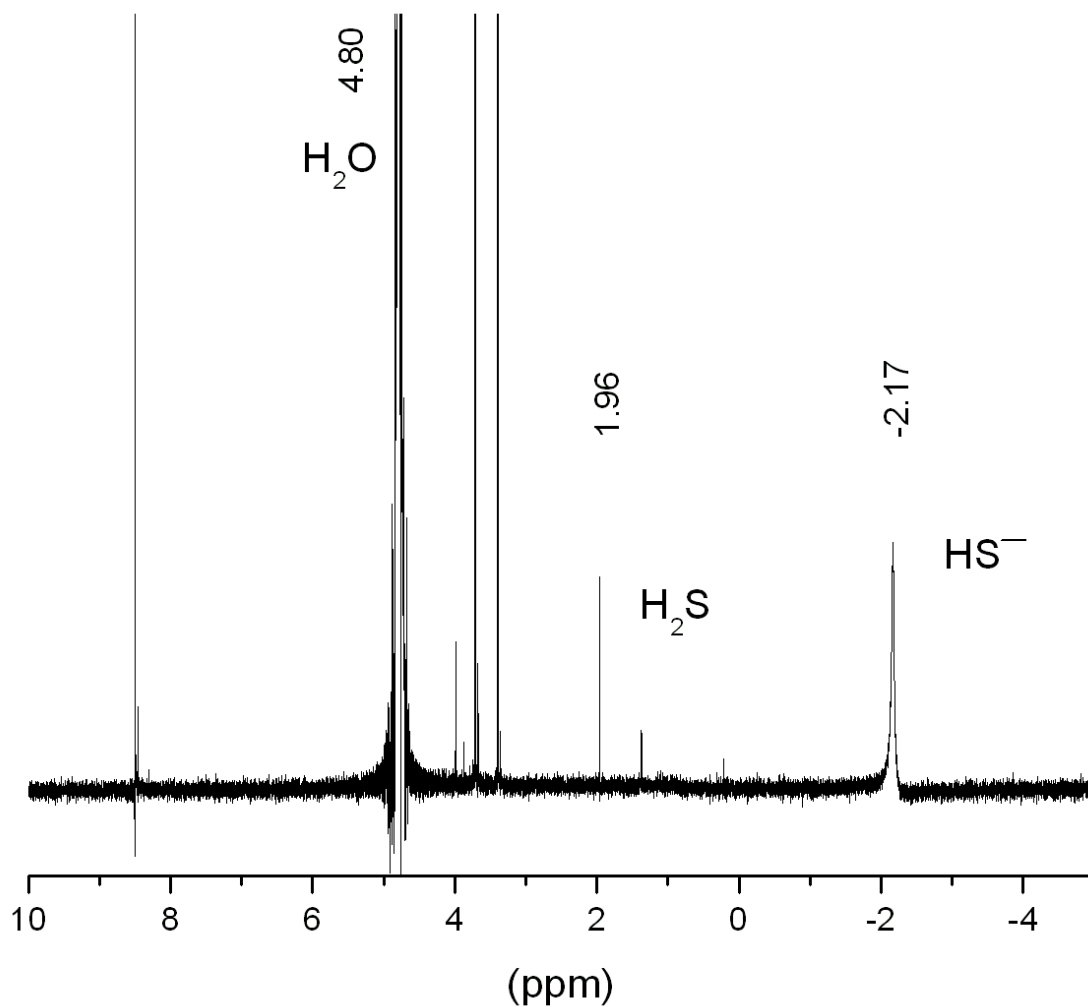
Figure 19. ^1H solution NMR of H_2S in DMF-d7 showing the H_2S peak at 1.77 ppm. The other peaks in the spectrum are due to DMF (labeled).
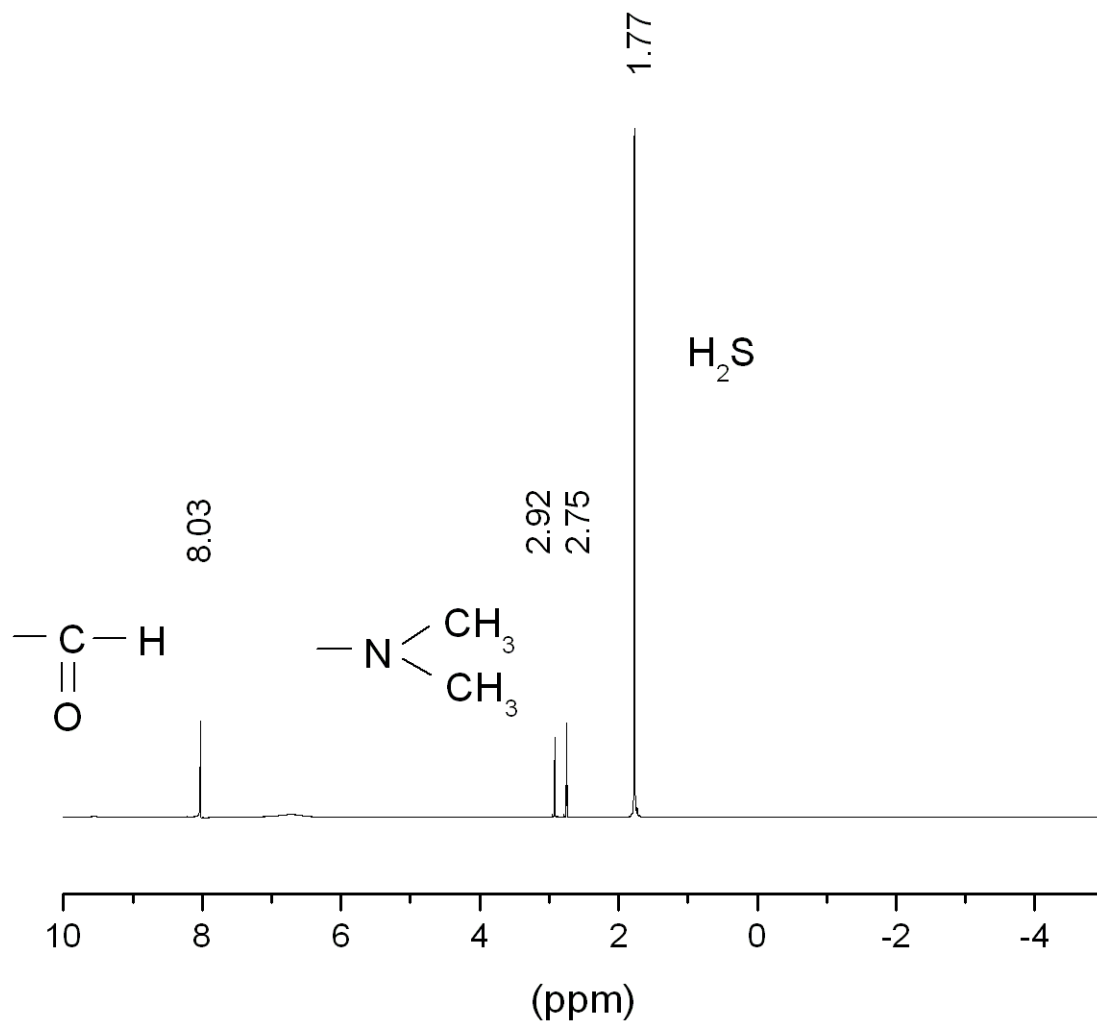
Figure 20. ^1H solution NMR of H_2S in D_2O added to DMF showing the H_2S peak at 1.76 ppm. The other peaks in the spectrum are due to DMF (labeled) and the water peak at 3.85 ppm.
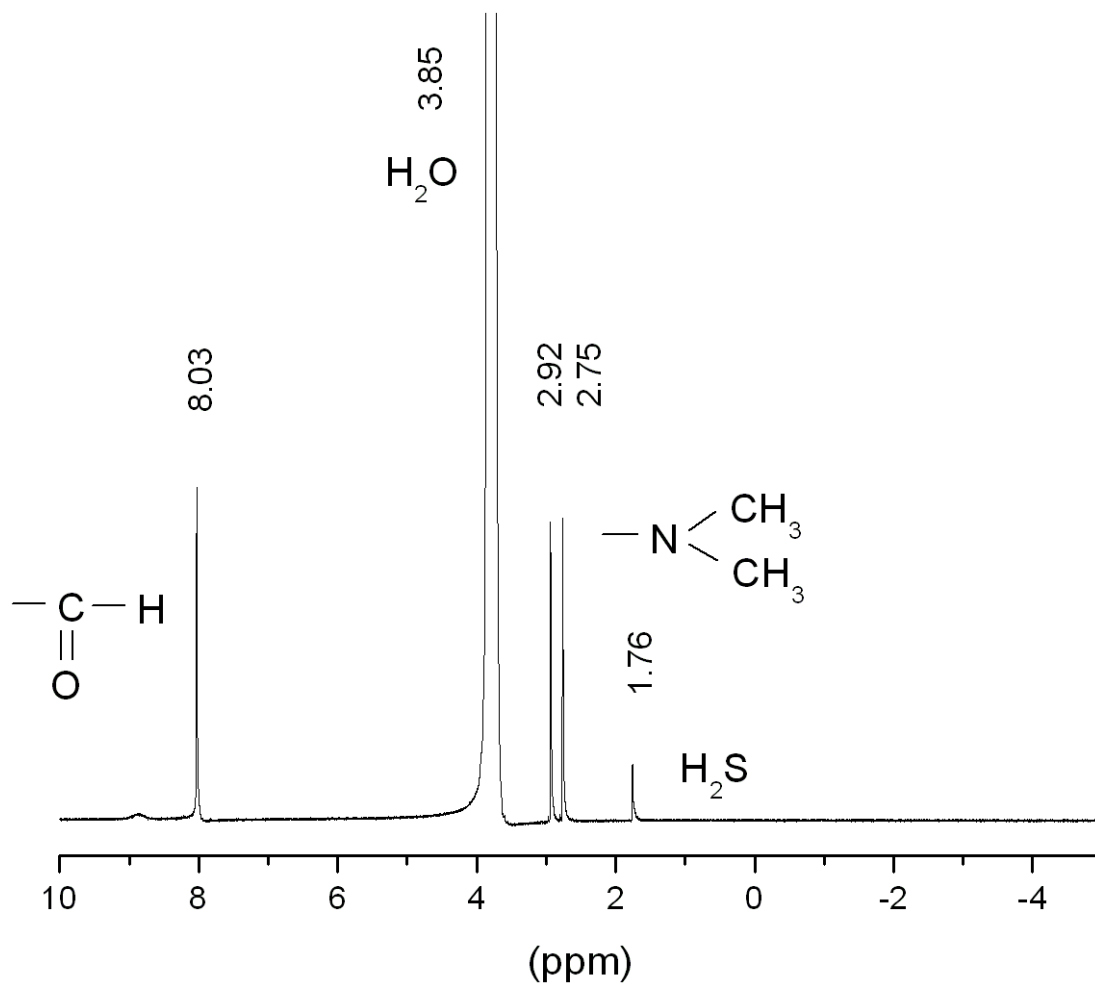
Figure 21. ^1H solution NMR of H_2S bubbled into a 0.25 M solution of $NaOH$ dissolved in D_2O until the pH was 9.0 showing an intense HS^- peak at –2.08 ppm and an acetone peak at 2.27 ppm.
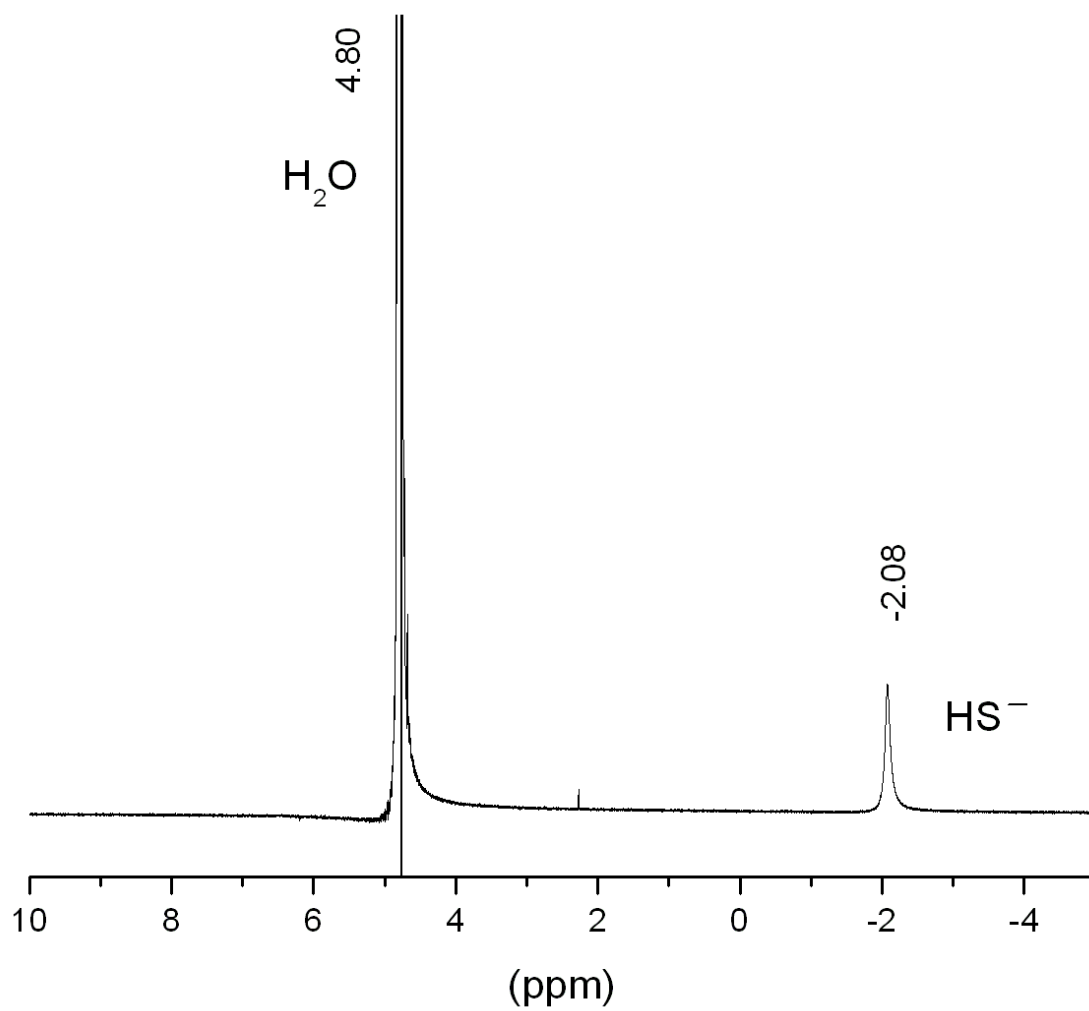
Figure 22. ^1H solution NMR of H_2S bubbled into a 0.25 M solution of *NaOH* dissolved in *D_2O* until the pH was 9.0 and then added to DMF-d7. For the prepared hydrino-free *NaHS* in DMF, a broad *HS^-* peak was observed at –2.73 ppm that was similar to the *HS^-* peak in *D_2O*.
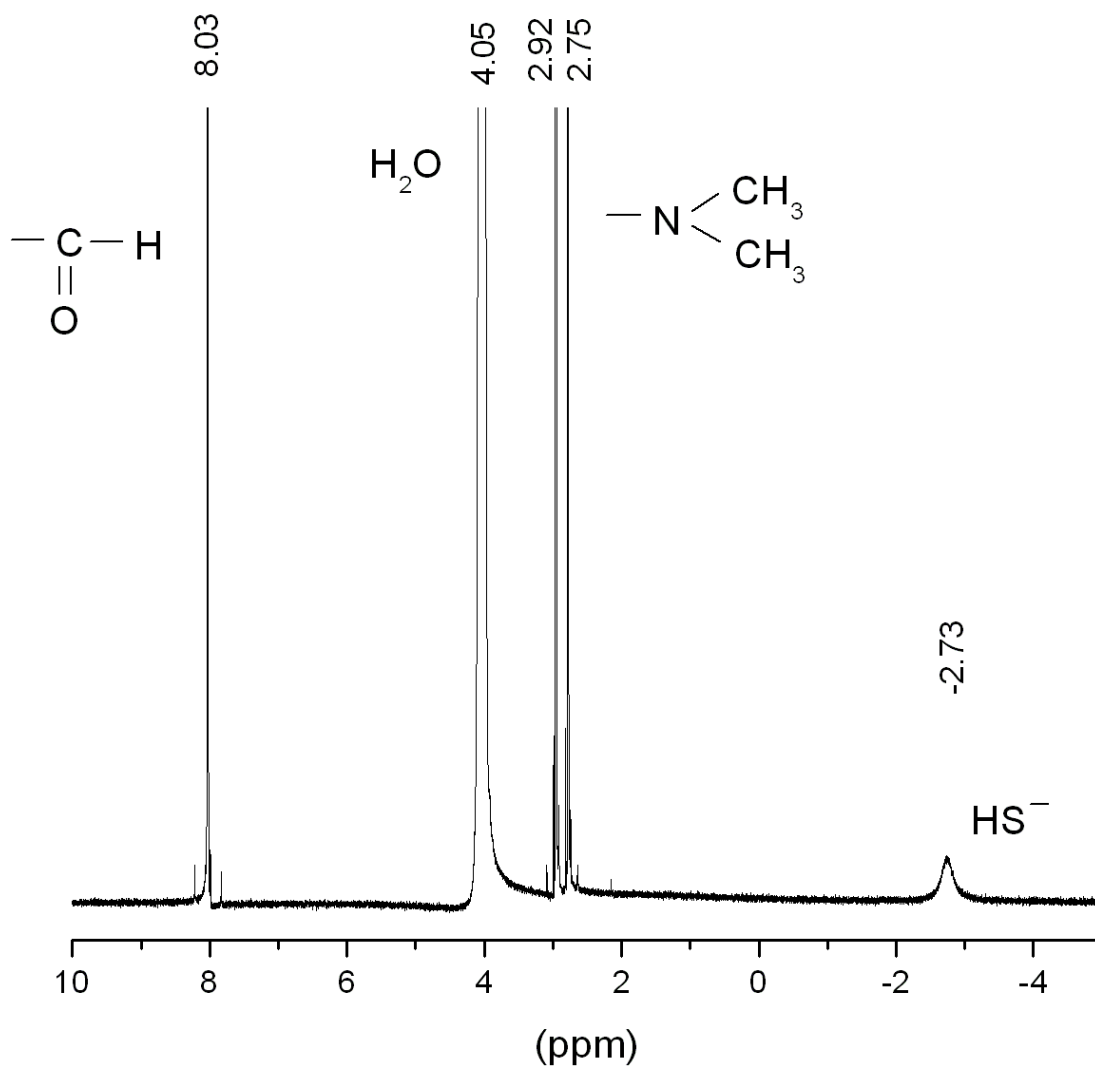
Figure 23. ^1H solution NMR of a saturated solution of *NaHS* in D_2O added to DMF-d7 solvent showing a very broad peak at −3.01 ppm. Since hydrino hydride reacts with water, the very broad peak in the region of about −3.01 ppm was assigned to HS_n^-. The H_2 (1/4), the predicted reaction product of water and H^- (1/4) was observed at 1.27 ppm.
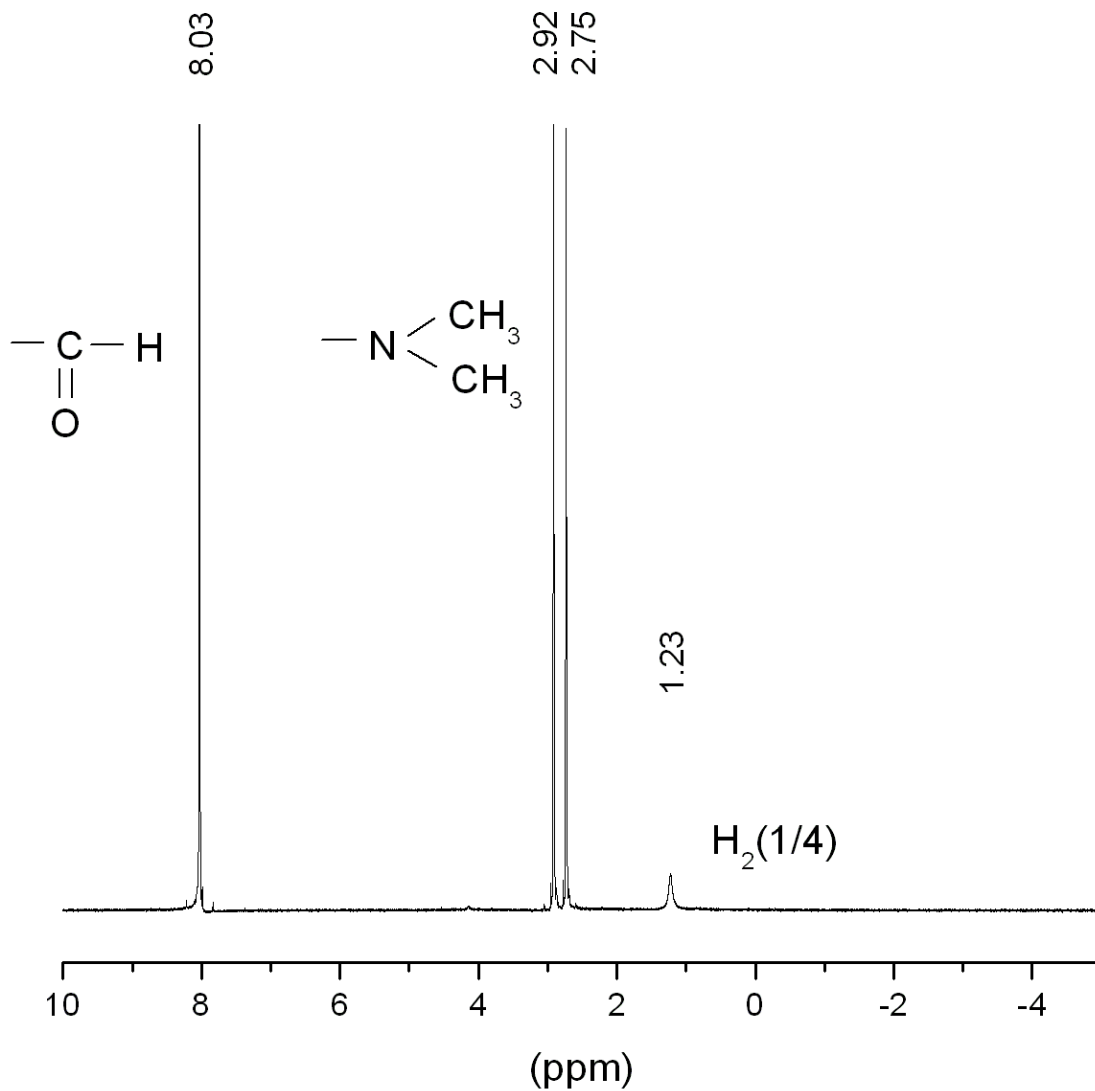
Figure 24. ^1H solution NMR following DMF-d7 solvent extraction of the product of the reaction mixture comprising 1.32g $LiH(s)$ + 3g Al powder + 12g AC + 3.9g S formed in the chemical cell. Both the H^- (1/4) peak at –3.81 ppm and the HS^- peak at –2.21 ppm were observed definitively eliminating the latter as the source of the –3.81 ppm peak.
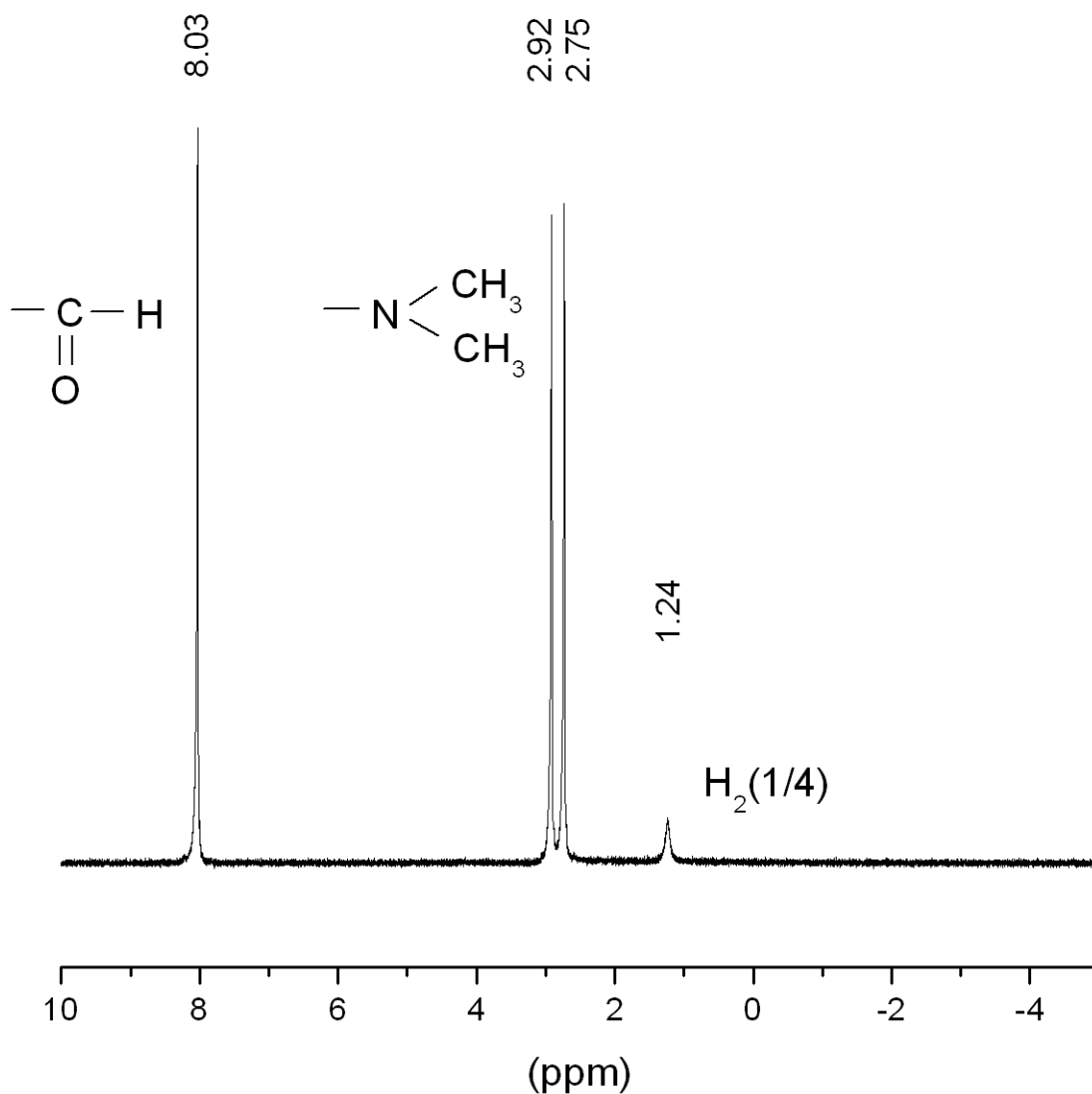
Figure 25. ^1H solution NMR following DMF-d7 solvent extraction of the product of the reaction mixture comprising 0.33g $LiH(s)$ + 1g Al powder + 4g AC + 1.3g S showed the H^- (1/4) peak at –3.81 ppm.

Figure 26. ^1H solution NMR following DMF-d7 solvent extraction of the product of the reaction mixture comprising 1.66g $KH(s)$ + 1g Al powder + 4g AC + 1.3g S showed the H^- (1/4) peak at –3.86 ppm.
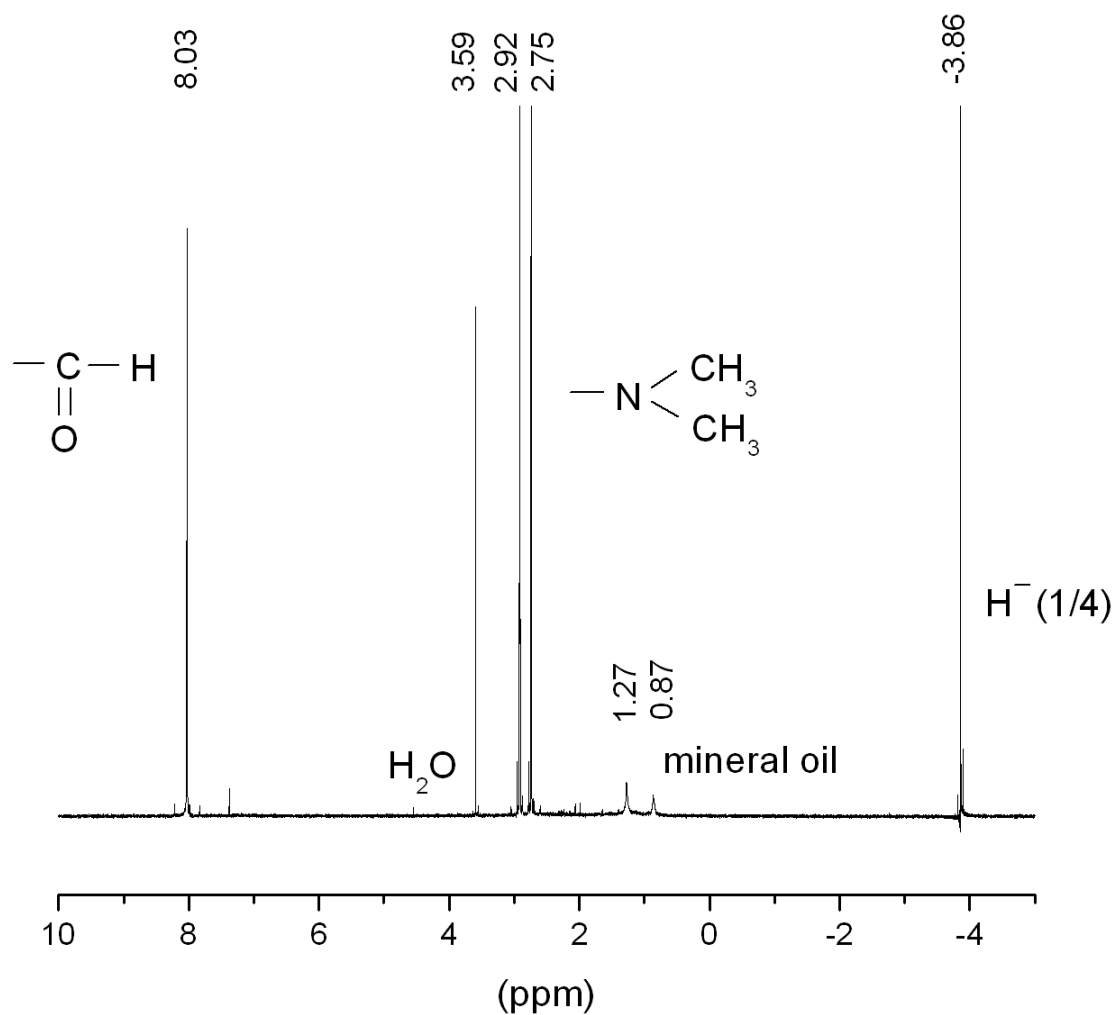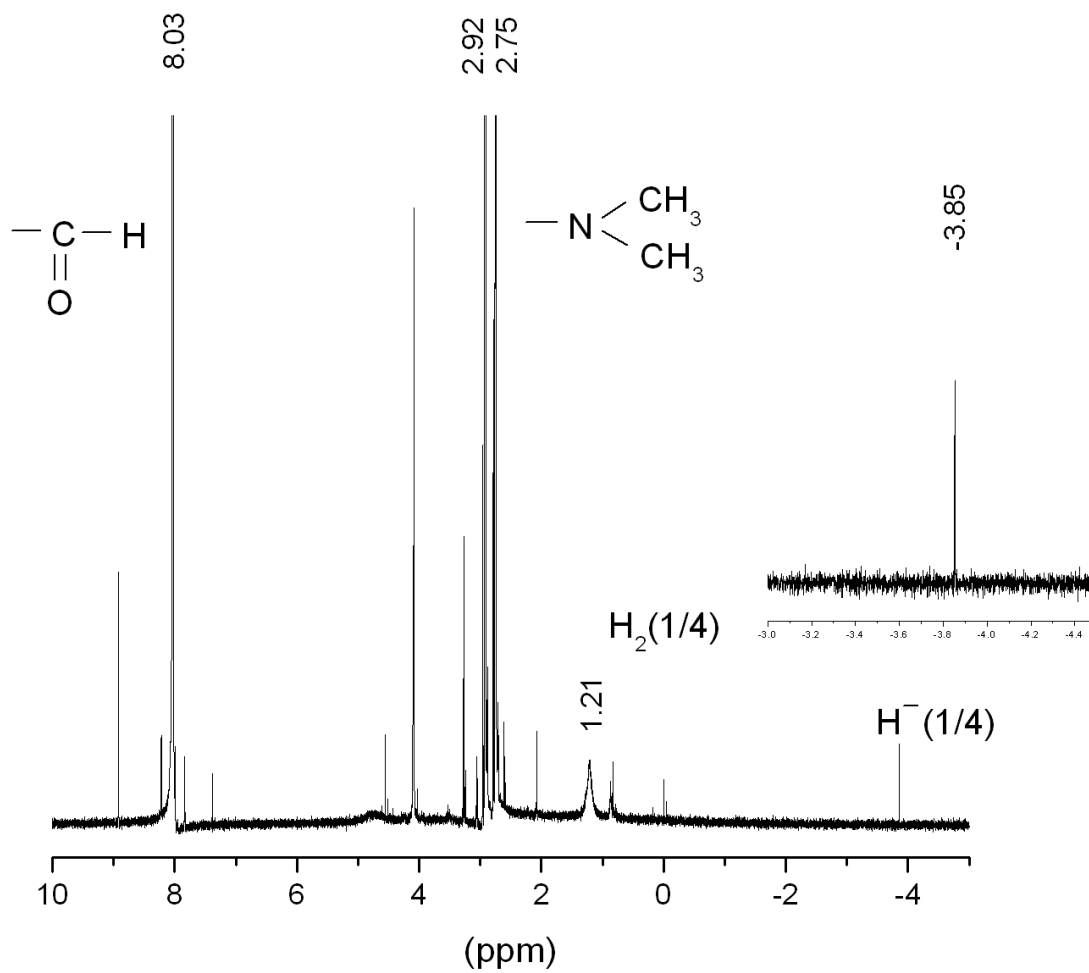
Figure 27. ^1H solution NMR following DMF-d7 solvent extraction of the product of the reaction mixture comprising 1g $NaH(s)$ + 1g MgH_2 powder + 4g AC + 3.2g S showed the H^- (1/4) peak at −3.34 ppm.
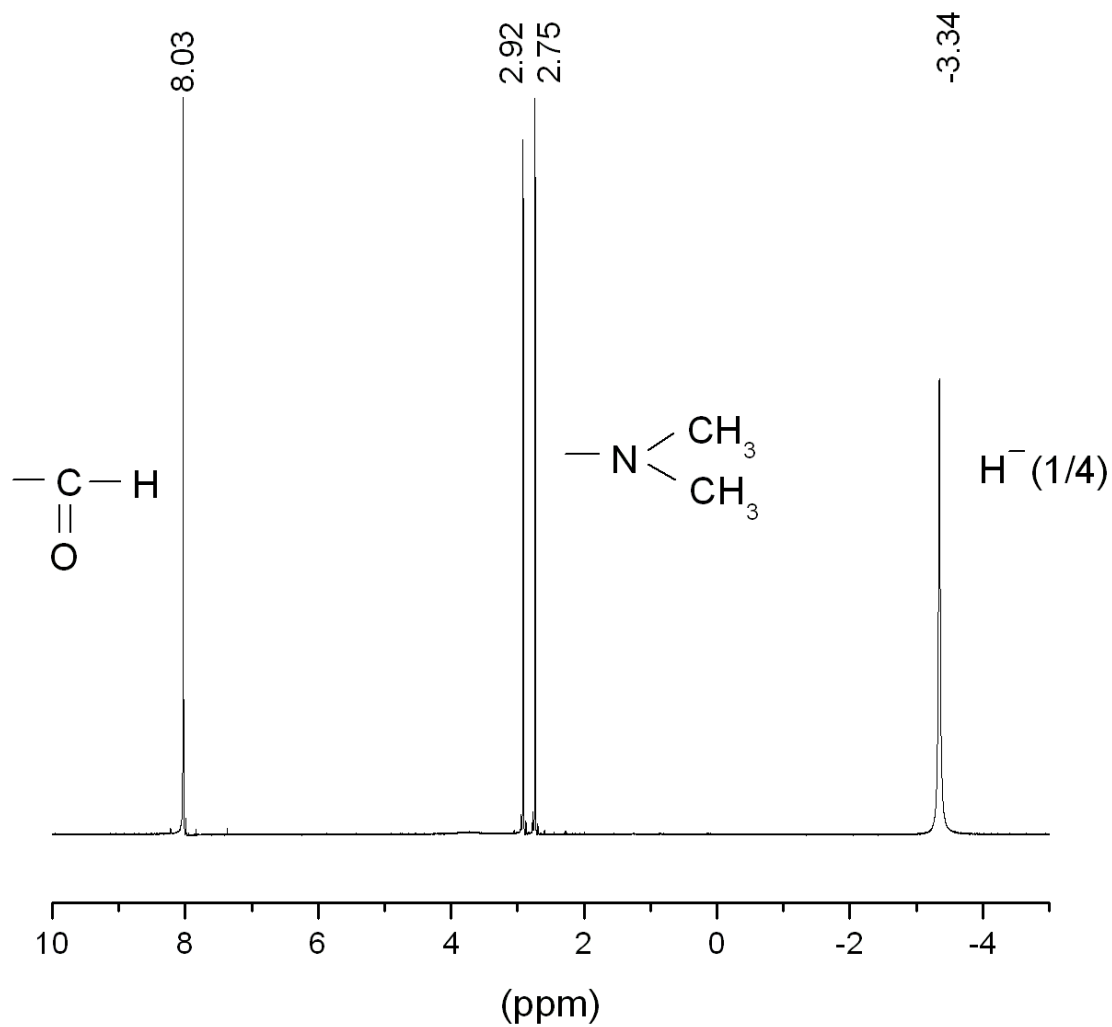
Figure 28. ^1H solution NMR of 5 mg of sulfur added to DMF-d7 extracted *NaHS* showing that the *H⁻* (1/4) peak shifted from −3.81 ppm to −3.37 ppm.
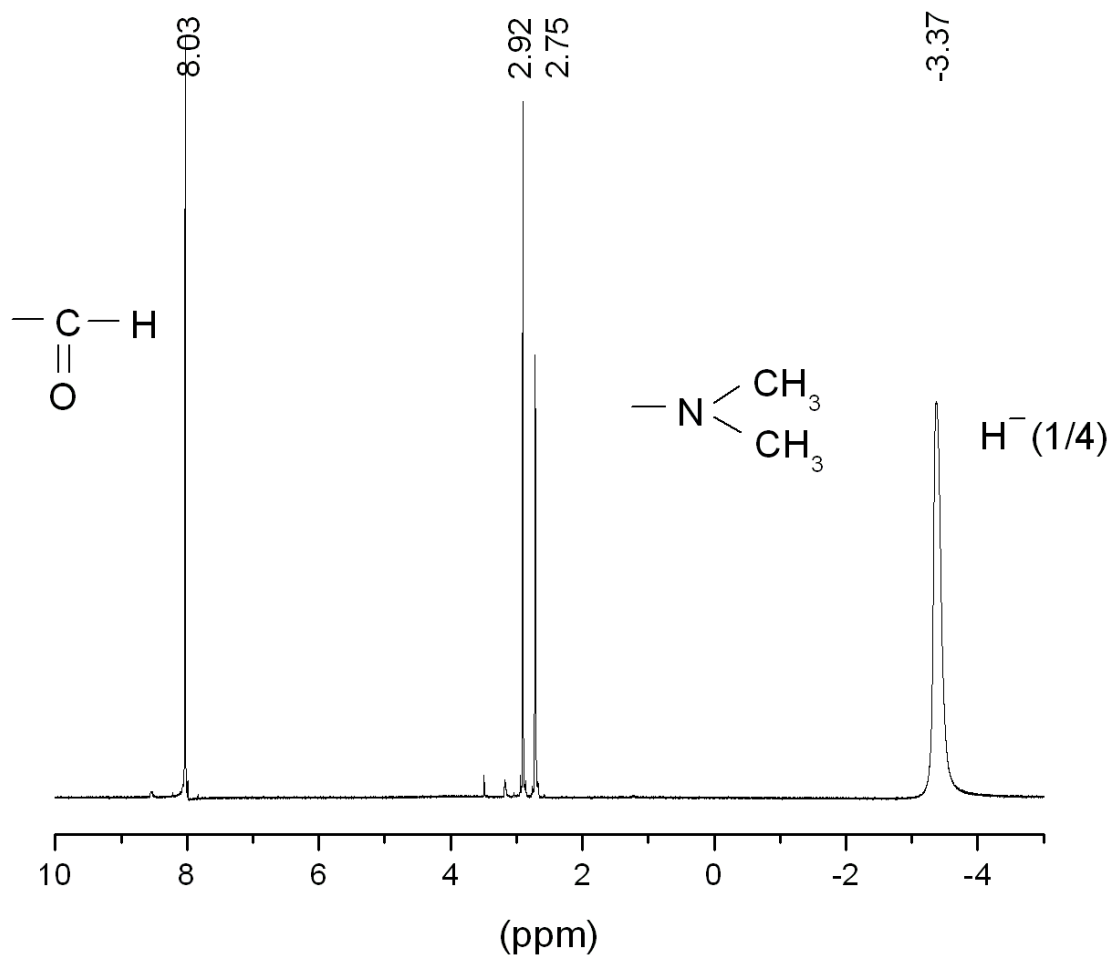
Figure 29. ^1H solution NMR following DMF-d7 solvent extraction of the product of the reaction mixture comprising 1g $NaH(s)$ + 1.66g Ca + 4g AC + 3.09g MnI_2 that showed the H_2 (1/4) peak at 1.23 ppm. Similarly to the case with 5.0g of Mg shown in Figures 6 and 7, the net energy of a five-fold scale-up was 61.3 kJ compared to the maximum theoretical of 29.5 kJ corresponding to an excess of 31.8 kJ due to forming H_2 (1/4), a gain of 2.08 times. Ca substituted for Mg as the reductant served as a superior getter for the molecular hydrino.
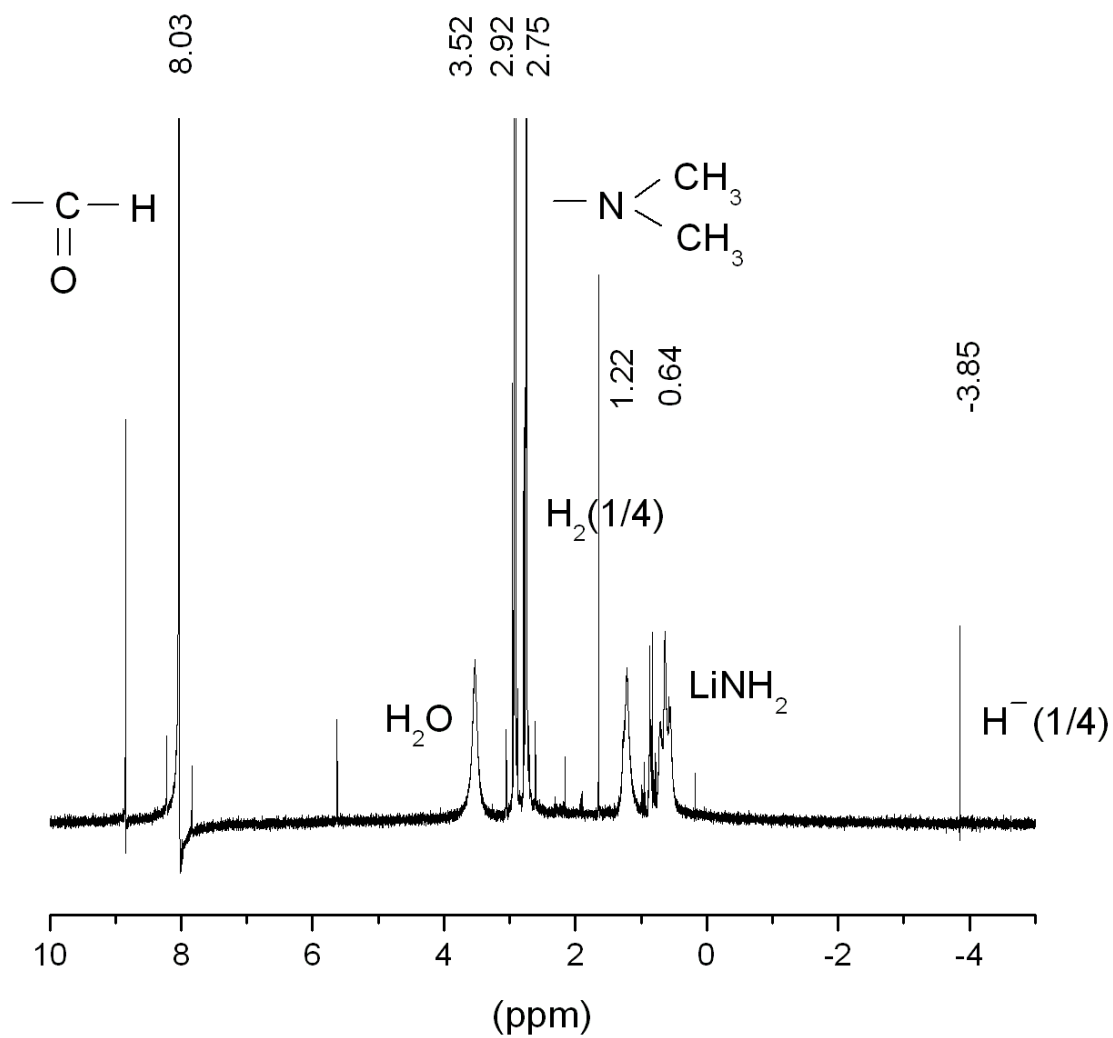
Figure 30. ^1H solution NMR following DMF-d7 solvent extraction of the product of the reaction mixture comprising 1g $NaH(s)$ + 3.67g Sr + 4g AC + 3.09g MnI_2 that showed the H_2 (1/4) peak at 1.24 ppm. Sr substituted for Mg as the reductant served as a superior getter for the molecular hydrino.
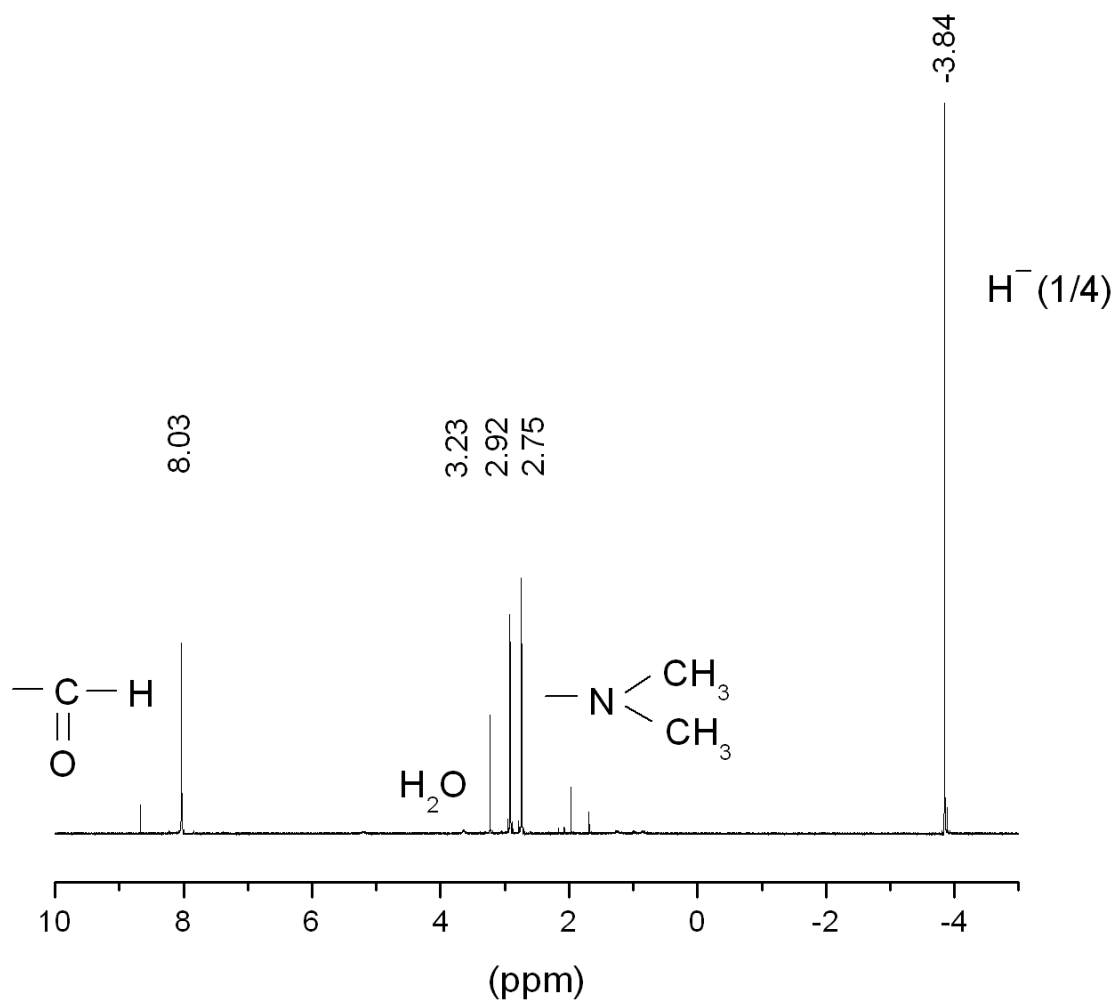
Figure 31. ^1H solution NMR following DMF-d7 solvent extraction of the product of the reaction mixture comprising 1.66g $KH(s)$ + 1g Al NP mixed with 4g activated carbon and pressurized with 0.01 moles of CF_4 that showed the H_2 (1/4) peak at 1.21 ppm and the H^- (1/4) peak at -3.85 ppm.
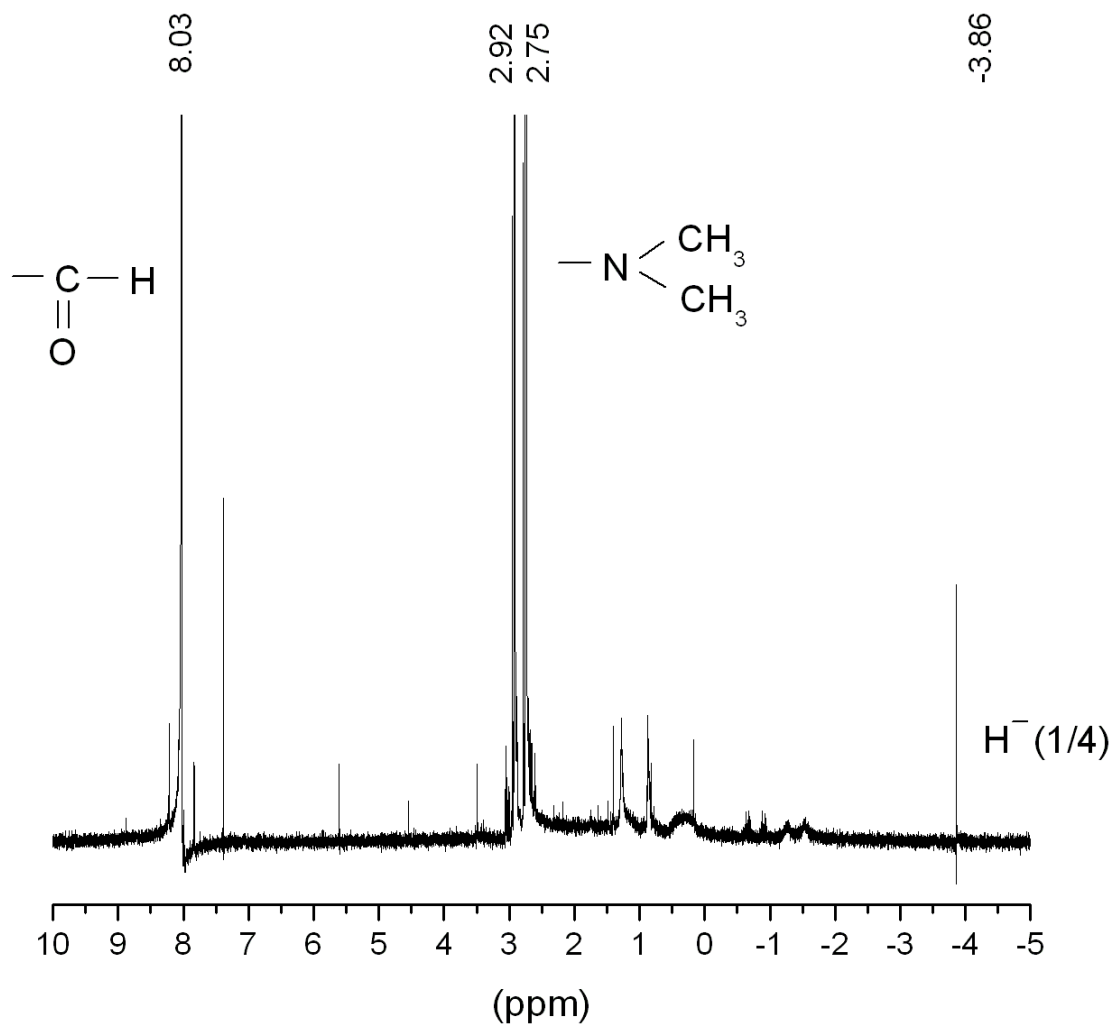
Figure 32. ^1H solution NMR following DMF-d7 solvent extraction of the product of the reaction mixture comprising 0.5g $NaH(s)$ + 0.5g Al NP mixed with 4g activated carbon and pressurized with 0.002 moles of NF_3 that showed the H_2 (1/4) peak at 1.22 ppm and the H^- (1/4) peak at -3.85 ppm.
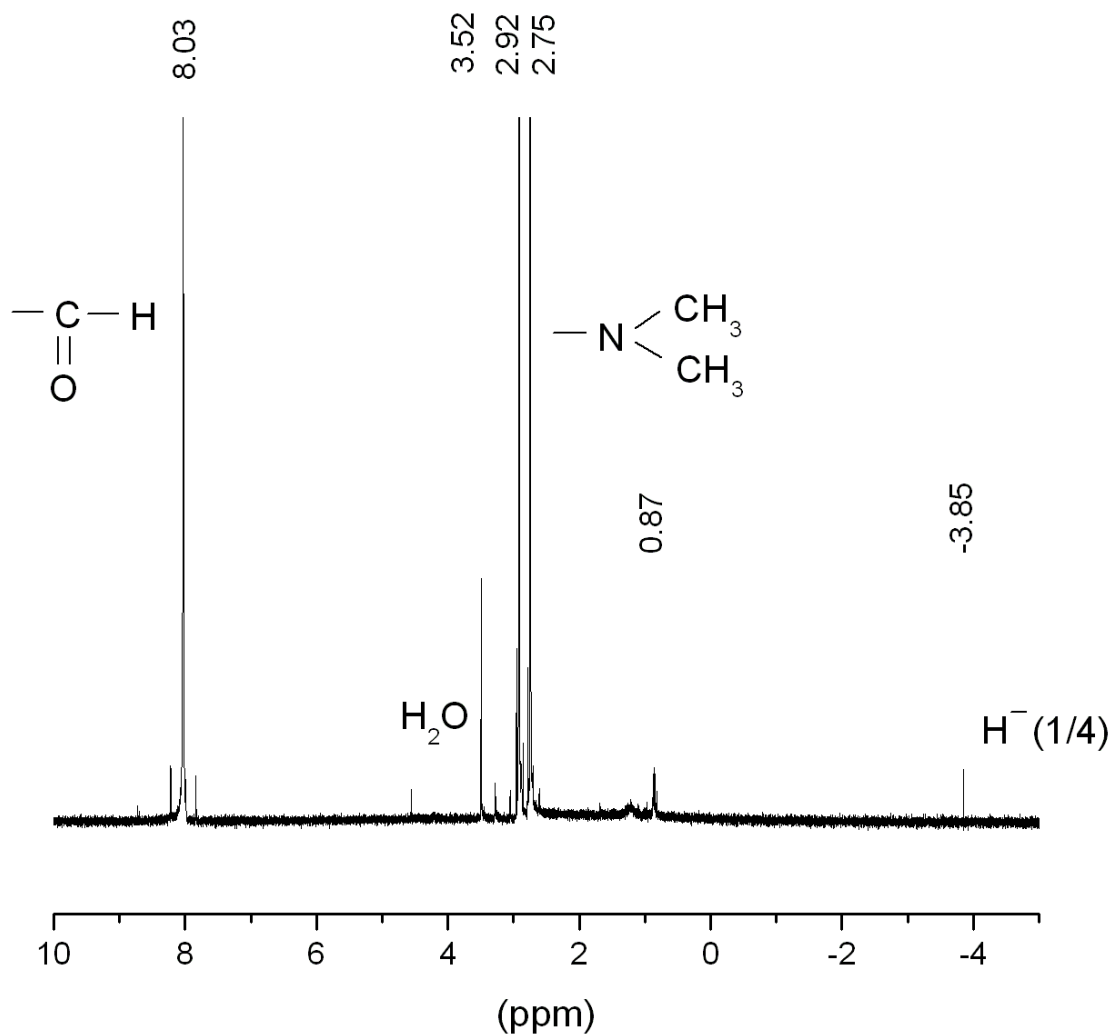
Figure 33. ^1H solution NMR following DMF-d7 solvent extraction of the product of the reaction mixture comprising 1.66g $KH(s)$ + 1g MgH_2 powder + 4g AC + 2.5g $LiNO_3$ that showed the H_2 (1/4) peak at 1.22 ppm and the H^- (1/4) peak at –3.85 ppm.

Figure 34. ^1H solution NMR following DMF-d7 solvent extraction of the product of the reaction mixture comprising 1g $NaH(s)$ + 1g MgH_2 powder + 4g AC + 2.7g $K_2S_2O_8$ + 0.5g Ag that showed the H^- (1/4) peak at −3.84 ppm.

Figure 35. ^1H solution NMR following DMF-d7 solvent extraction of the product of the reaction mixture comprising 1.66g $KH(s)$ + 1g MgH_2 powder + 4g AC + 2g P_2O_5 that showed the H^- (1/4) peak at –3.86 ppm.

Figure 36. ^1H solution NMR following DMF-d7 solvent extraction of the product of the reaction mixture comprising 1.66g $KH(s)$ + 1g Mg powder + 4g AC + 3.92g $EuBr_3$ that showed the H_2 (1/4) peak at 1.23 ppm.
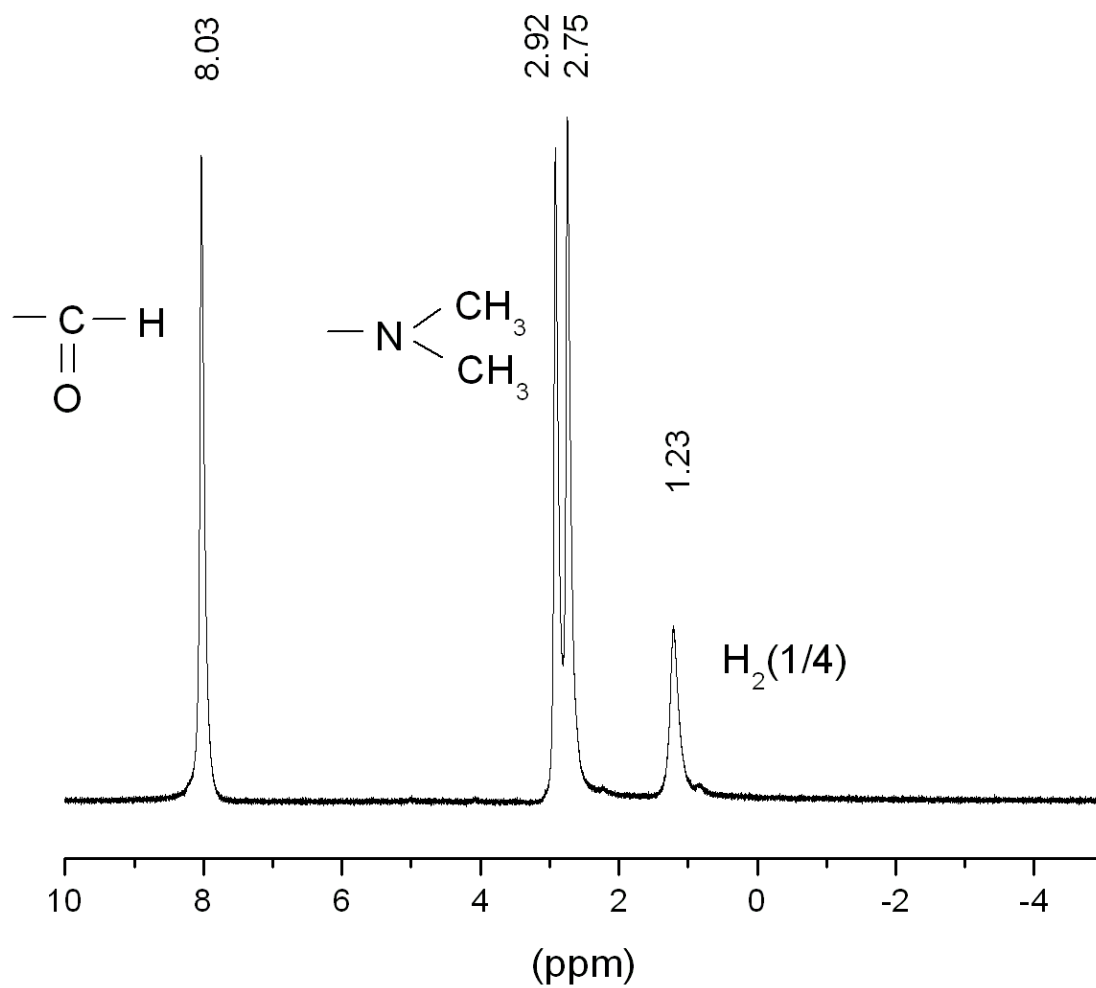
Figure 37. The negative ToF-SIMS spectrum ($m/e = 20 - 30$) of $NaHS$. Sodium hydrino hydride ions NaH_x^- $x = 1, 2, 3$ were observed.
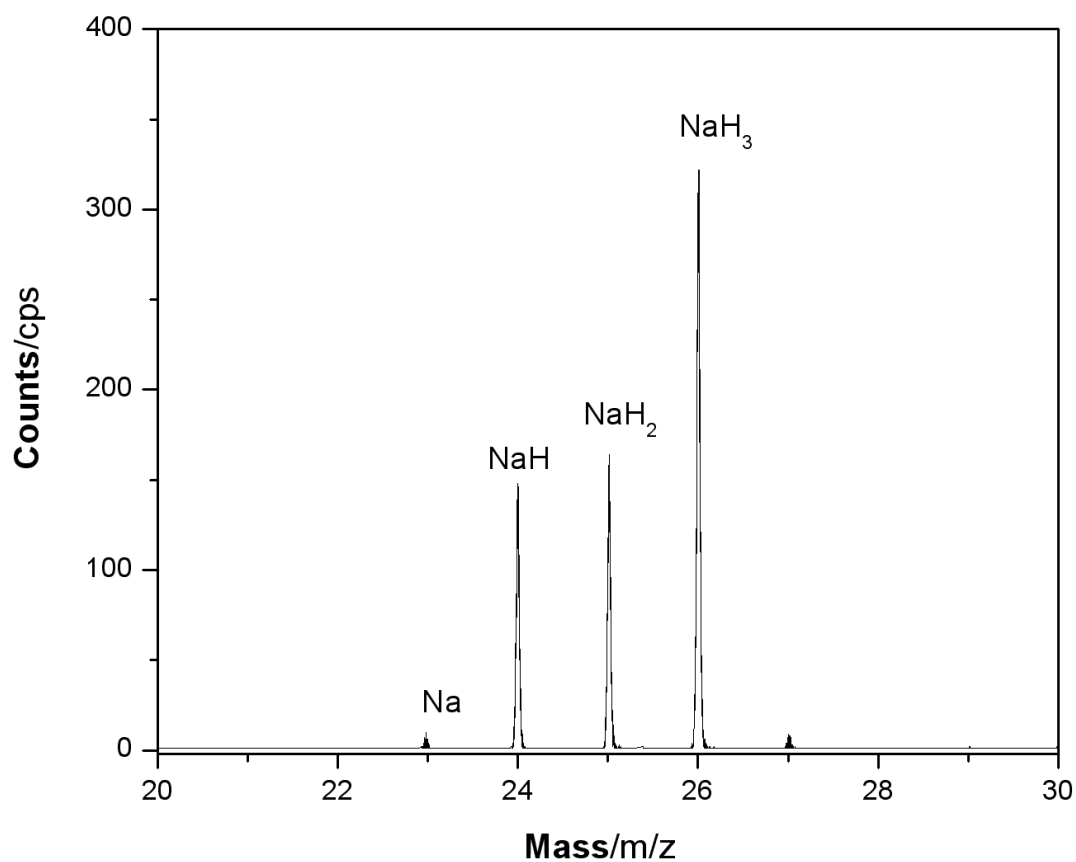
Figure 38. The negative ToF-SIMS spectrum ($m/e = 50-100$) of $NaHS$. Hydrino hydride ion clusters NaH_xS^-, $H_xS_2^-$, and $Na_2H_2S^-$ were observed.
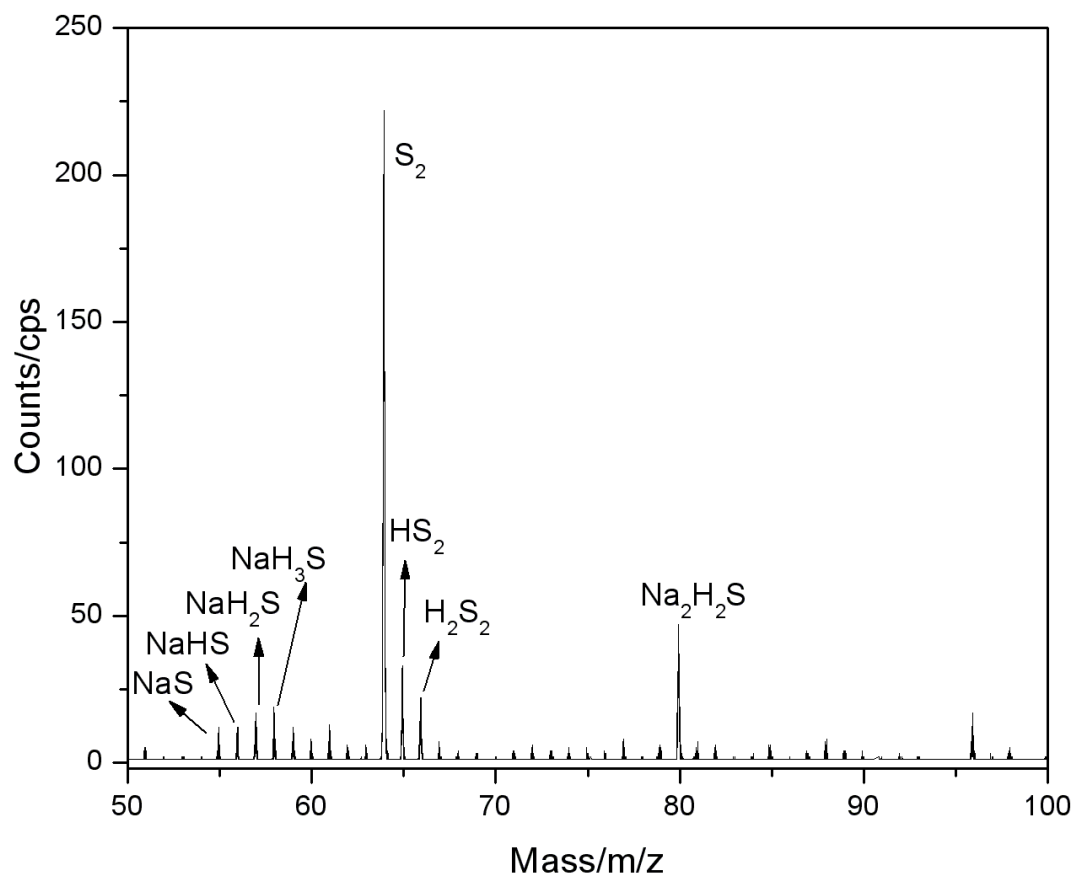
Figure 39. The negative ToF-SIMS spectrum ($m/e = 0 - 20$) of NaH + 5wt% S. Sodium hydrino hydride ions NaH_x^- $x = 1, 2, 3$ were not observed; albeit, S^- was dominant negative ion and Na^+ was the dominant positive ion in the positive spectrum.
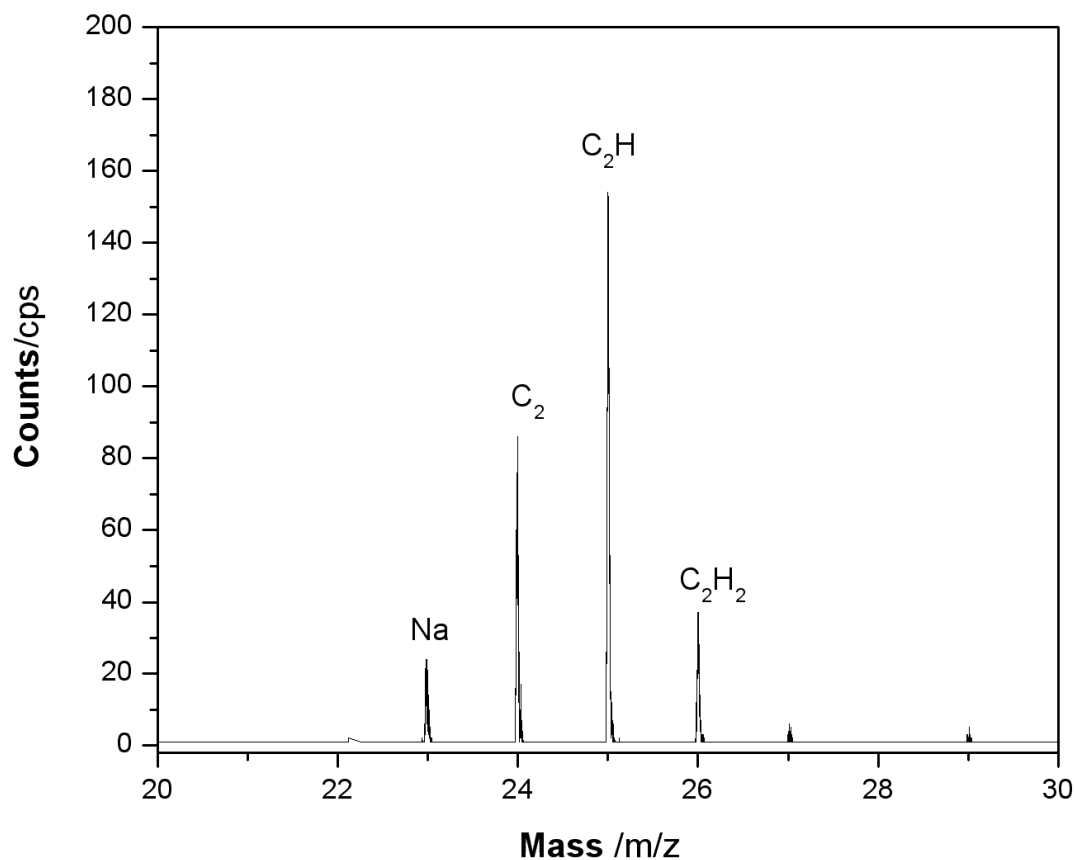
Figure 40. The negative ToF-SIMS spectrum ($m/e = 0-100$) of NaH + 5wt% S showing that S^- was a dominant negative ion.
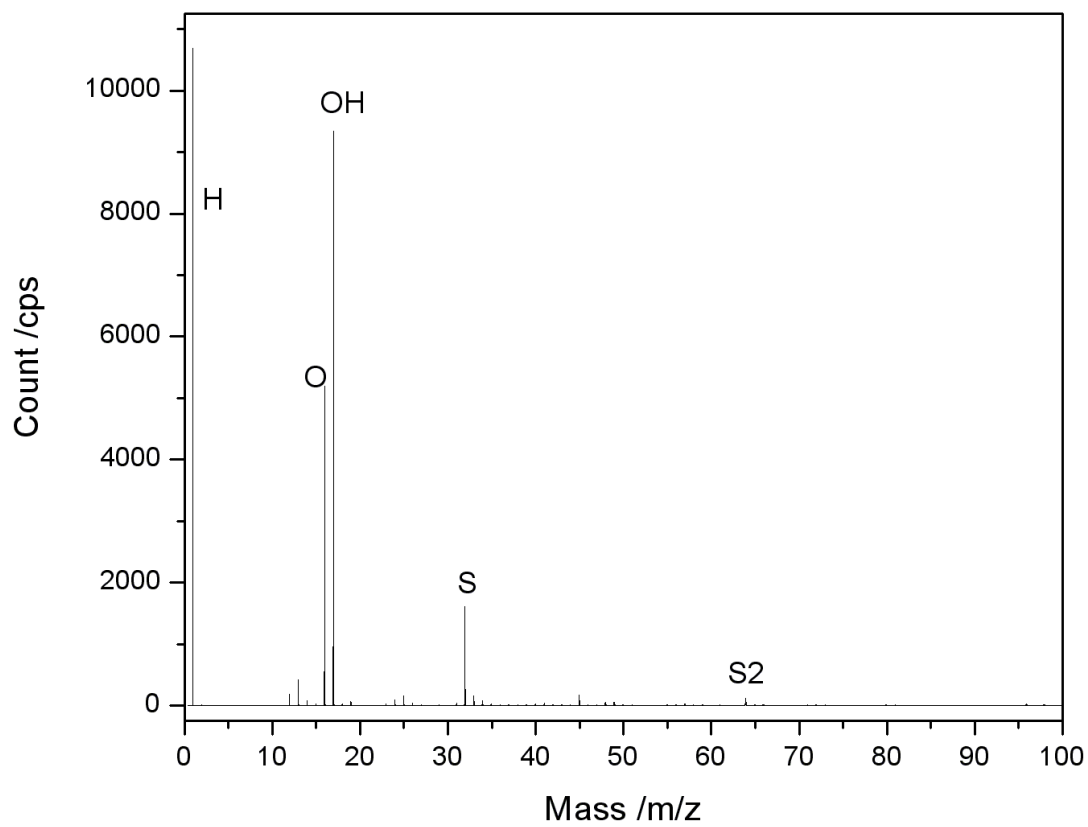
Figure 41. XPS survey spectrum ($E_b = 0$ eV to 1200 eV) of *NaHS*.

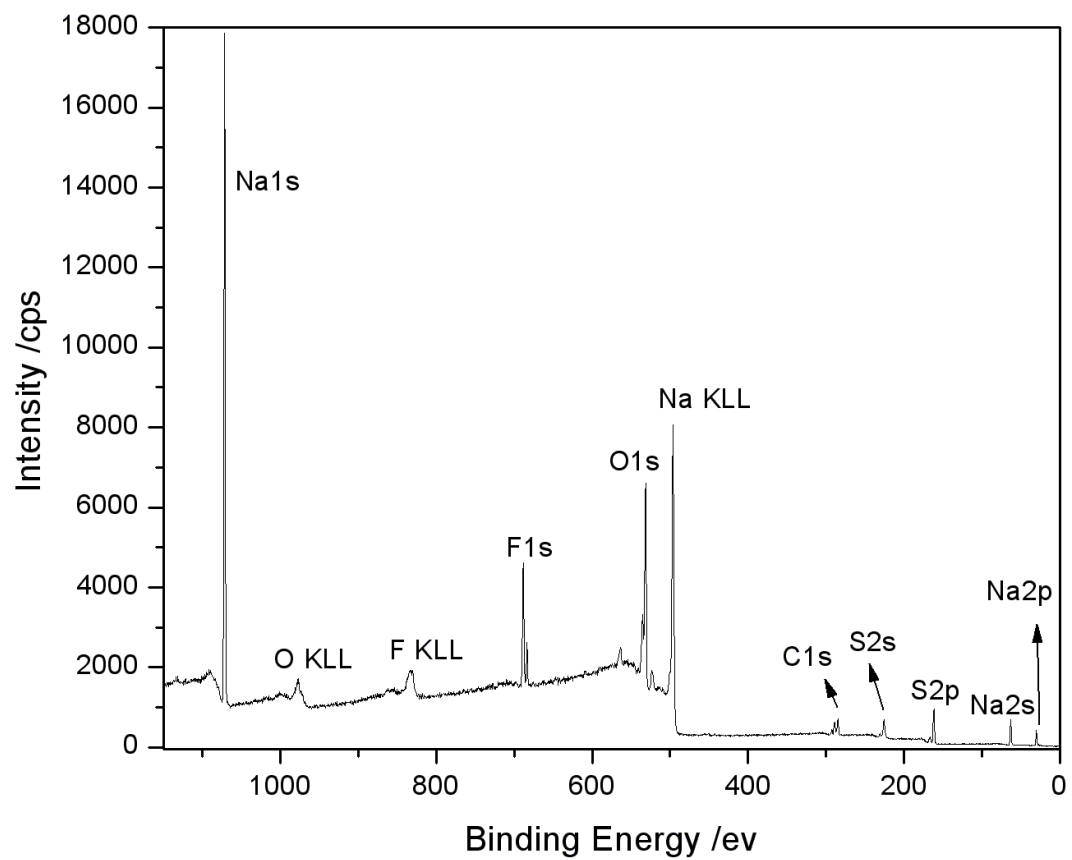Figure 42. High resolution XPS spectrum ($E_b = 0\ eV$ to $50\ eV$) of *NaHS* having peaks at 9.5 eV and 12.7 eV that could not be assigned to known elements and do not correspond to any other primary element peak but do match the $H^-(1/4)\ E_b = 11.2\ eV$ hydride ion in two chemical environments.